CRACKING BEHAVIOUR OF CLAYEY GEOMATERIALS

Ian Murray

Thesis submitted to the Department of Civil and Environmental Engineering, University of Strathclyde, Glasgow, in fulfilment of the requirements for the degree of

Doctor of Philosophy

in

Civil and Environmental Engineering

December 2017,

Glasgow, UK

Declaration of authenticity and author’s right

This thesis is the result of the author’s original research. It has been composed by the author and has not been previously submitted for examination which has led to the award of a degree.

Signed:

Date: 11 December 2017

Abstract

Cracking is a significant problem in the ceramics industry. It results in a substantial loss of production due to the discarded cracked wares associated. There is an understanding that cracking relates from restrained shrinkage and/or uneven drying. One of the solutions to this is to slow the rate of evaporation so that the wares dry more evenly. Such remedial measures are impractical due to the increase in drying space required. What is therefore required for the ceramics industry is a greater understanding of cracking and methods, which work within their manufacturing limitations, to reduce cracking susceptibility.

Despite a number of studies, there is a lack of understanding surrounding the mechanisms of crack initiation. It is clear from experimental evidence that the vast majority of cracking occurs while the soil is still saturated or at the transition from saturated to unsaturated. Many researchers assume that cracking is governed by total stress, i.e. a crack initiates when the tensile stress generated in a soil during drying exceeds the tensile strength of the material. However, this criterion conflicts with the long-standing and widely supported assumption that clay behaviour in the saturated state is governed by the effective stress (and not total stress).

This research investigates the mechanism of crack initiation using an effective stress based approach. A new tensile testing device utilising high capacity tensiometers to allow for the measurement of (negative) pore-water pressure during testing and, hence, the characterisation of the effective stress state has been developed. The device has been designed to test clays in both saturated and unsaturated states.

A series of tensile tests were performed on saturated clay samples prepared using non-de-aired and de-aired water. The results show that for non-de-aired tests, when suction approached

the air-entry value, failure occurred at a deviatoric stress lower than the one corresponding to the critical state line derived from triaxial and uniaxial compression tests. For specimens with the slurry de-aired before slip casting the de-airing process realigned the deviator stress at failure recorded in the tensile test with the critical state line derived from uniaxial and triaxial compression tests. It could therefore be speculated that water cavitation is one of the mechanisms that can control rupture of clay when subjected to a (total) tensile stress state. Finally, failure data from tests on unsaturated specimens could be fairly modelled by the Mohr-Coulomb criterion extended to unsaturated states. These tests confirm that tensile failure is associated with failure in shear for both saturated and unsaturated states.

Further validation of the shear failure mechanism is attempted via a numerical study using a simple coupled hydro-mechanical Finite Element Method (FEM) model to simulate the desiccation of a clayey soil to the point of crack initiation. The results of four laboratory desiccation tests of specimens with non-uniform geometry and different hydraulic boundary conditions are presented. These tests were simulated via FEM, and the time and location of cracking compared to test the validity of the model and the failure criterion.

A greater understanding of the mechanism of cracking has then be used to test more practical remedial measures that can be used in the manufacture of ceramics to reduce cracking. These measures are based around altering the material mixes used in production process, as to this point the adjustment of the slip material relating to cracking has been done by a process of trial and error without guidance. The results of Finite Element Method simulations suggest creating a material with a more graded grain and pore-size distribution can reduce deviatoric stress development during uneven drying.

List of Journal and Conference Papers

"A tensile strength apparatus with the facility to monitor negative pore-water pressure" I. Murray, A. Tarantino & F. Francescon. Submitted for publication to the Geotechnical Testing Journal.

"Mechanisms of crack initiation in clayey geomaterials under saturated and unsaturated conditions" I. Murray & A. Tarantino. Submitted for publication to Gèotechnique.

"Effective stress dependent failure criterion for desiccation cracking in fine-grained soil" P. Gerard, I. Murray & A. Tarantino. Submitted to UNSAT 2018, the 7th International Conference on unsaturated soils.

"The interplay between grain and pore-size distribution and susceptibility to cracking of clays in greenware state" I. Murray, A. Tarantino & F. Francescon. Submitted for publication to the Journal of the American Ceramics Society.

ACKNOWLEDGMENTS

I would like to express my thanks to my supervisor Alessandro Tarantino for his help and ideas throughout this PhD, without this help I would never have finished.

I gratefully acknowledge the funding received towards my PhD from Ideal Standard Italy and the support given by Fernando Francescon.

My thanks also to Pierre Gerard for his work on the modelling of the evaporation tests.

I would like to thank Derek McNee and the other department technicians for their support given for my experimental work.

A special thanks to my examiners Domenico Gallipoli and Gráinne El Mountassir for their time and constructive feedback.

I would like to thank my family and everyone who has supported and helped me during this PhD.

Finally, my thanks to Gea for her priceless support over the last 2 years.

Table of Contents

1 BACKGROUND

1.1 The importance of Cracking in Geotechnical, Hydrological, and Ceramic Engineering

The development of cracks in geomaterials exposed to drying is a worldwide phenomenon and an important issue in many geotechnical engineering, agricultural and environmental applications due to the adverse effects that cracks have on the mechanical and hydraulic properties of a soil. As a result of wetting and drying through seasonal weather patterns soils may crack, and the effects of climate change may increase instances of cracking. As a result, desiccation cracking and its effects have been studied in detail for a number of years in many fields.

Cracked soil has a reduced overall shear strength than its intact state, affecting its stability and bearing capacity (Stapledon, 1970, reported Morris et al.,1992). Desiccation cracks affect the stability of slopes (Baker, 1981) and in the top section of a slope may be a sign of impending slope failure (Peron, 2008).

The presence of cracks has a significant effect on the hydraulic properties of a soil. The hydraulic conductivity has been reported as increasing from 1×10^{-9}m/s to 1×10^{-6}m/s in cracked soil (Albrecht and Benson, 2001). This is significant as cracks can act as pathways for fluid and gas. This may lead to the increase in erosion rate of soils (Mitchell and Soga, 2005). Cracks in dams and embankments provide pathways for water infiltration and result in an increase in pore water pressure (reduction in effective stress) and leaks (Marsland & Cooling, 1958; Marsland, 1968; Dyer, 2005).

Desiccation cracks reduce the effectiveness of soil barriers, where the soil has been chosen

because of its low permeability, such as landfill liners and top covers (Heibrock, 1997), and can result in the contamination of groundwater. In deep nuclear waste isolation bentonite can be used to act as a buffer and can be subjucted to shrinkage and cracking as a result of thermal changes as a result of the waste (Park et al, 2001).

In agriculture, desiccation cracks allow water and nutrients to infiltrate quickly though the soil, bypassing the root systems in the top metres of soil and resulting in water and nutrient shortages for crops (Bronswijk, 1991)

Desiccation cracks are also important in other fields, including the ceramic industry. In the production of sanitaryware products greenware forms (describing a shaped piece after it is removed from the casting mould left to dry at ambient temperatures before final firing. During the drying process cracks can develop in the wares as a result of improper drying conditions (Cooper, 1978). Cracked wares are discarded. The loss of wares attributed to desiccation cracking is quantified at 5-10% of the total production (Tarantino et al., 2010).

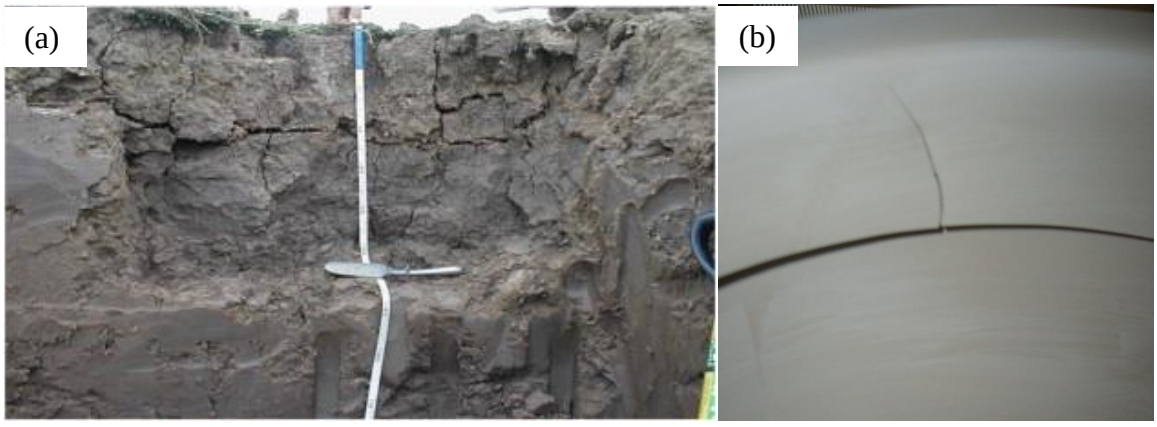

Figure 1-1 (a) Embankment failure due to desiccation cracks (after Dyer, 2009), (b) Cracking in ceramics during air drying

1.2 The Hydro-Mechanics of Desiccation

Drying or desiccation will occur from a soil when there is a thermodynamic imbalance

between the liquid component of a soil and the surrounding air (Coussy et al., 1998). To restore equilibrium a transfer of fluid occurs between the capillary held water and the atmosphere. In turn, this exchange generates a drop in the liquid pressure at the surface and subsequently, a gradient in liquid pressure between the outer and inner regions of the soil (Tarantino, 2010). The gradient of liquid pressure generates a flow, governed by Darcy's law (Darcy, 1856), of pore water from the inner to the outer region of the soil. The drying process will continue until the thermodynamic balance is restored.

During drying the liquid pressure will fall below atmospheric pressure, due to the formation and increase in curvature of menisci in the soils pores as water is removed, and a suction will develop. Suction is comprised of two parts, the matric and osmotic suction. The matric suction can be defined as the difference between the pressure of the surrounding air and the pore water pressure (Fredlund & Rahardjo, 1993). Osmotic suction develops in soil liquids where there are dissolved solutes present (Krahn & Fredlund, 1971). For this study, the soils used have a negligible osmotic suction, therefore the terms suction and (negative) matric suction, negative pore water pressure and pore water tension are effectively referring to the same thing.

A consequence of the removal of liquid during the drying process is soil shrinkage (Peron, 2012). In the saturated state the behaviour is controlled by Terzaghi's effective stress (Terzaghi, 1936):

$$\sigma' = \sigma - u_w = \sigma + s \qquad [1.1]$$

where σ is the total normal stress (the force per unit area, imagining the soil to be a single-phase material), σ' is the effective normal stress, representing the stress transmitted through the soil skeleton, u_w is the (negative) pore-water pressure and s is the suction (negative pore-water

pressure, u_w). Drying shrinkage is related to the soil liquid retention properties and the compressibility of the soil matrix. Shrinkage is a response to the increase in suction (negative pore-water pressure, u_w) (Marinho, 1994), which acts as an attractive force between the elements of the soil matrix. An increase in suction results in an increase in the effective stress, which results in the soil matrix becoming more closely packed. The shrinkage is a result of a decrease in the void ratio of the soil.

This thesis is usually concerned with specimens in a saturated state, but with negative pore water pressures. As such Terzaghi's effective stress concept (Eq. 1-1) is used for calculations of effective stress. When discussing specimens that are in an unsaturated state alternative concepts that address the degree of saturation are presented.

Desiccation cracks develop when there is some form of restriction upon the soils shrinkage that causes the development of stress (Hueckel, 1992). Constrained shrinkage can result from the presence of an external frictional or traction based boundary condition (Corte & Higashi, 1960). Constraints may also arise from within the soil body as a result of soil moisture gradients causing one part of the soil to prevent the shrinkage of another (Colina and Roux, 2000). Finally, it has been speculated that natural properties of the soil, such as the existence of large solid particles, may act as a restraint to shrinkage i.e. small particles surround one large particle and are unable to shrink freely during drying (Towner, 1988). In the case where there is no restriction on free soil shrinkage, there will be no generation of stresses and no cracking will occur (Peron, 2008).

It is commonly acknowledged that most of the shrinkage during desiccation occurs when the soil is still saturated or near the point of desaturation. As the soil dries beyond the point of desaturation the soil shrinkage virtually stops (e.g. Tarantino et al., 2005 and Hu et al., 2007). As the generation of stresses that can cause cracking is dependent upon some form of restrained

shrinkage, if the soil is no longer shrinking there is no further generation of stresses and hence, cracking is unlikely.

1.3 Criteria for crack initiation

The majority of existing yield and failure criterion in soils are related to compression behaviour, which is controlled by shear resistance. Despite the importance of cracking for the mechanical and hydrological behaviour of soils there has been relatively little experimental investigation towards a criterion for crack initiation, the majority of work has been focused towards crack propagation.

1.3.1 Total stress criteria (Tensile Failure)

The commonly held opinion for authors publishing on cracking in soils is that cracking is a tensile failure, based upon a total stress analysis i.e. the soil has a tensile strength and cracking occurs when the stress in any plane is greater than this strength (Trabelsi et al. 2011; Amarasiri et al. 2011; Nahlawi and Kodikara, 2006; Tang et al. 2011; Stirling et al. 2015; Rodriguez et al 2007; Peron et al. 2009). This opinion is based on the propagation of desiccation cracks. In fracture mechanics, Mode I failure (tensile failure) occurs when the crack faces separate in a direction normal to the plane of the crack.

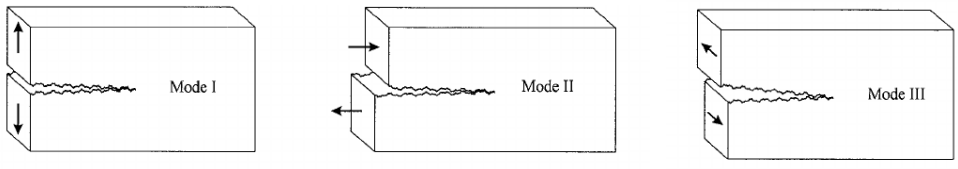

Figure 1-2 Fracture mechanics modes of failure (Yavari et al., 2002)

It is evident from many studies that as a soil dries, the tensile load it is able to withstand prior to failure increases to, and for some soils beyond, the point of desaturation (e.g. Heibrock et al., 2003; Prat et al., 2008; Trabelsi et al., 2010). This is widely acknowledged to be a result of the increase in suction, which causes the inter-particle forces to increase. There is clearly a relationship between suction and the perceived tensile strength. Often, in the absence of suction measurement, the relationship is instead between water content and tensile strength. The tensile strength of a soil is experimentally determined using a tensile testing technique.

The concepts of fracture mechanics are often used, in conjunction with tensile failure, to explain the initiation of cracks. The propagation of cracks is often approached using a Linear Elastic Fracture Mechanics Approach (LEFM), which is based on Griffth's theory of brittle fracture (Griffith 1924). Observing that the fracture strength of brittle materials was often lower than the theoretical strength, Griffith proposed that in materials there existed inherent randomly orientated defects, which would act as locations of stress concentration and therefore early failure would occur when this concentration of stress reaches a critical value.

A fracture mechanics approach has often adapted by people to explain the formation of cracks in soils (Morris et al., 1992; Kodikara & Choi, 2006; Peron et al., 2009; Amarisiri et al., 2013; Miller 2015). Many studies have adapted experimental techniques and devices from LEFM testing to obtain material properties, such as tensile strength, fracture toughness and activation energy, and modelling cracking using LEFM concepts (Lachenbruch, 1961; Morris et al, 1992; Ayad et al., 1997; Amarisiri & Kodikara, 2011). As the assumption of Mode 1 failure is still made in such studies, the tensile strength of the material is a key parameter.

Some studies have shown that the assumption of linear elastic behaviour is not reasonably applicable to clayey soils where there are plastic deformations occurring at the crack tips (Saada et al. 1985, Hallet et al. 1995). LEFM's applicability to successfully describe cracking in dry,

brittle soils exhibiting little plastic behaviour has been shown by Lima & Grismer (1994) and Hallett et al. (1995). The use of models incorporating plasticity around the crack tip, such as J-integral (Rice, 1968), can provide a method of simulating cracking for wet soils (Costa and Kodikara, 2012).

1.3.2 Effective stress criteria (Shear and Tensile Failure)

There is limited investigation into cracking as being initiated by a failure in shear. Parry (1960) performed triaxial extension tests on saturated Weald clay. The tests showed that failure points for both drained and undrained extension tests satisfied the Hvorslev failure concept (1937). Thusyanthan et al. (2007) performed an investigation of the stress and strain criteria for crack initiation in over consolidated Kaolin bars using 4-point bending. Importantly, tensiometers were used to record the pore water pressure throughout testing.

The stress state of the extreme tension fiber at the point of crack initiation showed that cracking occurred when the effective stress state reached either the tension cut off line or an apparent failure line which corresponded to Hvorslev's normalisation of the Mohr-Coulomb failure envelope i.e. When the total stress is negative, it was shown that cracking would occur through shear failure (mixed mode I and mode II).

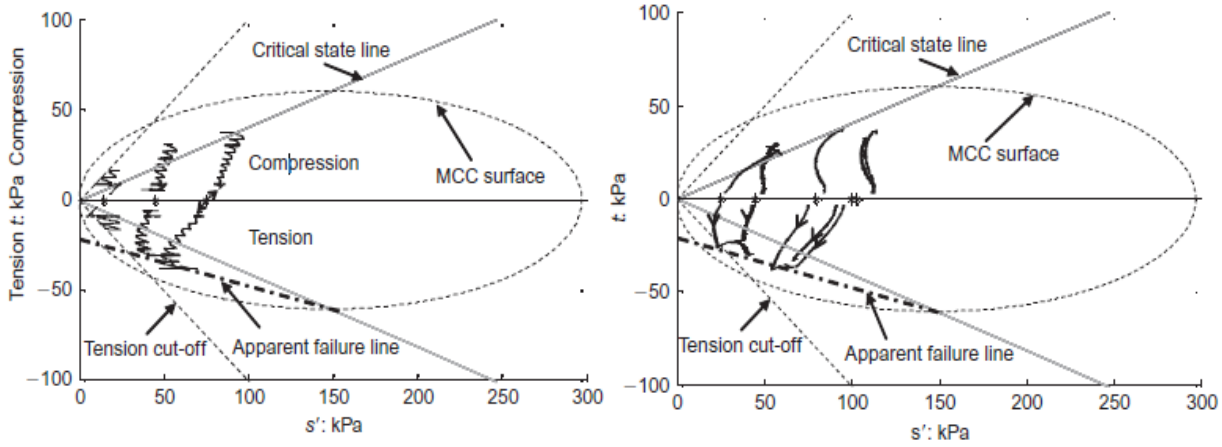

Figure 1-3 Stress paths to failure in (a) stress controlled and (b) strain controlled bending tests (after Thusyanthan et al., 2007)

1.4 Experimental investigation of the response of soil under (total) tensile stress state

There is no universally accepted best method of testing soils in tension as there is for shear or compression tests. Methodologies have often been created by adapting standard tests or from taking tests designed for use on other materials, such as rocks.

Determination of tensile failure conditions has, in the past, generally focused on a total stress based experimental procedure with little focus being put on the control or measurement of suction. To improve the understanding of desiccation cracking, an experimental method which has the ability to measure suction during testing should be considered.

Tensile testing methods for soils can be divided into two categories based upon the method of load application; indirect tension tests and direct tension tests. A brief description of some of the more common tensile testing methods follows with some of their main advantages and disadvantages discussed.

Indirect tests use a test specimen with a specifically designed geometry so that upon

loading, either from a compressive force or bending moment, tensile stresses develop on a plane where the specimen failure will eventually occur.

1.4.1 Brazilian Test (indirect test)

The Brazilian test, also referred to as the diametrical compression test or indirect tension test was developed by Carneiro and Barcellos (1953) and Akazawa (1953)., It has become a well-used method of testing the tensile strength of concrete and rock, but has also been used for testing soils, see Frydman (1964), Krishnayyad and Einstein (1974), Blazejczak et al (1995), Vilar et al (2009), Stirling et al (2015). A cylindrical disk shaped specimen, lying horizontally, is loaded with a compressive force through diametrically opposed rigid platens. Along the plane between the platens the applied compressive force generates a tensile stress which acts perpendicular to the compressive force. The compressive force is increased until the radial stress is greater than the uniaxial tensile strength and the specimen fails along the loaded plane.

A problem associated with the Brazilian test, particularly with soils, is deformation of the specimen at the loading plates. The validity of the test with high deformation was investigated by Frydman, 1964. A maximum deformation was proposed, beyond which the assumptions of the test were no longer valid. Due to the limit upon the deformation, the applicability of the test is limited to soils that are unsaturated and it is difficult to see any way of using the Brazilian test to test the tensile behaviour of specimens across the full range of saturation. Analysis of the tensile stress at failure is based upon the assumption of linear elasticity, an analytical solution for which can be found in Jaeger and Cook (1969).

Horizontal strain measurement is commonly done in concrete testing with the use of a strain gauge extensometer or a Linear Variable Differential Transformer. In the case of soils, a useful measurement of tensile strain is more difficult. The tensile stress reduces rapidly with increased

distance from the centre of the disk, meaning strain measurement would have to be done over a very short length. Additionally, the strain recorded would only be partially due to the tensile stress, with a significant strain component coming as a result of the applied compressive force through the effect of Poisson's ratio (Ajaz and Parry, 1975).

There are no examples of suction measurement in the literature for the Brazilian test. Suction measurement would be very difficult due to the non-homogeneous stress field. A tensiometer would have to be placed onto the centre of the specimen.

In addition, the non linear-elastic behaviour of saturated soils makes the Brazilian test an unsuitable method for accurate testing of soils subjected to a tensile total stress.

1.4.2 Bending Tests (indirect test)

The 3-point bending test, also referred to as the flexure bending test, is used in materials engineering for rock and concrete testing. It consists of the specimen acting as a beam. It is supported at each end and a point load applied at the midspan. Under this load the beam deflects, the largest tensile and compressive forces occurring in the extreme bottom and top fibres respectively. The value of these extreme stresses are calculated as follows from Jaeger and Cook 1969, using the assumption of linear elasticity;

$$\sigma_t = -\frac{PhL}{2I} \qquad [1.2]$$

where P is the applied load, L is the length of the beam from the mid-point to the support, h is half the beam height and I is the moment of inertia for the beam.

The use of equipment to extensively measure the development of strain across the beam offers an alternative and more reliable testing method than the assumption of linear elasticity.

Knowing the strain field, means the stress:strain relationship is considered and allows calculation of the stress based upon equilibrium of forces and moments. The equation for calculating the tensile stress becomes:

$$\sigma_t = \frac{1}{\varepsilon_c + \varepsilon_t}\left[\frac{\partial}{\partial \varepsilon_t}\left(\frac{B}{2L \cdot (2h)^2}(\varepsilon_c + \varepsilon_t)^2\right)\right] \quad [1.3]$$

where B is the applied bending moment and ε_c and ε_t are the measured extreme compressive and tensile strains. Measurement of the strain field has been achieved for this test by Ajaz and Parry, 1975, and Thusyanthan et al, 2007. Ajaz and Parry, 1975, used a radiographic technique, with lead being implanted into the specimen to monitor the displacement. Thusyanthan et al. (2007) replaced the radiographic technique by using Particle Image Velocimetry, as detailed by Take (2003). Thusyanthan et al. also used two loading points to create a 4 point bending test. The addition of the second loading arm creates a homogenous tensile stress zone in the extreme tensile fibre between the loading points. In addition, tensiometers were embedded into the specimens to record the pore water pressure during loading, allowing for an effective stress analysis of the test.

Non-direct tensile testing methods do not allow the operator control of the stress path and rely either upon the assumption of linear elastic behaviour, which is not accurate for soils, or overcome this assumption with the use of extensive measurement of the local strain which increases the complexity of the test.

1.4.3 Uniaxial test (Direct Test)

Direct tension tests are generally performed by applying a uniaxial stress to one of the

boundaries of the test specimen, while the other boundaries remain free to deform. Direct tests are generally simpler than indirect tests because, as the force is applied directly, the relationship between stress and strength can be obtained without the need for complex analysis. In general, the force can be applied to the soil in two ways: either by bonding the loading system directly to the specimen, or by using moulds designed to hold the specimen (friction based) from which the load can be applied. An important aspect when applying the tensile load is to not create any unwanted shear stresses within the specimen.

The majority of friction based tests follow a similar design of both specimen and apparatus. The specimen has a larger cross-sectional area at its ends than in the centre. A specimen is prepared in two moulds which act to hold the specimen upon loading. The moulds have converging sides which effectively hold the specimen by friction. One of the moulds is fixed in position while the other remains free to move and is the part to which the loading is applied. Loading can either be stress or strain controlled. Recent examples of this general method of tensile testing for soils include Kim and Hwang, 2003; Rodriguez et al., 2007; Trabelsi et al., 2012). Minor modifications to this idea have been made by Snyder and Millar (1985) who used a figure of eight shaped mould and Nahlawi et al, (2004) who used shear keys instead of converging sides to grip the sample during testing (Figure 1-4b). An accurate analysis of the impact of the shear keys on the soil specimen, given their embedded nature, is impossible and it is conservative to assume some influence on the stress in the region of the failure.

Examples of direct bonding are far less common, this is due to difficulties in finding a suitable method of bonding the specimen, which is often soft and wet, to the traction system. Farrell et al. (1967) used Araldite, an epoxy based adhesive resin to secure brass end-plates to a cylindrical soil specimen, which was then loaded to failure. In order to achieve a successful adhesion, it was necessary for the ends of the soil specimen to be dried beforehand. Epoxy resin

was also used by Heibrock et al, (2003) as the bonding agent. Compacted kaolin cylinders were drilled through to allow for the gluing of hooks at either end of the hollow cylinder. These hooks were then used to pull the specimen apart. The results show that the specimens tested were all unsaturated, as the specimens had to be able to be self-supporting. Tang and Graham (2000) presented a method for testing unsaturated soils in tension using 2 half cylindrical moulds. The specimen was fixed securely to the moulds using an epoxy paste adhesive. However, Nahlawi et al. (2004), reported problems with this adhesive not working correctly.

Gripping the soil laterally with friction based designs is likely to create shear stresses from the contact between the specimen and the mould. To assess tensile failure effectively it is necessary to avoid the introduction of shear stresses close to the location of specimen failure. Despite the difficulties associated with direct bonding of the specimen to the loading system reported in the literature it is the ideal loading method where an accurate determination of tensile strength is required.

The examples of tensile tests mentioned are all examples of globally undrained tests. The load is applied with water not being allowed to enter or leave the specimen. During testing pore-water pressure will change as a result of the applied tensile load. The measurement of pore water pressure during testing is ignored by most tensile testing techniques, but is a critical aspect of investigating tensile strength. The author has found no examples in the literature where a direct method of loading had been coupled with measurement of pore-water pressure.

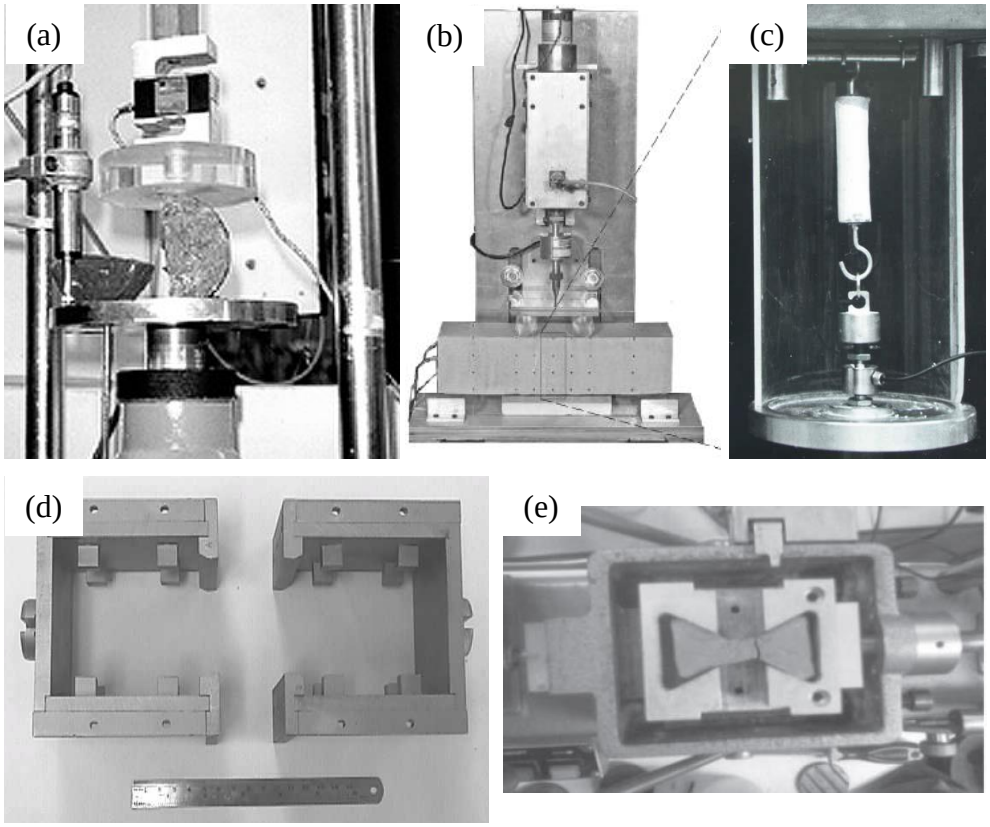

Figure 1-4 Indirect and Direct tensile testing equipment: (a) Brazilian test (after Souza Villar et al., 2009), (b) Beam bending test (after Thusyanthan et al., 2007), (c) Direct pull on hollow cylinder (after Heibrock et al. 2003), (d) Shear key gripping method (after Nahlawi et al., 2004), (e) Strain controlled direct test on bow tie shape (Trabelsi et al., 2010).

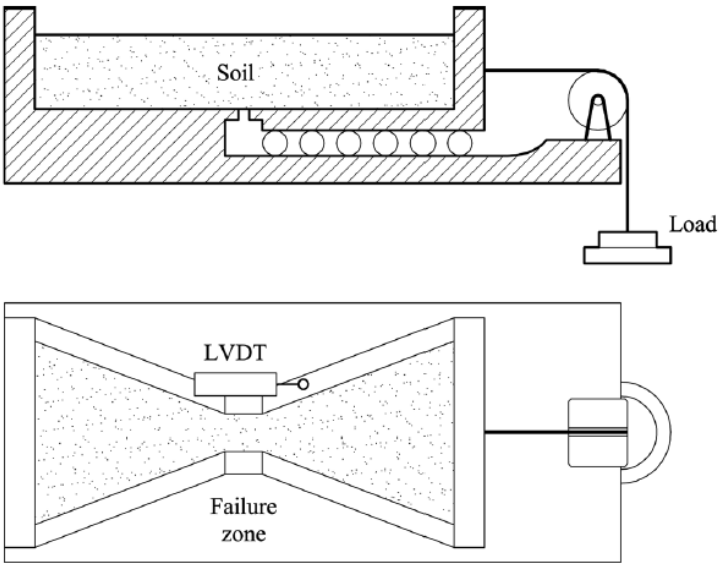

Figure 1-5 Stress controlled direct test on bowtie shaped specimen (after Rodriguez et al., 2007)

1.5 Objectives

The aim of this thesis is to enhance the understanding of the cracking behaviour of clayey geomaterials. This will be achieved by applying experimental, numerical and theoretical approaches.

The main goals of this are:

1. Develop a new tensile experimental test for clays with the ability to measure negative pore-water pressure.
2. Identify the crack initiation mechanism for both saturated and unsaturated states.
3. Develop a numerical model that encapsulates the crack initiation mechanism to simulate the drying of clay forms and predict the time and location of cracking.
4. Provide practical guidance for the ceramic industry on how to prevent/reduce instances of cracking in their production.

Chapter 2 presents a new direct tensile testing apparatus that has been designed to incorporate high-capacity tensiometers, allowing analysis of tensile failure in terms of effective stress. A detailed description of the design and procedure for the experiment are given, as well as some results of tensile tests using the apparatus to validate the methods. Finally, the results of a cam-clay simulation are shown to validate the water flow within the specimen during tensile loading.

Chapter 3 is concerned with the mechanisms of cracking. Full results of tensile tests performed using the apparatus shown in chapter 2 are presented. Two materials are used to demonstrate that failure in tension is a shear failure in both saturated and unsaturated states. Results are then shown for the same materials tested again in tension as well as for standard plastic limit tests, where the slip was de-aired prior to casting, to investigate the role of cavitation in cracking.

With the mechanism of cracking now shown, **chapter 4** is concerned with applying this to the drying process to further validate the shear mechanism. A finite element method coupled hydro-mechanical model is presented and then used to simulate the drying, to the point of crack initiation, of four restrained laboratory evaporation tests. The time and location of cracking for the tests are then compared to assess the accuracy of the simulations.

Chapter 5 is concerned with trying to find a practical solution for use in the ceramics industry to reduce cracking in their production. It is well known that uneven and fast drying result in a higher number of cracked wares. With this in mind two materials with different cracking susceptibility are compared. The Bigot curves, along with the grain and pore-size distributions that control the Bigot curves, are examined. It is speculated that the transition from saturated to unsaturated is key in the formation of cracks and that by making changes to

the material mix used in slip casting that instances of cracking could be reduced. A coupled hydro-mechanical finite element method model is then used to test qualitatively the effect of modifying the material characteristics on the amount of deviator stress generated during drying of a simple disk.

Appendix A shows results from drying tests on two materials (Vitreous China and Fine Fire Clay) which provides evidence of their different susceptibility to cracking. This difference in cracking susceptibility is the basis for chapter 5.

Appendix B shows results from a modified version of the test shown in Appendix A. The results provide further evidence to the role that cavitation plays in cracking, as is first discussed in chapter 3.

.

2 A TENSILE STRENGTH APPARATUS WITH THE FACILITY TO MONITOR NEGATIVE PORE-WATER PRESSURE

2.1 Abstract

This paper presents a new testing method for investigating the behaviour of clayey geomaterials subjected to a tensile (negative) total stress. The method includes the use of high capacity tensiometers to measure the pore-water pressure of the test specimen, an aspect which has not been demonstrated in any other direct tensile testing method. This addition allows interpretation of failure data in terms of effective stress rather than total stress, which is the approach that should be pursued in the saturated range. The test specimen shape and loading method have been modified from those commonly seen in existing literature to ensure that the direction of the major principal stress in the failure zone coincides with the direction of the externally applied tensile force, allowing for a more accurate analysis of tensile failure. Results are shown for saturated specimens and compared to results obtained for the same soil in uniaxial compression, using a modified version of the presented uniaxial tensile method, and a triaxial compression test. It is demonstrated that crack initiation occurs by shear failure if the data is interpreted in terms of effective stress rather than total stress, and that the failure mechanisms under tension do not differ from compression.

.

2.2 Introduction

When subjected to desiccation a soil will shrink. If this shrinkage is prevented tensile stresses will develop in the soil mass and cracking will occur. Fundamental to the understanding of desiccation cracking is an accurate understanding of the conditions which result in crack initiation. Determination of these conditions has, in the past, generally focused on a total stress based experimental procedure with little focus being put on the control or measurement of suction.

Tensile testing methods for soils can be divided into two categories, based upon the method of load application; indirect tension tests and direct tension tests.

Indirect tests use a test specimen with a specifically designed geometry so that upon loading, either from a compressive force or bending moment, tensile stresses develop on a plane where specimen failure will eventually occur.

The Brazilian test, also referred to as the diametrical compression test or indirect tension test, has most commonly been used for testing concrete and rock, but has also been used for testing soils, see Frydman 1964; Krishnayya and Eisenstein 1974; Blazejczak, Horn and Pytka 1995; Vilar et al. 2009; Stirling et al. 2015. In this test, a cylindrical disk-shaped specimen, lying horizontally, is loaded with a compressive force through diametrically opposed rigid platens. There are no examples of suction measurement in the literature for the Brazilian test. Effective suction measurement would be very difficult due to the non-homogeneous stress field that develops during testing.

The flexure bending test is used in materials engineering for rock and concrete testing. It consists of the specimen acting as a beam supported at each end and a point load applied at the midspan. Under this load the beam deflects, the largest tensile and compressive forces occurring

in the extreme bottom and top fibres respectively. The value of these extreme stresses is generally calculated assuming linear elastic behaviour of the clay. The use of equipment to measure the development of strain across the beam offers an alternative and more reliable method than the assumption of linear elasticity. Measurement of the strain field has been achieved for this test by Ajaz and Parry (1975) and Thusyanthan et al. (2007).

Direct tension tests are generally performed by applying a uniaxial stress to one of the boundaries of the test specimen, while the opposite boundary is constrained, with the remaining boundaries free to deform. Direct tests are generally simpler than indirect tests because, as the tensile force is applied directly, the relationship between stress and strength can be obtained without the need for complex analysis. In general, the force can be applied to the soil in two ways: either by using moulds designed to hold the specimen (friction based) from which the load can be applied, or by bonding the loading system directly to the specimen.

The majority of friction based tests follow a similar design of both specimen and apparatus. The specimen has a larger cross-sectional area at its ends than in the centre. A specimen is prepared in two moulds which act to hold the specimen upon loading. The moulds have converging sides which effectively hold the specimen by friction. One of the moulds is fixed in position while the other remains free to move and is the part to which the loading is applied. Loading can either be stress or strain controlled. Recent examples of this general method of tensile testing for soils include Kim and Hwang (2003), Rodriguez et al. (2007) and Trabelsi et al. (2012). Minor modifications to this idea have been made by Snyder and Millar (1985) who used a figure of eight shaped mould and Nahlawi et al. (2004), who used shear keys instead of converging sides to grip the sample during testing. Criticism of friction based tests is associated with the gripping of the soil laterally, which is likely to create shear stresses from the contact between the specimen and the mould. To assess tensile failure effectively, the introduction of

shear stresses close to the location of specimen failure should be avoided.

Examples of direct bonding are far less common, this is due to difficulties in finding a suitable method of bonding the specimen, which is often soft and wet, to the traction system. Farrell (1967) used Araldite, an epoxy based adhesive resin to secure brass end-plates to a cylindrical soil specimen, which was then loaded to failure. In order to achieve a successful adhesion, it was necessary for the ends of the soil specimen to be dried beforehand. Epoxy resin was also used by Heibrock et al. (2003) as the bonding agent. The results show that the specimens tested were all unsaturated. Tang and Graham (2000) presented a method for testing unsaturated soils in tension using 2 half cylindrical moulds. The specimen was fixed securely to the moulds using an epoxy paste adhesive, however, Nahlawi et al. (2004) reported problems with this adhesive.

Despite the difficulties associated with direct bonding of the specimen to the loading system reported in the literature, in particular for saturated specimens, this type of test appears to be the ideal loading method where an accurate determination of tensile stress at failure is required.

This paper presents a method that represents a step change in direct tensile testing. Direct bonding has been chosen, with a new bonding system to allow testing samples in both saturated and unsaturated states. The system implements HCTs to monitor suction allowing interpretation in terms of effective stress. With the exception of Thusyanthan et al. (2007), there are no tests with measurement of suction using HCTs.

2.3 Testing apparatuses

2.3.1 Uniaxial tensile test apparatus

The tensile test is designed as a direct test giving control over the applied axial total stress.

The test is similar in concept to that developed at the Soil Mechanics laboratory at Polytechnic University of Catalonia (UPC) (Rodriguez, 2002) but has some significant modifications.

High capacity tensiometers are used to measure the matric suction of the specimen throughout testing, allowing for an effective stress based analysis of the failure. Three tensiometers were used for each test. The tensiometers were placed onto the surface of the specimen, not embedded within it. One tensiometer was secured to each end of the sample and a third located in the centre section. The suction measured by the centre tensiometer was used in the calculations as specimen failure always occurred in the centre section. The tensiometers at the end were used to validate the suction measured by the centre tensiometer.

The specimen is fixed using the adhesive at one end to a rigid restraint and at the opposite end to a rigid plate from which a hanger is attached via a low friction wheel. The ratio between the (horizontal) tensile force and the hanger dead weight was measured and found to be equal to 0.997. The specimen is placed on top of a layer of ball bearings to reduce frictional effects and allow the specimen to deform freely during loading (Figure 2-1).

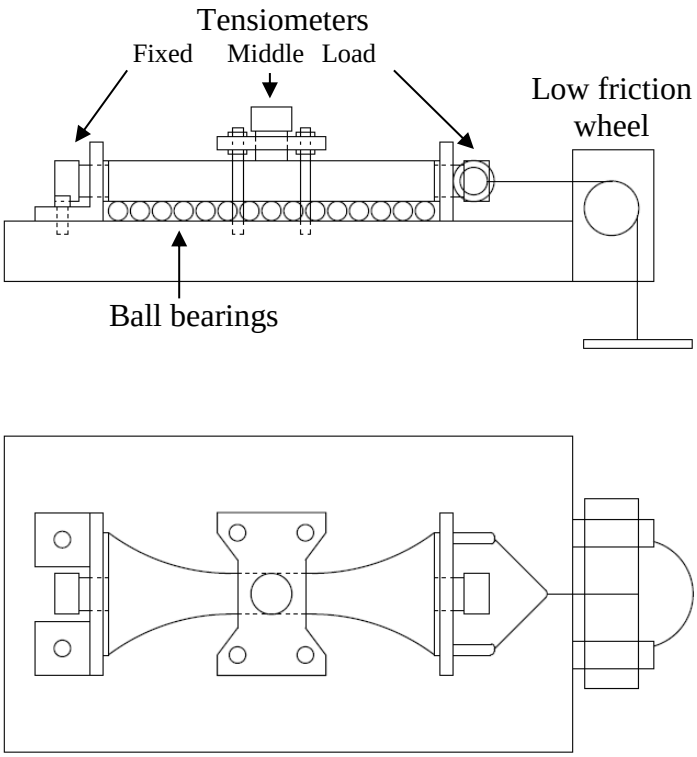

Figure 2-1. Uniaxial tensile test apparatus

2.3.2 Uniaxial compression test apparatus

The uniaxial tensile apparatus was used as a method for testing specimens in compression. To do this a number of modifications to the tensile test apparatus were made. The applied loads required to reach failure in the sample were significantly greater than those for the tensile test. To accommodate the increase in load the tensile test apparatus was mounted for convenience inside the tensile test apparatus of Rodriguez (2002), as shown in Figure 2-2. The low friction wheel, over which the load is applied was moved to be at the same end as the fixed mould. A loading system which bypasses the fixed mould and goes to the loading wheel was attached to

the moveable mould. The metal plates used in the tensile test to restrain and load the specimen were fixed into position on the moveable and fixed mould. The test only used the two tensiometers, located at the ends of each sample. A tensiometer in the centre section was tried, but it was not possible to maintain a good connection between the tensiometer and the specimen.

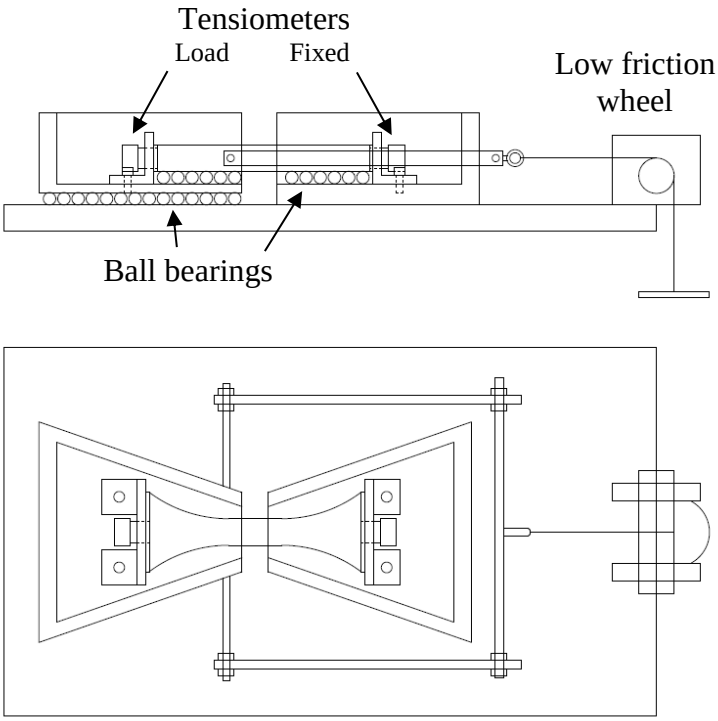

Figure 2-2 Uniaxial compression apparatus

2.4 Design of Specimen shape

Comsol Multiphysics, a finite element code, was used to assess and then optimise the shape of the test specimen. The soil was modelled as a linear elastic material (Young modulus E= $205x10^9$Pa, Poisson's ratio ν=0.3) and the analysis was performed assuming plane-strain conditions. The basic shape of samples used in friction based direct tests reported in the literature was considered as a starting point for the analysis. The centre section, with reduced

area had to be sufficiently large as to allow the fixing of a tensiometer to the specimen, but was limited to 1.5cm due to the method of sample preparation. The centre section should also be of sufficient length to create an area where the stress state is homogeneous, but not so long as to make the specimens too flexible at higher water contents.

Figure 2-3 shows the deviator to isotropic stress ratio, q/p, for a sample with straight sides, which is a similar geometry to Rodriguez (2002), where a deformation equivalent to an average axial strain of 1% was applied at its end. It can be observed that the highest q/p values occur at the transition between the centre section and the diagonals, which would trigger failure at the transition corners rather than the sample centre.

The geometry was therefore modified by trial and error to eliminate the concentration of deviator stresses at the transition corners. The dimensions of the shape finally adopted is shown in Figure 2-5. The values of q/p generated by the same deformation in the sample with curved transition are shown in Figure 2-4. The highest q/p values now occur in the centre section where the stress state appears to be reasonably homogeneous.

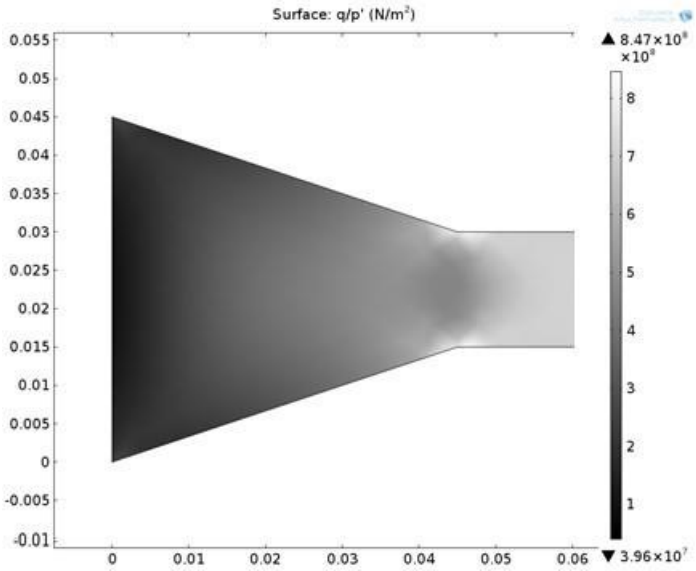

Figure 2-3 Stress state for uniaxial tensile specimen with straight sides

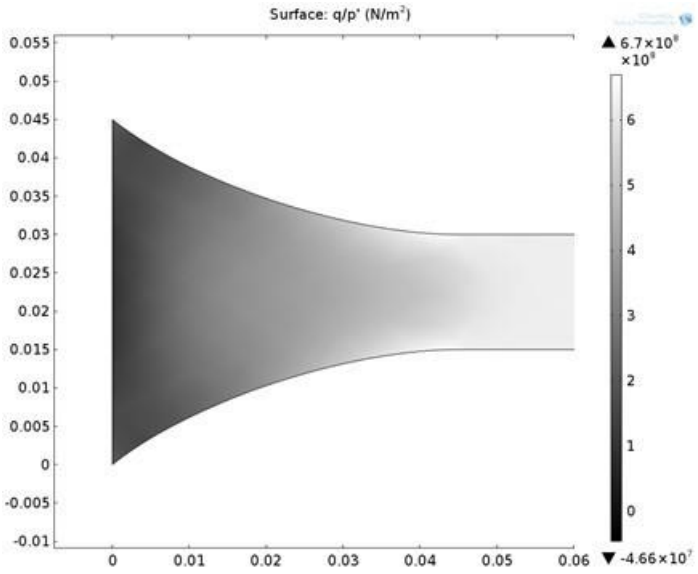

Figure 2-4 Stress state for uniaxial tension test specimen with curved sides

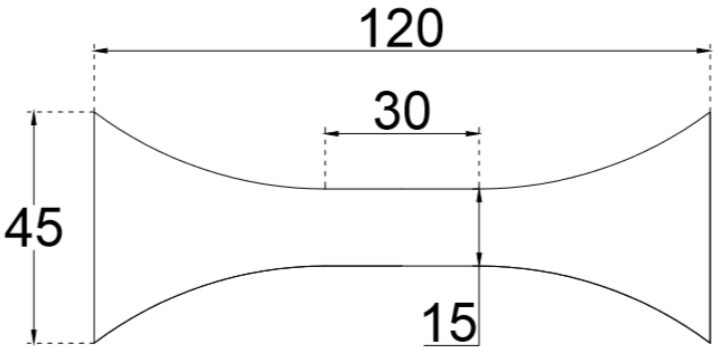

Figure 2-5 Dimensions of final specimen shape (mm)

2.5 Material and specimen preparation

The material used in the tests for the results shown was a Vitreous China mix (comprised of ball clay, Kaolin, quartz and feldspar, the exact composition cannot be disclosed for commercial reasons), a material commonly used in the ceramic industry. Figure 2-6 shows the particle size distribution of the material.

Specimens were prepared by slip casting in plaster moulds. The plaster has a high suction which removes water from the liquid slip to form a plastic specimen. Plaster moulds were used because they were able to produce specimens of complex shape in a relatively short time.

The VC slip, produced by Ideal Standard, Italy, was obtained by mixing the different 'ingredients', each component being added to influence the behaviour of the overall mix, making it suitable for use in the ceramics industry for the production of sanitary ware products. To ensure consistent specimens a large quantity of the VC slip was prepared prior to beginning the experimental programme by mixing the dry powdered constitutive parts with demineralised water to a moisture content of approximately 0.30. The mixed slip was then stored in an air tight container for the period of the experiments. Individual specimens were prepared by taking a portion of the re-mixed slip adding de-mineralised water to reach the required slip density for casting (1.84kg/l, w≈0.35).

Slip was added to the plaster mould. The time required to dry the VC slip was 90 min. Upon removal from the mould the moisture content of the specimens was in the range 0.2-0.21, corresponding to a negative pore water pressure of approximately 100kPa.

Specimens were air dried, where necessary, to target moisture content for the required test, vacuum sealed and stored for 24 hours prior to testing to obtain an equilibrium in the moisture content throughout the specimen. For uniaxial tensile tests samples were air dried to give specimens with initial negative pore water pressure covering the entire saturated range of the material (air entry corresponds to a negative pore-water pressure of approximately 500kPa.

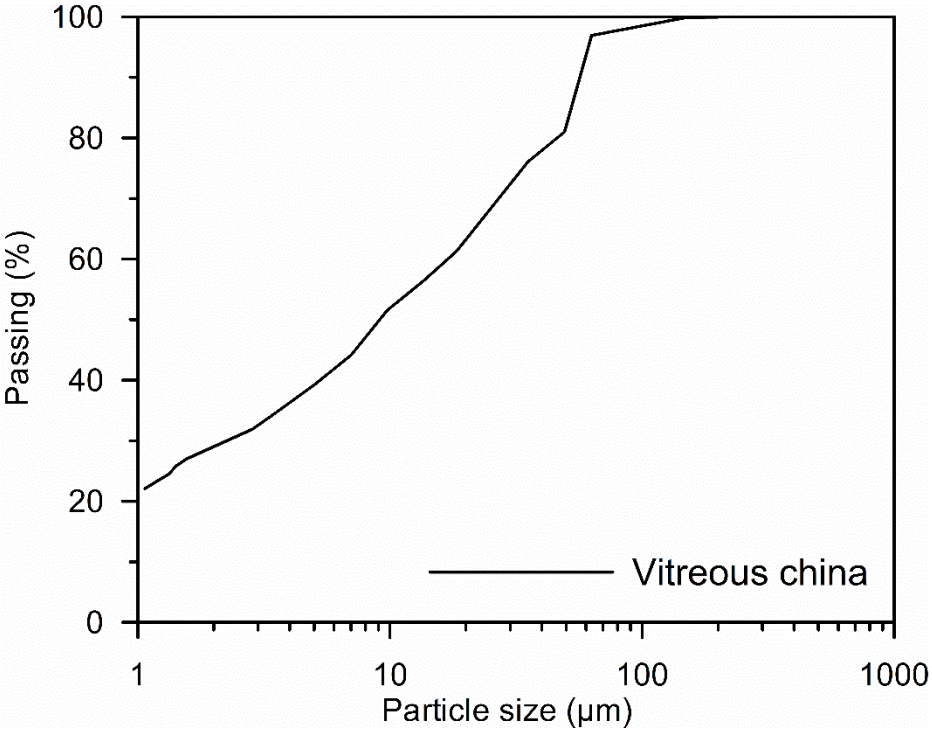

Figure 2-6 Particle size distribution for Vitreous China

2.6 Specimen installation

In an ideal test evaporation from the specimen would be completely prevented. In reality, this was not possible due to the complex specimen shape and the need to attach the tensiometers. Initially petroleum jelly was coated onto the specimens to reduce the evaporation. While this did reduce evaporation and was easy to apply, the water contents of the specimens at failure appeared to not be consistent (water contents at failure lay above the normal consolidation line in the isotropic stress-water content plane). The reason for this is not understood as all the petroleum jelly was removed from the surface of the specimen before weighing and placing in the oven. To overcome this difficulty Parafilm© was used in place of petroleum jelly. Due to the relatively complex shape of the sample it was not possible to create a completely effective barrier using the parafilm to prevent evaporation. The Parafilm© could reduce the base rate of

evaporation sufficiently for the change in suction to be less than 1kPa per minute. A single piece of Parafilm© could not be stretched over the sample as this could provide a load path for the applied tensile load and increase the load at which the sample fails. To overcome this problem multiple pieces of unstretched Parafilm© were used and then silicone grease was used to seal the pieces of parafilm to each other. The grease did not come into contact with the sample.

The specimen was placed onto the ball bearings and glued to the end restraints. The adhesive used throughout the testing to bond the specimen to the loading system was Hilti Hit RE500, a bi component epoxy mortar designed for rebar connections and heavy anchoring. The adhesive was able to restrain all of the different soils tested, with suctions ranging from 100kPa to a near dry sample. The maximum axial tensile stress applied through the adhesive was approximately 130kN/m^2.

Care had to be taken to align the specimen correctly to the restraints and to remove all the glue from the tensiometer holes in the restraints before it cured. During the curing process, dummy tensiometers were inserted in the holes in the restraints to minimise evaporation. The specimen and apparatus were then covered with an additional cling film layer to reduce evaporation from the holes for the tensiometers. The specimen was then left overnight to allow the adhesive to cure.

During early testing, the majority of tests failed under loading at one of the soil-adhesive boundaries. This was attributed to an inability of the parafilm and film to adequately prevent evaporation from the specimen. After a short time (approximately 6 hours) the adhesive cured sufficiently to prevent the specimen shrinkage associated with the evaporation. This resulted in an increase in deviatoric stress along the glue boundaries. Although this was not sufficiently large to cause cracking before loading, the stress caused by the restrained evaporation, in

addition to the applied stress during testing was enough to cause failure at the soil-adhesive boundary, rather than in the centre of the specimen. To overcome this issue the specimen and attached apparatus, while the adhesive was curing, were covered with a plastic box. The relative humidity of the air inside the box was raised by placing beakers of hot water inside. With the introduction of this technique there were no more instances of sample failure at the specimen-adhesive boundary.

After curing of the adhesive, the 3 tensiometers were placed onto the specimen and secured in place. A small amount of soil paste was used to ensure a good contact between the tensiometer and the specimen. The test was again covered with the box while the tensiometers came into equilibrium with the specimen. Prior to loading, the box and film were removed from the specimen for a period of one hour to obtain a base evaporation rate.

2.7 Experimental procedure

2.7.1 Uniaxial tension test

Specimens were tested at the loading rate of 1.96 N/min (≈7 kPa/min) until rupture occurred. To verify that the response time of the tensiometers is adequate compared to the loading rate, an additional tensile test at a higher nominal loading rate of 23.5 N/min (approximately 84 kPa/min) was performed.

The result of this test is compared to a 1.96 N/min standard test with a similar initial pore-water pressure as shown in Figure 2-7. The base evaporation rate for both load rates was accounted for using the change in suction measured by the centre tensiometer for the one-hour period before the start of loading. The change in pore water pressure associated with the loading was similar for both load rates. The effective stress state at failure for the specimens with faster load rate was also on the same failure envelope as the tests from the 1.96 N/min load rate,

indicating that the load rate used had no effect on the test. The 1.96 N/min rate was then used for the tests as it allowed the operator easier control during loading and the base evaporation rate was not considered to be negatively affecting the test results.

The determination of the axial stress at failure required the measurement of the cross-sectional area at the onset of rupture. Due to the centre tensiometer, it was not possible to measure the cross-sectional area of the centre section where the failures were occurring during the tests. The only measurement of size of the centre section possible was to measure the dimensions immediately after the sample had failed. The measurements were taken from a section of the centre section that was not in immediate proximity to the failure.

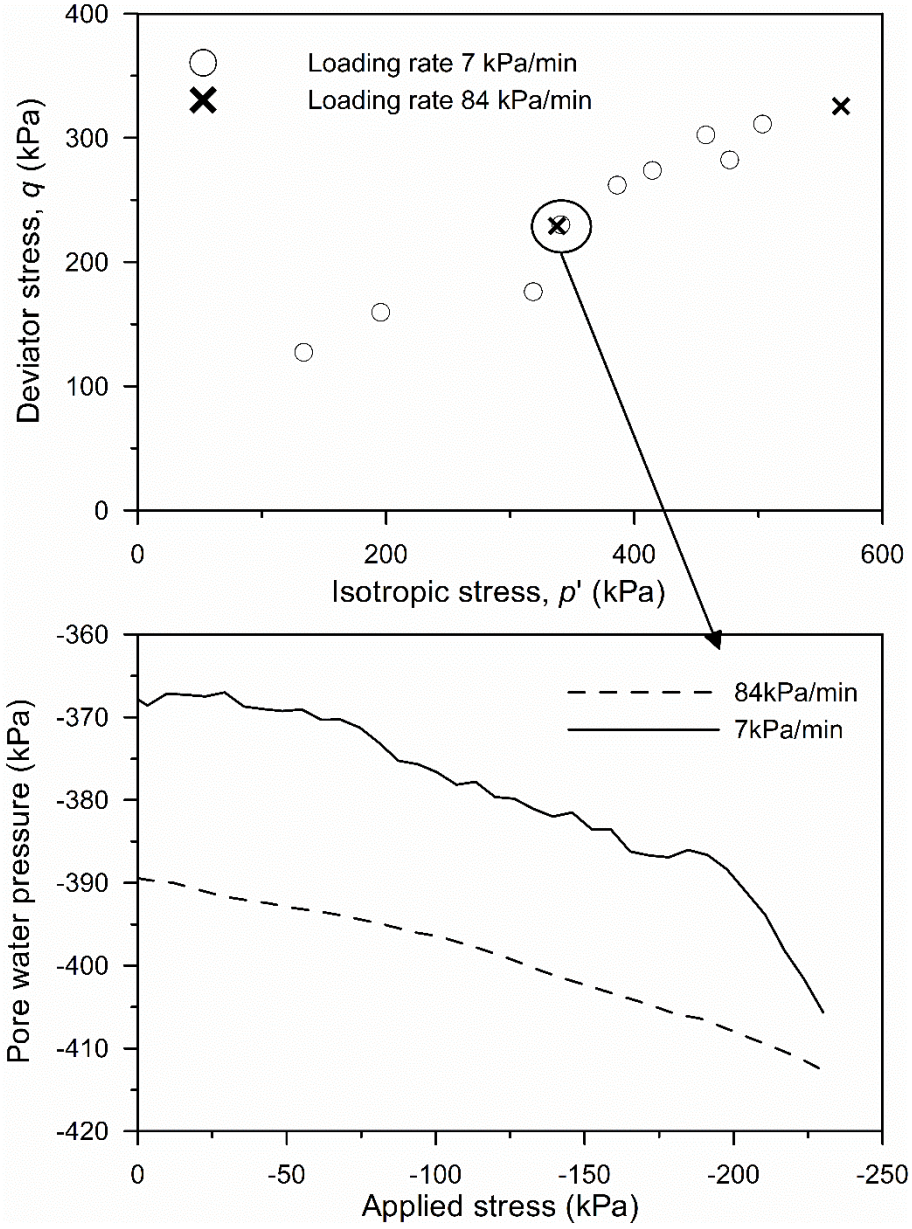

Figure 2-7 Comparison of uniaxial tension test load rate

To relate the post failure cross-sectional area in the centre section to the area immediately before failure, which is necessary for the accurate calculation of the stress state at failure, tests were performed with the centre tensiometer removed and manual measurements of the width and height of the specimen taken during loading. The area after failure was also taken allowing for the calculation of the percentage change in cross-sectional area after failure and immediately before failure. This test was performed at three different specimen moisture contents to create

a best fit line relating the percentage area change to the final moisture content of the specimen. This best fit was used to calculate a cross-sectional area at the time of failure for the tests with the centre tensiometer in place, given the measurements of the area and the moisture content of the specimen after failure.

Figure 2-8 shows the correlation between the water content at failure (w_f) and the percentage area increase after failure occurs. The change in area ΔA, was calculated from the following:

$$\Delta A = 0.4882 \cdot w_f - 6.134 \quad [2.1]$$

The cross-sectional area of the sample immediately before failure (A_f) was therefore calculated as follows:

$$A_f = h_m \cdot w_m \cdot \left(100 - \left(\left(48.82 \cdot w_f\right) - 6.134\right)\right) \quad [2.2]$$

where h_m and w_m are the measured height and width of the specimen after failure has occurred and w_f is the moisture content of the specimen at failure.

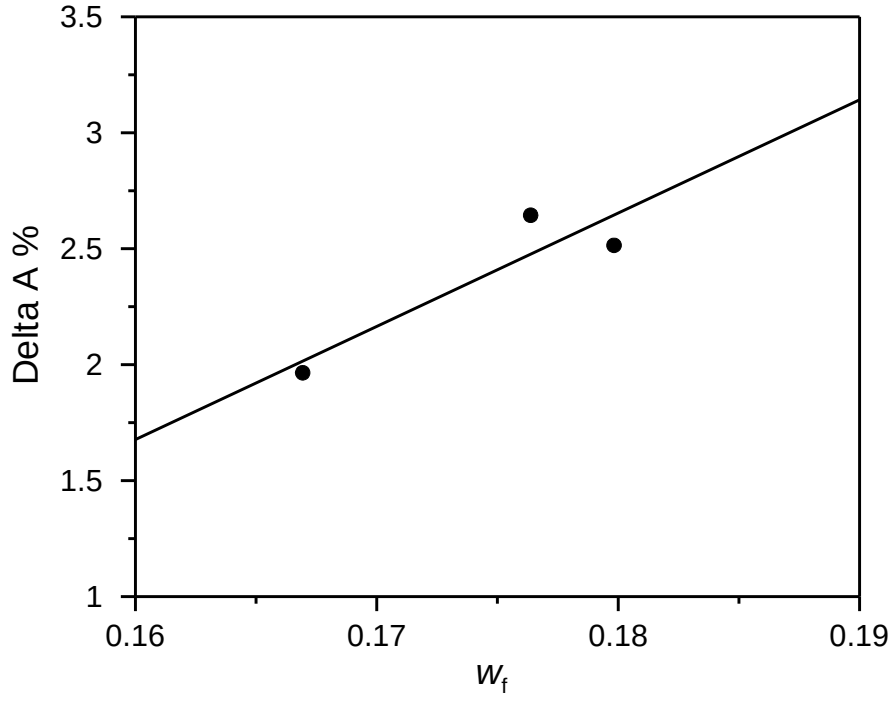

Figure 2-8 Method for area correction for uniaxial tension test

2.7.2 Uniaxial compression test

As there was no tensiometer in the centre section, the loading procedure was altered to allow for the propagation of the change in suction to reach the tensiometers in the end section. The specimen was loaded in steps and the duration of each step was determined by the time taken for the tensiometer readings to stabilise following an increase in load, i.e. rate of change measured by the tensiometers matched that of rate recorded prior to loading (accounting for baseline evaporation). The load was applied in steps of 4.9, 9.8, or 19.6N and the time required for the pore-water pressure to equalise ranged between 12 and 30 min. As there was no centre tensiometer it was possible to measure the cross-sectional area of the centre section throughout the test with callipers.

A procedure similar to the uniaxial tensile test was adopted to glue the specimen to the loading ends and to install the tensiometers. The only exception was the use of petroleum jelly to cover the specimen during the curing stage. At the time of the compression test it was not yet

known that the petroleum jelly was causing errors in measured water content.

Two specimens having initial water content of 0.197 and 0.185 respectively were tested. The specimen with initial moisture content of 0.197 was loaded in steps of 4.9N (≈15kPa) with each load maintained for 12 minutes (sufficient to ensure pore-water pressure equilibration). The specimen with initial moisture content of 0.185 was loaded in steps of 19.6N (≈60kPa) every 30 minutes until the stress conditions were equivalent to a friction angle of 20°, then in steps of 9.8N ((≈30kPa) until rupture. The increment in loading was changed as the specimen approached failure to increase the precision of the applied load required to cause the specimen to rupture. Prior to each increase in load the dimensions of the cross section of the centre section were measured with callipers. The test was considered to have failed correctly if the sample did not buckle in any direction prior to failure. After failure, a piece of the centre section was placed into the oven for 24hrs to obtain the moisture content.

2.8 Results

2.8.1 Evolution of pore-water pressure during the test

The results of 3 uniaxial tensile tests are shown in this paper. Figure 2-9 shows the evolution of pore-water pressure for the specimen tested at w=18.9% (calculated from relationship between moisture content and pore-water pressure using readings from tensiometers immediately before application of first load, p'_0=262kPa). After the installation of the three tensiometers (two at the ends and one in the middle) the equilibrium was reached after about 200 minutes for the middle tensiometer, and 400 minutes for the fixed and load tensiometers. To minimise evaporation during this period water evaporation was prevented by using the Parafilm®, cling film and plastic cover as described previously.

At t~970mins, the cling film and the plastic cover were removed (leaving the Parafilm®

layer in place). A decrease in pore-water pressure was observed due to the disturbance of the specimen. After a short time, the pore-water pressure recorded by the tensiometers recovered and all 3 tensiometers recorded a similar rate of change of pore-water pressure (baseline evaporation). The specimen was finally subjected to a tensile uniaxial stress at t≈1052 min. The load and fixed tensiometers show consistent measurement and recorded a decrease in pore-water pressure upon tension. The middle tensiometer recorded a greater decrease in pore-water pressure, which has been seen in the majority of tests performed. The pore-water pressure recorded by the centre tensiometer was then used to quantify the changes in isotropic effective stress during the tensile test, the other two tensiometers were used to validate the measurement of the centre tensiometer.

Figure 2-10 shows the evolution of pore water pressure recorded by the tensiometers for the uniaxial compression test shown in this paper. After installation, equilibrium between the 2 tensiometers and the specimen was reached after approximately 100 minutes. At approximately 160 minutes the plastic container and film were removed from the specimen, leaving the coating of petroleum jelly in place. The specimen was left for a further 60 minutes to obtain the baseline evaporation. The baseline evaporation in the uniaxial compression test was higher than that of the uniaxial tensile tests, due to the parafilm layer being a more effective method of preventing evaporation. The specimen was then loaded as described in the previous section until rupture occurred. The pore water pressure recorded by the 2 tensiometers shows an increase in pore-water pressure immediately following an increase in load, followed by a subsequent decrease as the pressure equilibrates and returns to the baseline evaporation rate.

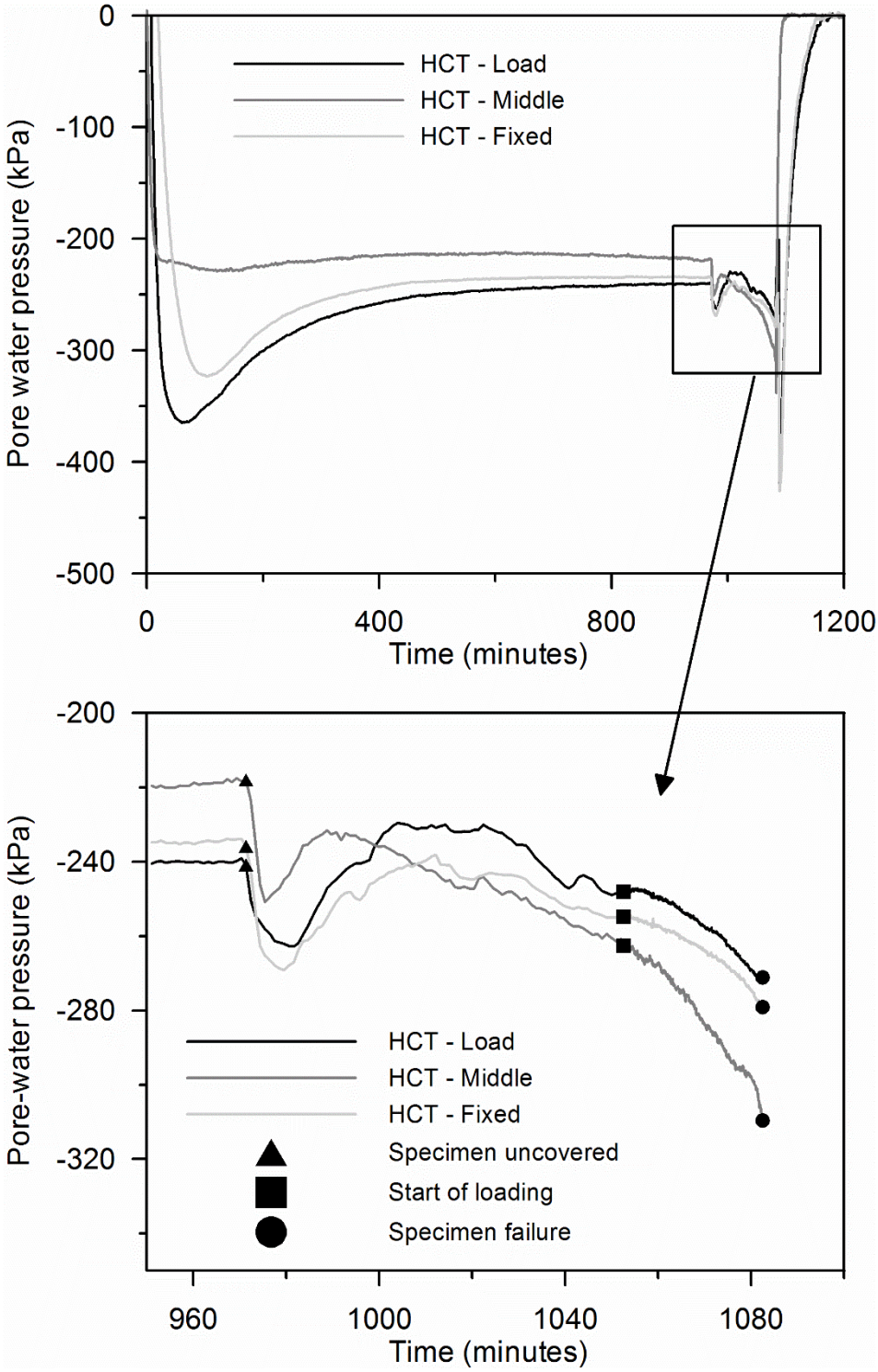

Figure 2-9 Evolution of pre-water pressure recorded by the tensiometers in uniaxial tensile test

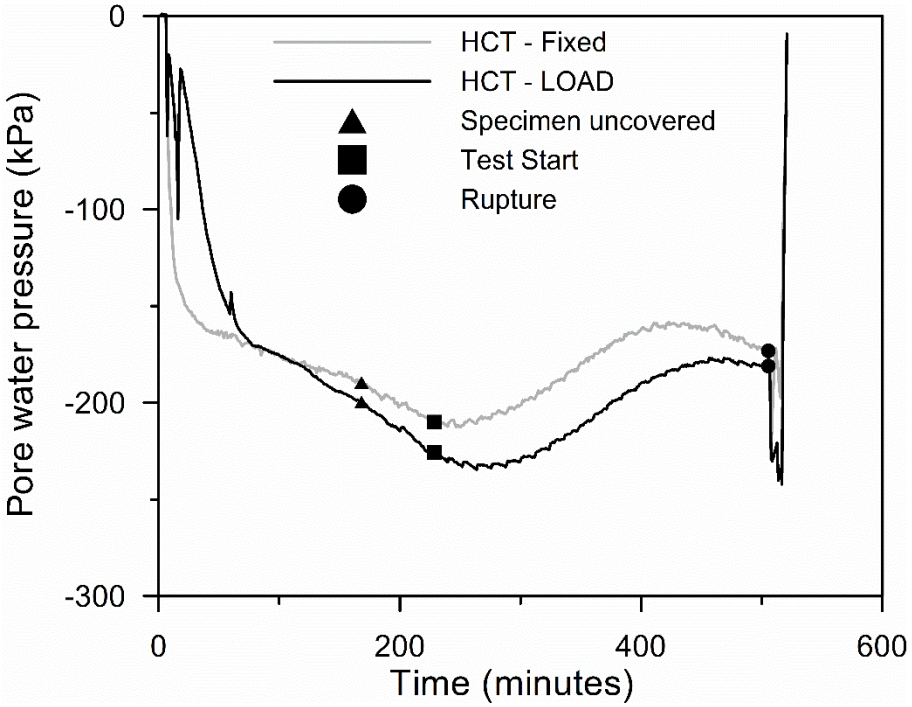

Figure 2-10 Evolution of pore-water pressure recorded by the tensiometers in the uniaxial compression test

2.8.2 Critical state data

The effective mean stress, *p*', versus deviator stress, *q*, paths for the 3 uniaxial tensile tests, the uniaxial compression tests and a standard CU triaxial compression test are shown in Figure 2-11. Where p' and q are calculated from the following, assuming triaxial conditions:

$$p' = \frac{\sigma'_a + (2\sigma'_r)}{3} \qquad [2.3]$$

$$q = \sigma'_a - \sigma'_r \qquad [2.4]$$

where σ'_a and σ'_r are the axial and radial effective stresses.

The deviator stress for the uniaxial tensile tests have been adjusted to allow them to be

directly compared to the compression test data using Equation 2.5:

$$q = \frac{M_c}{M_e}(\sigma'_r - \sigma'_a) \quad [2.5]$$

where M_c and M_e are critical state soil parameters defining the gradient of the critical state line in compression and extension respectively in the q:p' plane. M_c was calculated from the best fit critical state line of the compression tests and M_e was the q:p' ratio from each of the uniaxial tests at failure.

It can be observed from Figure 2-11 that using Eq 2.5 the uniaxial tensile test specimens reach the failure envelope created by best fitting the compression test failure points. The failure envelope is associated with a friction angle, φ', of 27.8°, which is linked to M_c from the following:

$$sin\ \varphi' = \frac{3M_c}{6 + M_c} \quad [2.6]$$

In the volumetric plane, the uniaxial compression specimen data point lies above the normal consolidation line for the soil. This fault has been attributed to use of petroleum jelly, as the same issue was recorded with early uniaxial tensile tests and ceased when Parafilm was used as a covering instead of Vaseline. The data points for the uniaxial tensile specimens are all on or close to the critical state line. The critical state line was created from triaxial compression tests.

The consistency of the results for the uniaxial tensile tests specimens shown, in both the p'-q and the volumetric plane, with respect to the compression tests act as validation for both

the testing apparatus and experimental procedure for the investigation of soil behaviour in tension.

The water contents from the uniaxial tensile test taken immediately after rupture from the centre and the two ends of the specimens from beside the specimen-adhesive boundary, are shown in Figure 2-12. The results show that the water contents of the samples taken from the centre section of the specimen, where the failures occurred, was lower than that of the end sections at the adhesive-specimen boundary. Figure 2-9 shows the tensiometer response during a test. The pore water pressure in the centre section decreased more than at the ends of the specimen. This response was recorded in the majority of the specimens tested. Considering this pore-water profile it would be expected that the lower pore water pressure in the centre section would create a water flow from the ends to the centre, resulting in higher water content in the centre.

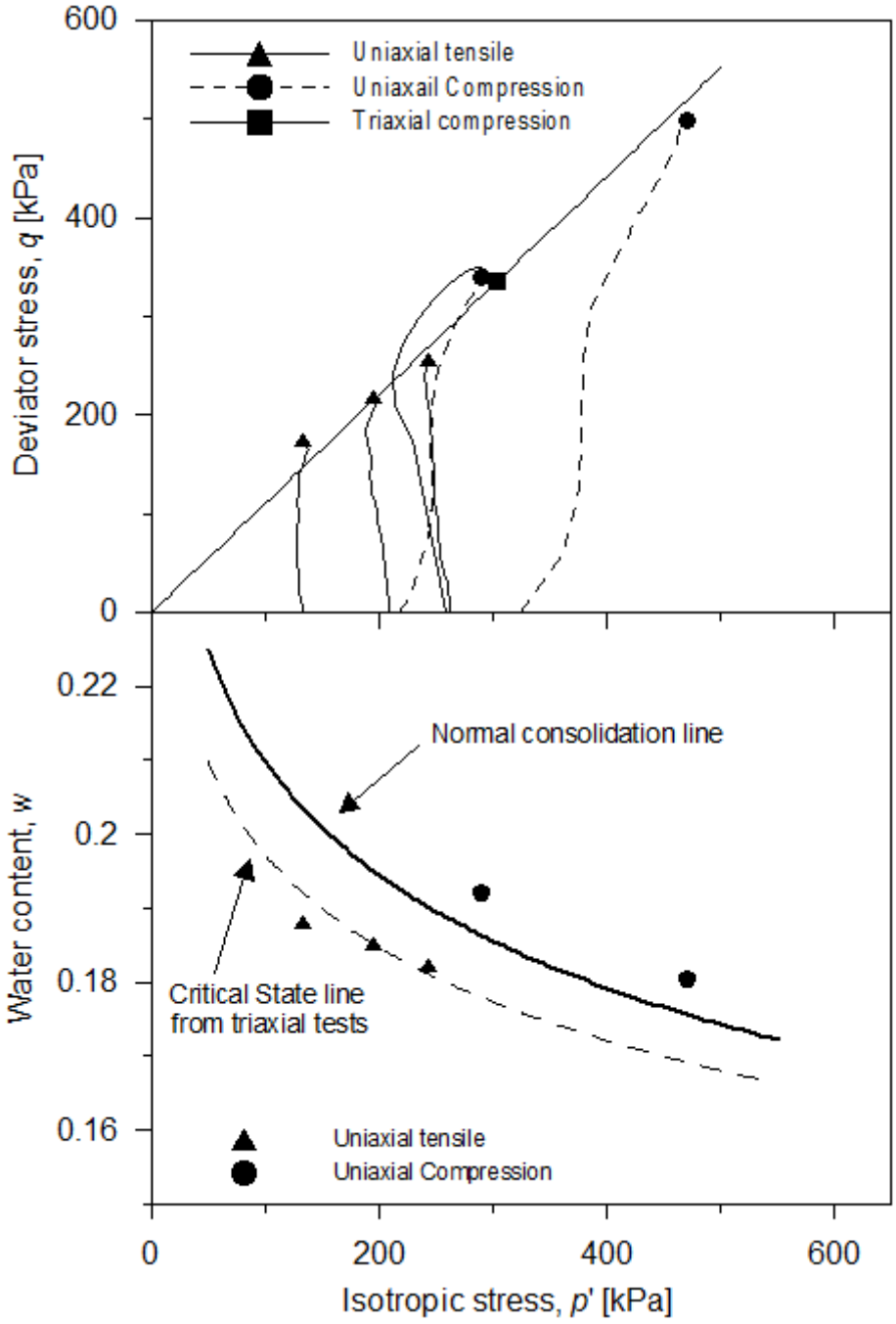

Figure 2-11 Critical state for uniaxial tension, uniaxial compression and triaxial compression test

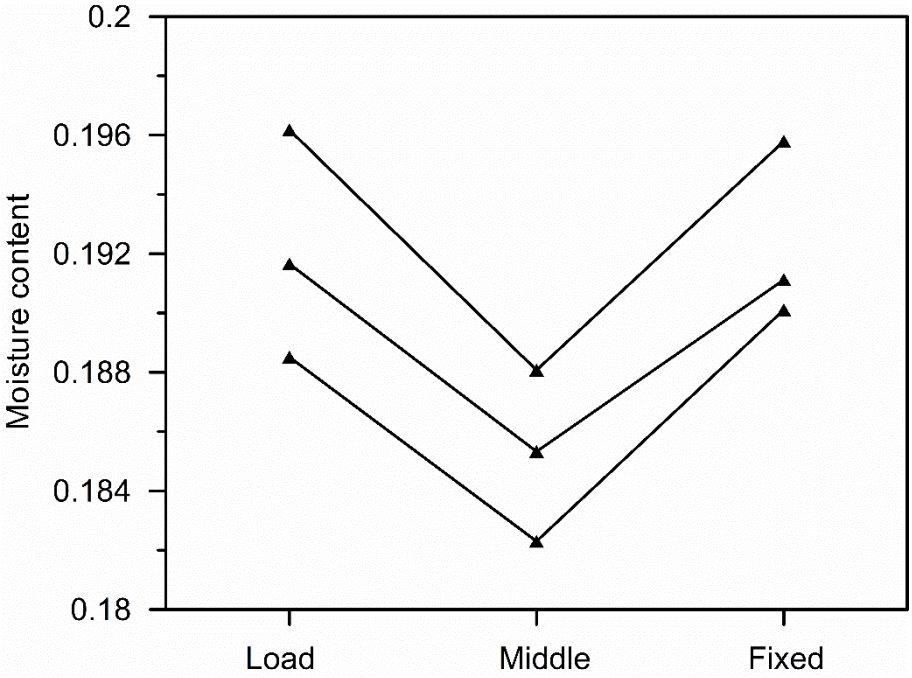

Figure 2-12 Moisture content at different specimen locations at failure for uniaxial tension tests

As mentioned previously it was not possible to prevent all of the evaporation from the specimen. In order to check whether the lower water content in the centre was due to this evaporation a 'mock' test was performed. A specimen was installed as per normal procedure. At the point where in a standard test the specimen would be loaded the specimen was left unloaded for the period of time required to carry out a normal test. The water contents of the specimen were then measured. The water contents for the three locations were within a small range of each other. The change in water content can therefore be assumed to be due to the effect of the negative total stress applied during testing.

To investigate the water content issue further the test was modelled via Finite Element Method (GeoStudio) using the Modified Cam-Clay constitutive model. For reasons of symmetry only half of the specimen was modelled.

In this simulation, the specimen was initially subjected to a suction of 350kPa. The

specimen was then subjected to a deviatoric stress by applying a constant rate of axial extension of 0.2mm per time step. The specimen was modelled as being fully undrained. The model boundary conditions and parameters before the deformation was applied are shown in Figure 2-13 and Table 2-1 respectively.

Figure 2-14 shows the stress path in the centre of the specimen, as well as the pore water pressure at intervals of height in the specimen for each time step. It can be seen from the figure that as shearing occurs the pore water pressure in the centre of the specimen increases significantly, while the pore water pressure at the ends of the specimen shows a small decrease. The difference in magnitude of the increase in the centre to the decrease in the ends can be attributed to the relative size of the sections.

The increase in pore water pressure in the centre of a specimen shown in Figure 2-14 would result in a flow of water from the centre of the specimen to its ends. Although the sample is globally undrained, local drainage may occur within the specimen. The Modified Cam-Clay simulation has therefore justified the water content profile found in the specimen at the end of testing.

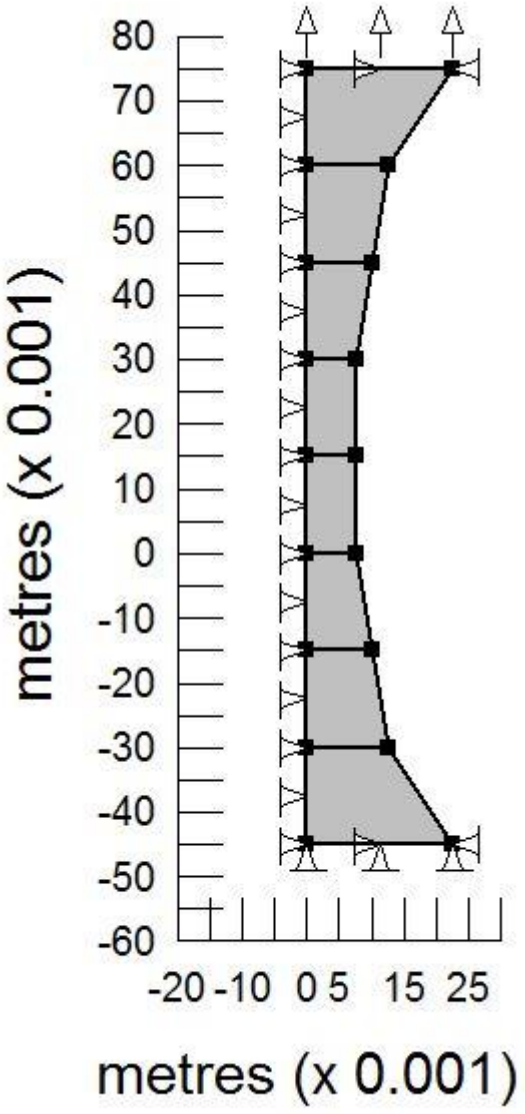

Figure 2-13 Boundary conditions adopted in uniaxial test simulation

Table 2-1 Parameters of Cam-clay model

Parameter	E (kPa)	ν	e_0	λ	κ	ϕ'	θ
Value	1000	0.334	0.353	0.0789	0.0132	27.8	0.5248

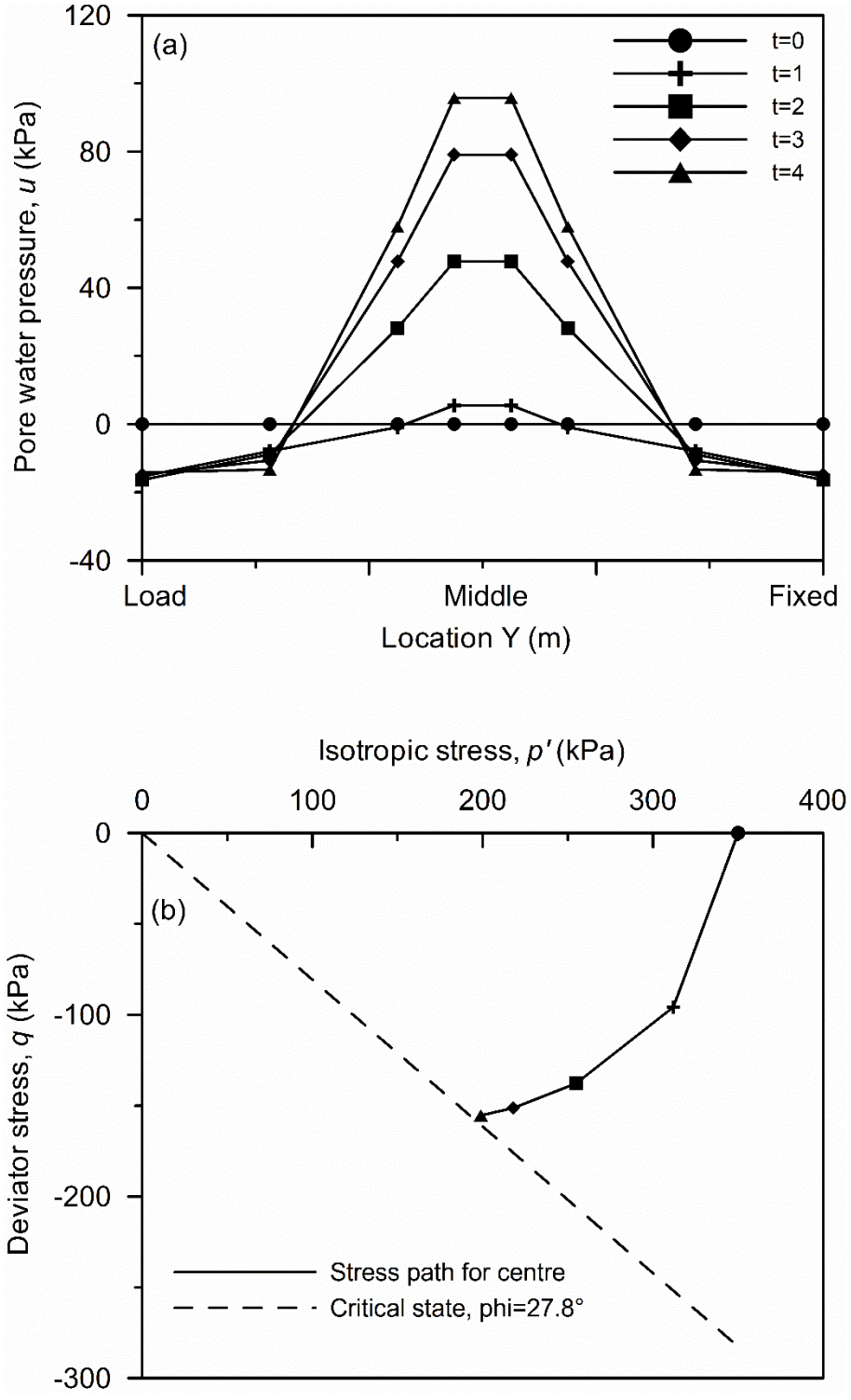

Figure 2-14 Results of uniaxial test simulation. (a) evolution of pore-water pressure with time. (b) stress path in the p'-q plane

2.9 Conclusions

This paper has presented a new apparatus for investigating the behaviour of clayey geomaterials subjected to a tensile (negative) total stress. A key feature of the apparatus is the facility to monitor the negative pore-water pressure using high capacity tensiometers. This allows interpretation of the failure data in terms of effective stress rather than total stress. The specimen shape has been designed to ensure that the direction of the major principal stress in the failure zone coincides with the direction of the externally applied tensile force, allowing for a more accurate analysis of tensile failure. The loading rate has been validated by testing specimens at a different loading rate and a simple method has been implemented to assess the cross-sectional area of the specimen at failure.

Results are shown for saturated specimens and compared to results obtained for the same soil in uniaxial compression, using a modified version of the presented uniaxial tensile method, and a triaxial compression test. It is demonstrated that that crack initiation occurs by shear failure if data are interpreted in terms of effective stress rather than total stress and that the failure mechanisms under tension do not differ from compression.

2.10 Acknowledgements

The authors wish to thank Ideal Standard International for supporting the research as well as Derek McNee for his help constructing the test apparatus.

3 MECHANISMS OF CRACK INITIATION IN CLAYEY GEOMATERIALS UNDER SATURATED AND UNSATURATED CONDITIONS

3.1 Abstract

The paper presents an experimental investigation into the mechanisms of crack initiation in clayey geomaterials under saturated and unsaturated conditions. An experimental apparatus was developed to test specimens in uniaxial tension with the facility to monitor suction using high-capacity tensiometers. A first series of tests were performed on saturated clay samples prepared using non-de-aired water. When suction approached the air-entry value, failure occurred at a deviatoric stress lower than the one corresponding to the critical state line derived from triaxial and uniaxial compression tests. A second series of tests were performed on saturated specimens with the slurry preventively de-aired before slip casting. Indeed, the de-airing process realigned the deviator stress at failure recorded in the tensile test with the critical state line derived from uniaxial and triaxial compression tests. It could therefore be demonstrated that water cavitation is one of the mechanisms that can control rupture of clay when subjected to a (total) tensile stress state. Finally, failure data on unsaturated specimens could be fairly modelled by the Mohr-Coulomb criterion extended to unsaturated states confirming that tensile failure is associated with failure in shear for both saturated and unsaturated states.

3.2 Introduction

The development of cracks in geomaterials exposed to drying is an important issue in many geotechnical engineering applications due to the effects that cracks have on the mechanical and hydraulic properties of a soil. The presence of tension cracks influences the stability of natural slopes (Baker 1981) and earth structures like flood embankments due to water seeping directly into the desiccated crest of the flood embankment (Marsland & Cooling, 1958; Marsland, 1968; Dyer, 2005). Cracks significantly increase the hydraulic conductivity of clayey soils, providing a preferential pathway for fluid transport. This can be particularly problematic where the soil has been used to provide a hydraulic barrier, e.g. landfill liners and earth dams (Albrecht & Benson, 2001). Desiccation cracks are also important in other fields, including the ceramic industry. In the production of sanitaryware products, slip cast forms are left to dry at ambient temperatures. During the drying process cracks can develop in the wares (Cooper, 1978). The loss of wares attributed to desiccation cracking is quantified at 5-10% of the total production (Tarantino et al., 2010).

Various numerical methods have been developed to simulate the initiation and propagation of cracks within geomaterials exposed to drying. These include methods based on the linear elastic fracture mechanics (Morris, 1992; Konrad & Ayad, 1997; Prat et al., 2008), discrete/distinct element method (Peron et al., 2009; Amarasiri et al., 2010; Sima et al., 2014), and finite element methods with the possible incorporation of interface elements (Rodriguez et al., 2007; Sanchez et al., 2014). The majority of these methods assume that crack initiation occurs when the soil tensile strength is exceeded by the tensile stresses present in the geomaterial. Even in the case of the application of Discrete Element Methods, the micro-parameters of the model, i.e. the contact bond strengths, are inversely determined by matching

the tensile strength in a uniaxial tensile test.

The assumption that crack initiation is associated with the mobilisation of a tensile strength implies that the formation of cracks in geomaterials occurs in Mode I. In addition, the tensile strength is always associated with a ‘total’ stress, i.e. the mechanical behaviour of the geomaterial, including the crack initiation, is modelled in terms of total stress. This is not very intuitive considering that crack initiation in geomaterials prepared from slurry often occurs at the transition from saturated to unsaturated states upon a drying process (Bowman, 1926; Clews, 1969; Peron et al., 2007). In the saturated state, one would expect the response of clay to be modelled in terms of effective and not total stress.

Indeed, Thusyanthan et al. (2007) have demonstrated that crack initiation is controlled by the effective normal stress, as is the case for failure of geomaterials in compression. Similar arguments have been provided by Shin and Santamarina (2011). In addition, Thusyanthan et al. (2007) have shown that failure occurs in shear rather than tension, in the sense that crack initiation is controlled by the combination of isotropic and deviatoric stresses, rather than a threshold value of (negative) minimum principal stress.

Thusyanthan et al. (2007) have characterised the mechanisms of crack initiation in saturated geomaterials but the question still remains open about the mechanisms of crack initiation in unsaturated geomaterials. Lakshmikantha et al. (2012) and Varsei et al. (2016) have implicitly suggested that crack initiation in unsaturated geomaterials can be modelled in terms of ‘average skeleton stress’ as discussed by Tarantino (2007) and Tarantino and El Mountassir (2013). However, there is not any experimental evidence of the validity of such an assumption.

This paper shows an experimental programme with the aim of clarifying fundamental aspects of tensile cracking. Tests include a new direct method of tensile testing using high capacity tensiometers to measure specimen suction during testing.

3.3 Materials and specimen preparation

3.3.1 Materials used

Two materials were used in the experiments, Speswhite kaolin (SK, silty clay) and a material mix commonly used in the ceramics industry, Vitreous China (VC). The grain size distributions of these materials are shown in Figure 3-1.

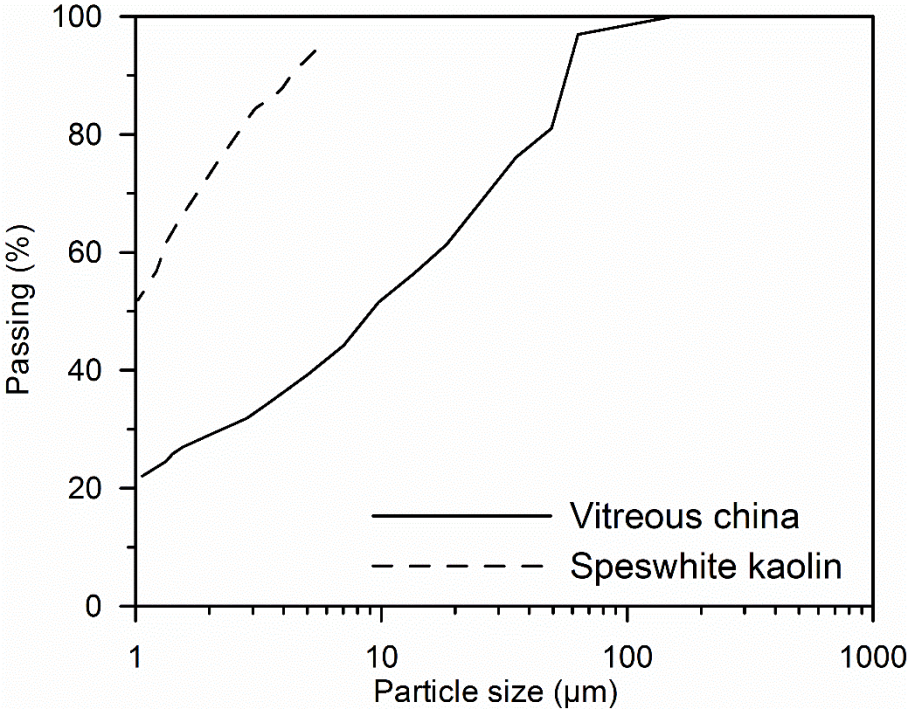

Figure 3-1 Grain-size distribution of tested materials

3.3.2 Preparation of non-de-aired samples

Specimens were prepared by slip casting in plaster moulds. The suction possessed by the plaster removes water from the liquid slip to create a plastic specimen. Plaster moulds were used because they could repeatedly form specimens of complex shape in a relatively short time. The moulds for the uniaxial tensile/compression and triaxial specimens created a specimen of the required shape for testing, whereas the mould for the water retention curve creates a large

bar from which specimens were made using a cutting ring.

The VC slip was obtained by mixing different 'ingredients', each component included to influence the behaviour of the overall mix that make it suitable in the production of sanitaryware products. To ensure consistent specimens a large quantity of the VC slip was prepared prior to beginning the experimental programme by mixing the dry powdered constitutive parts with demineralised water to moisture content of approximately 0.30. The slip was stored in an air tight container for the period of the experiments. Individual specimens were prepared by taking a portion of the slip, which had been mixed for 30 minutes, and adding de-mineralised water to reach the required density (1.84kg/l, w≈0.35).

The Speswhite kaolin was supplied in the form of dry powder. The slip was prepared before each experiment by mixing the kaolin powder with demineralised water to moisture content of approximately 2.5 (250%).

The slip was added to the plaster mould. The time required to dry the VC slip in the mould varied depending upon which specimen shape is being made. Specimens for uniaxial tensile/compression tests required 90 minutes, specimens for triaxial tests required 150 minutes, and specimens for water retention curve required 120 minutes. Upon removal from the mould the moisture content of the specimens was in the range of 0.2-0.21, corresponding to an initial negative pore-water pressure of approximately 100kPa.

The time required to dry the slip of SK was higher due to the higher initial water content of the slip and hence larger volume of water to be removed by the moulds (tensile/compression 120 minutes, triaxial 180 minutes, water retention curve 150 minutes). Upon removal from the moulds the moisture content was 0.54, corresponding to an initial negative pore-water pressure of approximately 100kPa.

Specimens were air dried, where necessary, to target moisture content for the required test,

sealed and stored for 24 hours prior to testing to obtain an equilibrium in the moisture content throughout the specimen.

3.3.3 De-aired samples

The SK and VC slips, prepared to the correct density/moisture content, were added into a vacuum chamber. The vacuum chamber was placed on top of a stirring plate and a stirring rod added to the slip. A vacuum pressure of 100kPa was applied to the chamber for a period of one hour. The slip was stirred continuously throughout the de-airing process. At the end of the de-airing process no more bubbles of air were being released from the slip. The slip was then cast immediately in the plaster moulds, stored and air-dried as described previously for the non-de-aired specimens.

3.4 Equipment

3.4.1 High-Capacity Tensiometer

The measurement of matric suction was performed using high capacity tensiometers (Tarantino & Mongiovi, 2002). The tensiometers are comprised of a water reservoir, a high air entry ceramic disk (1.5MPa) and an integral strain gauge diaphragm.

3.4.2 Chilled Mirror Psychrometer

Measurement of suction beyond the range of the tensiometers was done using a WP4C water potential meter. The WP4C uses the chilled mirror method to determine the relative humidity of the air around a sample in a sealed chamber once the sample has come into equilibrium with the vapour in the surrounding air. At the dew point the WP4C measures the temperature of the sample and the surrounding air. Calibration of the device was achieved by

using sodium chloride solutions with known water potentials.

3.4.3 Uniaxial tensile test apparatus

The tensile test is designed as a direct test giving control over the applied axial total stress and uses high capacity tensiometers to measure the matric suction of the specimen throughout testing, therefore allowing for an effective stress based analysis of the results. The test is similar in concept to that developed at the Soil Mechanics laboratory at Polytechnic University of Catalonia (UPC) Rodriguez (2002), but has some significant modifications. The test specimen has a centre section with a cross sectional area equal to one third of that at the ends. This results in a higher axial stress within the central area, and failure subsequently occurs in this centre section. The end sections are curved towards the centre section, resulting in a smooth transition between the centre section and curved section. This results in less shear stresses being present under loading than the equipment proposed by Rodriguez (2002). The specimen is fixed, using a glue, at one end to a rigid restraint and at the opposite end to a rigid plate from which a hanger is attached via a low friction wheel. The specimen is placed on top of a layer of ball bearings to reduce frictional effects and allow the sample to deform during loading. Parafilm was used to cover the specimen during glue curing and testing to control and reduce as much as was possible the evaporation from the specimen. Each test used three tensiometers to measure the suction of the sample. The tensiometers were placed onto the surface of the specimen, not embedded within it. One was secured to each end of the sample and a third was located in the centre section. The suction measured by the centre tensiometer was used in the test analysis. The tensiometers at the ends were used to check the consistency of the suction measured by the centre tensiometer. The specimen shape, thickness of 1.5cm, and schematic of the equipment is shown in Figure 3-2 and Figure 3-3 respectively.

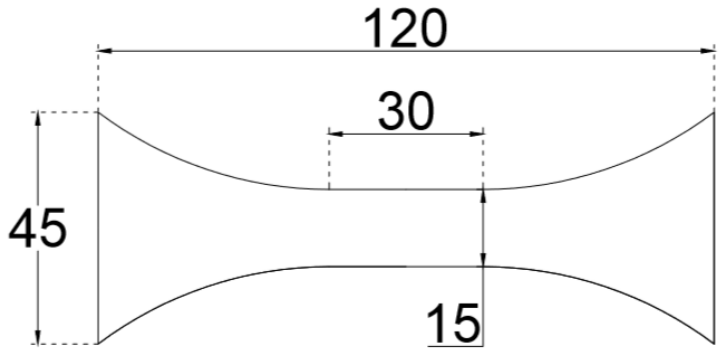

Figure 3-2 Specimen shape and dimensions (mm)

3.4.4 Uniaxial compression test apparatus

The purpose of the compression test was to derive the critical state parameters for the VC and SK materials in compression for the purpose of comparison with the parameters derived from extension tests. The equipment and procedure were very similar to the tensile test, with some modifications, see Figure 3-4. The loading system was modified to apply the load in compression. The loads required to reach failure in the sample were significantly greater than those for the tensile test. To accommodate the increase in load the tensile test apparatus was mounted for convenience inside the tensile test apparatus of Rodriguez, 2002. The test also only used the two tensiometers located at the ends of each sample. A tensiometer in the centre section was tried but it was not possible to maintain a good connection between the tensiometer and the specimen throughout loading. As there was no tensiometer in the centre section the rate of loading was altered to allow for the propagation of the change in suction to reach the tensiometers in the end sections. The time required for this was determined by the time taken, following an increase in load, for the tensiometer readings to stabilise, i.e. rate of change measured by the tensiometers matched that of rate recorded prior to loading due to evaporation.

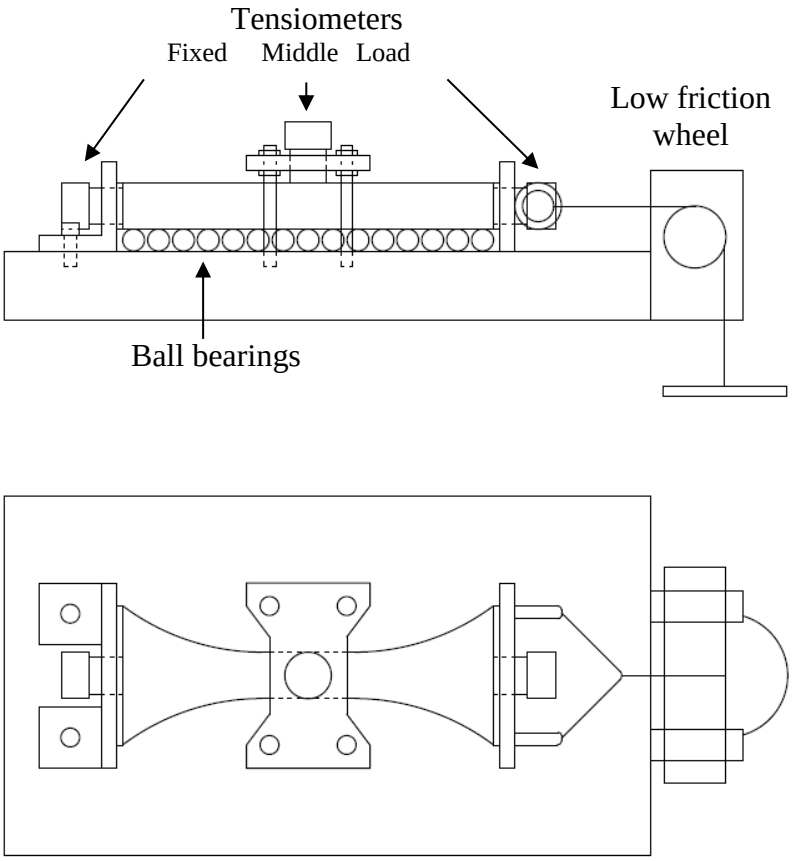

Figure 3-3 Apparatus for uniaxial tension test

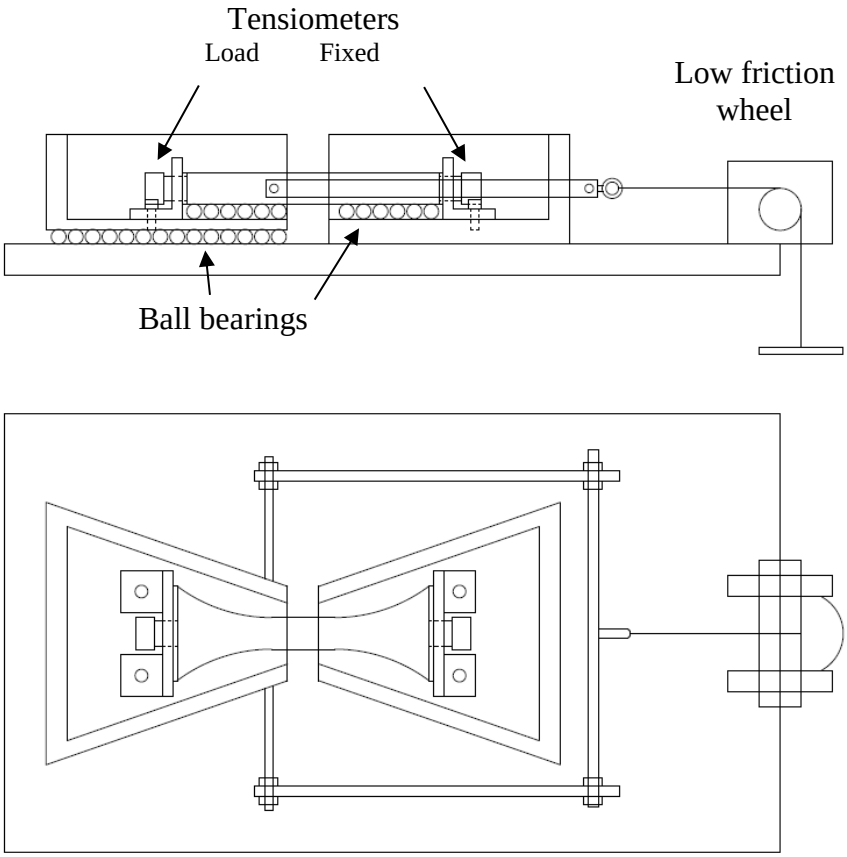

Figure 3-4 Apparatus for uniaxial compression test

3.4.5 Triaxial cell apparatus

A conventional triaxial apparatus accommodating a 38mm diameter and 76 mm high specimen was used to investigate the response of clays under confined compression. The cell had a fixed pedestal and was loaded axially through a rigid top cap. An internal submersible load cell was used to measure the axial load. For the drained stage of the test, a volume gauge was connected to the drainage line to measure volume change, and in turn connected to a pressure regulator via an air-water bladder cell to impose a target pore-water pressure. The cell was connected to a pressure regulator via an air-water bladder cell to control the cell pressure. The cell was mounted in a loading frame to apply a constant displacement rate during shearing.

3.5 Experimental procedures

3.5.1 Water retention curve

The bar from the slip casting was air-dried to the required water content and stored to ensure equilibrium of the water content throughout the soil. A 50mm diameter metallic cutting ring was used to cut a specimen from the bar. The specimen was placed inside a sealed box and the (negative) pore-water pressure measured using two high-capacity tensiometers (Tarantino et al., 2009). At the end of the measurement, the sample was placed into the oven for 24hrs at 105°c to give the moisture content related to the matric suction.

When the pore-water pressure was beyond the measurement range of the tensiometers, specimens of approximately 1 cm^3 were cut from the cast bar and placed into the WP4C. At the end of the pore water pressure measurement the specimens were placed into the oven for 24hrs at 105°c to give the moisture content related to the total suction. The relationship between moisture content and suction is shown in Figure 3-5.

Because it was not possible to measure accurately the volume of the specimens used for tensiometer and psychrometer measurements, the degree of saturation of the specimens tested was assessed by establishing independently a relationship between degree of saturation and water content along a main drying path. To this end, a cast bar was left to air-dry, and a smaller cutting ring 16 mm diameter and 12.5 mm high was used to cut small specimens at different stages in the drying process from the same bar. The cutting ring was pushed into the sample slowly using a loading frame to prevent the soil cracking. The top and bottom of the specimen was carefully trimmed to give the specimen the same volume as the cutting ring. The specimen was then placed into the oven for 24hrs at 105°c to obtain the water content. The inner volume of the cutting ring allowed the calculation of the void ratio and hence, the degree of saturation

of each specimen. The relationship between degree of saturation and moisture content is shown in Figure 3-6.

The combination of these two tests allowed for the relationship between water content *w*, suction *s*, void ratio *e*, and degree of saturation S_r to be developed into the full 'main drying' water retention curve.

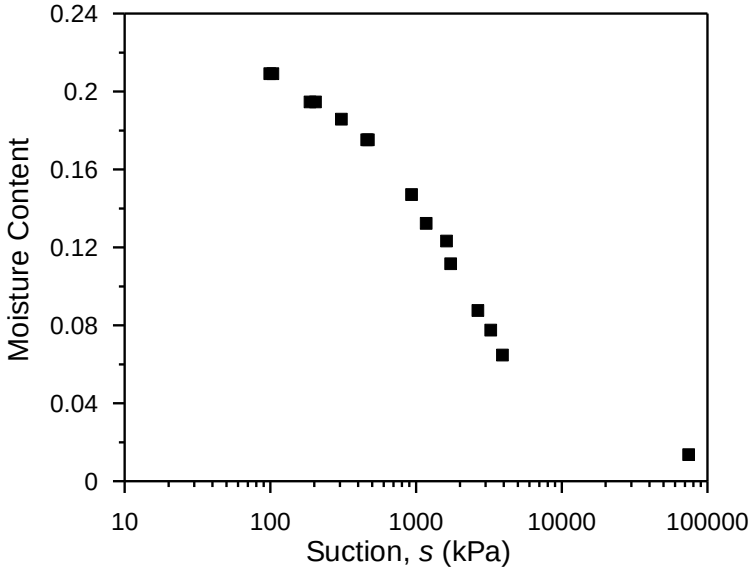

Figure 3-5 Relationship between gravimetric moisture content and suction

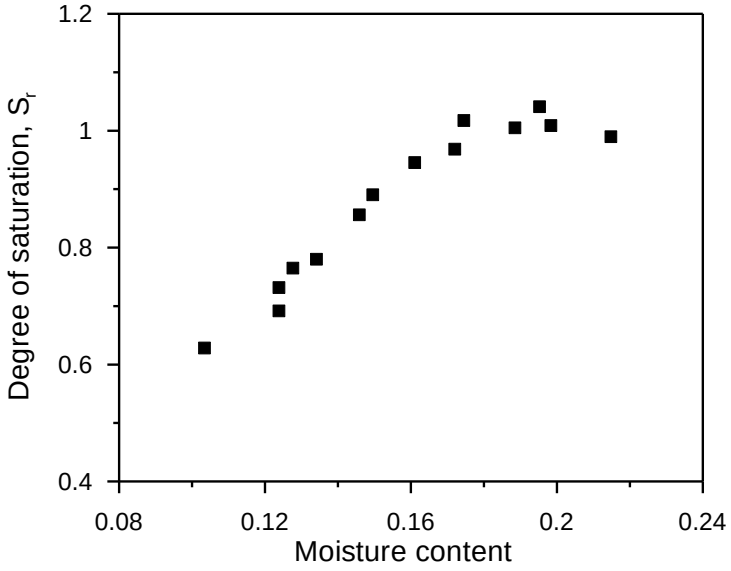

Figure 3-6 Relationship between gravimetric moisture content and degree of saturation

3.5.2 Tensile test

After removal from the plaster mould, specimens were air dried to the required moisture content and stored for 24hrs. To prevent evaporation during testing the sample was covered in Parafilm. A single piece of parafilm could not be stretched over the sample as this could provide a load path for the applied tensile load and increase the load at which the specimen fails. To overcome this problem multiple pieces of unstretched parafilm were used and then grease was used to adhere the pieces of parafilm to each other. The grease did not come into contact with the specimen. Due to the relatively complex shape of the sample it was not possible to create a completely effective barrier using parafilm to prevent all evaporation.

The specimen was placed onto the ball bearings and glued to the end restraints. Care had to be taken to align the specimen correctly to the restraints. The specimen and apparatus were covered in a film to prevent evaporation from the holes for the tensiometers and then a plastic box was placed ontop. The relative humidity of the air inside the box was raised to help reduce evaporation from the specimen. The test was left for 12hrs to allow for the glue to fully cure. After curing the 3 tensiometers were placed onto the specimen and secured. A small amount of soil paste was used to ensure a good contact between the tensiometer and the specimen. The test was again covered with the box while the tensiometers came into equilibrium with the specimen. Prior to loading the specimen was uncovered for a period of one hour to obtain a base evaporation rate. The specimen was loaded axially at a nominal rate of 1.96N/min (≈7 kPa/min) until failure occurred. After failure, a sample from the centre and each of the ends of the specimen was placed into the oven to obtain the moisture content at failure.

The loading rate of 7 kPa/min was validated by performing additional tests at a nominal loading rate of 23.5N/min (≈84 kPa/min). The results of these tests, shown in Figure 3-7, showed that the change in pore water pressure associated with a load step for the two load rates

was comparable (when a correction for base evaporation was added). The effective stress state at failure for the faster load rate specimens was also on the same failure envelope as the tests from the slower load rate indicating that the load rate used had no effect on the test. The 7kPa/min rate was then used for the tests as it allowed the operator easier control during loading.

Due to the centre tensiometer, it was not possible to measure the cross-sectional area of the centre section where the failure was occurring during the tests. The only measurement of size of the centre section possible was to measure the dimension immediately after the sample had ruptured. In order to relate the post rupture area to the area immediately before failure, which is required for the accurate calculation of the stress state at failure, tests were performed with the centre tensiometer removed and manual measurements of the area of the specimen taken during loading. The area after rupture was also taken allowing for a correlation to be established between the cross-sectional areas immediately before and after rupture. This test was performed for both the VC and SK soils at three different specimen moisture contents to create a best fit line relating the percentage area change to the final moisture content of the specimen. This best fit was used to calculate a cross-sectional area at failure for the tests with the centre tensiometer in place given the measurements of their area after rupture and the moisture content of the specimen at failure.

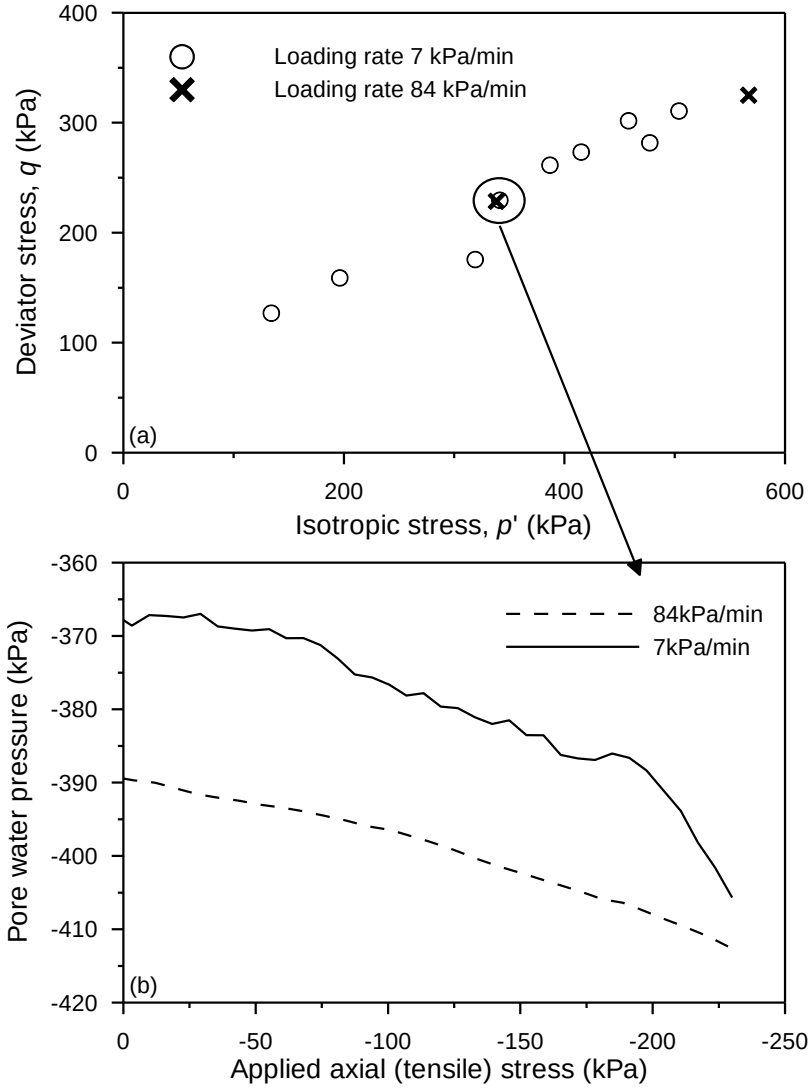

Figure 3-7 Comparison of uniaxial tension tests performed at different loading rates on VC samples. (a) Shear strength envelope in the plane isotropic effective stress p' versus deviator stress q (b) Evolution of pore-water pressure during shearing for two specimens tested at different loading rates

3.5.3 Uniaxial compression test

The same procedure as was used for the uniaxial tensile test was adopted to glue the specimen to the loading ends and to install the tensiometers. The only exception was the use of petroleum jelly, instead of Parafilm®, to cover the specimen during the curing stage. The

loading rate for the two tests performed were different, in order to reduce the total test time. The specimen with initial moisture content of 0.197 was loaded in steps of 4.9N (≈15kPa) every 12 minutes. The 0.185 specimen was loaded in steps of 19.6N (≈60kPa) every 30 minutes until the stress conditions were equivalent to a friction angle of 20°, then in steps of 9.8N ((≈30kPa) until rupture. The period between loading steps was sufficient to allow the change in the pore water pressure to be similar to that of the baseline evaporation prior to loading. Prior to each increase in load the dimensions of the cross-section of the centre section were measured with callipers. The test was considered to have ruptured correctly if the sample did not bend in any direction prior to failure. After failure, a piece of the centre section was placed into the oven for 24hrs to obtain the moisture content.

3.5.4 Triaxial compression tests

The triaxial apparatus was saturated for 12 hours prior to testing to dissolve any air bubbles and then flushed with de-aired water. Specimens were cut from the 38mm diameter cast bar to 76mm height and the off-cuts used to get an initial moisture content. The specimen was placed in the apparatus and adequate saturation checked by closing the drainage valve and applying an increase to the confining pressure. The value of the pore pressure coefficient B was calculated as follows:

$$B = \frac{\Delta u_w}{\Delta \sigma_3} \qquad [3.1]$$

where Δu_w is the change in pore water pressure recorded under water-undrained conditions upon the application of a change in cell pressure $\Delta\sigma_3$. A series of increases to the back pressure and confining pressure were applied until a value of B greater than 0.95 was obtained.

Specimens were consolidated under a cell pressure greater than that of the specimen suction, calculated from the initial moisture content to ensure that the sample was normally consolidated. Three tests were performed for both the VC and SK materials, at effective consolidation pressures of 60kPa, 259kPa and 529kPa for the VC and 59kPa, 253kPa and 516kPa for the SK. When the consolidation was complete the drainage valve was closed. A strain rate was calculated, using the procedure from Head (1986), based upon the consolidation time. This rate was 0.12mm/minute for all the tests, with the exception of the 60kPa VC specimen which was performed at 0.07mm/min. Testing was continued until the measured deviator stress no longer increased. At this point the cell was dismantled and the moisture content of the specimen tested.

The cross-sectional area, A, associated with the axial compression of a specimen under loading was calculated as follows:

$$A = \frac{A_0}{1 - \varepsilon_a} \qquad [3.2]$$

where A_0 is the sample cross-sectional area at the start of the test and ε_a is the axial strain.

3.6 Failure behaviour of non-de-aired samples in saturated state

3.6.1 Vitreous China (VC)

Two uniaxial compression tests under 'quasi-undrained' conditions were carried out on VC samples, having water contents at the start of loading of 19.7 and 18.5% respectively (estimated from the water retention curve and the initial measured suction). Figure 3-8 shows the evolution of pore-water pressure for the sample tested at w=19.7%). After the installation of the

tensiometers, the equilibrium was reached after about 90 min. The tensiometers then recorded a decrease in pore-water pressure due to the slight evaporation occurring from the sample despite the petroleum jelly coating. The sample was compressed uniaxially at t~240min. Both tensiometers recorded an increase in pore-water pressure with respect to the evaporation baseline, i.e. the change in pore-water pressure that would have been recorded if the specimen was not loaded. This response is consistent with the behaviour of normally consolidated clay subjected to undrained compression.

The stress paths in the isotropic effective stress *p'* versus deviator stress *q* plane for the two specimens tested in uniaxial compression are shown in Figure 3-9. The same figure also shows the stress paths for the specimens subjected to conventional CU triaxial compression test. Table 3-1 summarises the conditions of the samples at the start of shearing for the uniaxial compression and triaxial compression tests for both materials, where p'_0 is the effective mean stress. For uniaxial compression tests p'_0 is equal to the average matric suction recorded by the tensiometers and $w_0\%$ is the moisture content, calculated from the relationship between moisture content and suction as detailed in section 3.5.1. For triaxial compression tests w_0 is back calculated from the final moisture content accounting for the volume change during the consolidation process. The associated p'_0 value is calculated using the relationship between moisture content and suction established in 3.5.1.

The stress data points at the critical state form a linear envelope passing through the origin, corresponding to a gradient, M_c, as would be expected for a soil reconstituted from slurry. The corresponding critical state friction angle is φ'_{cs}=27.8°, calculated from:

$$\sin \varphi' = \frac{3M_c}{6 + M_c} \qquad [3.3]$$

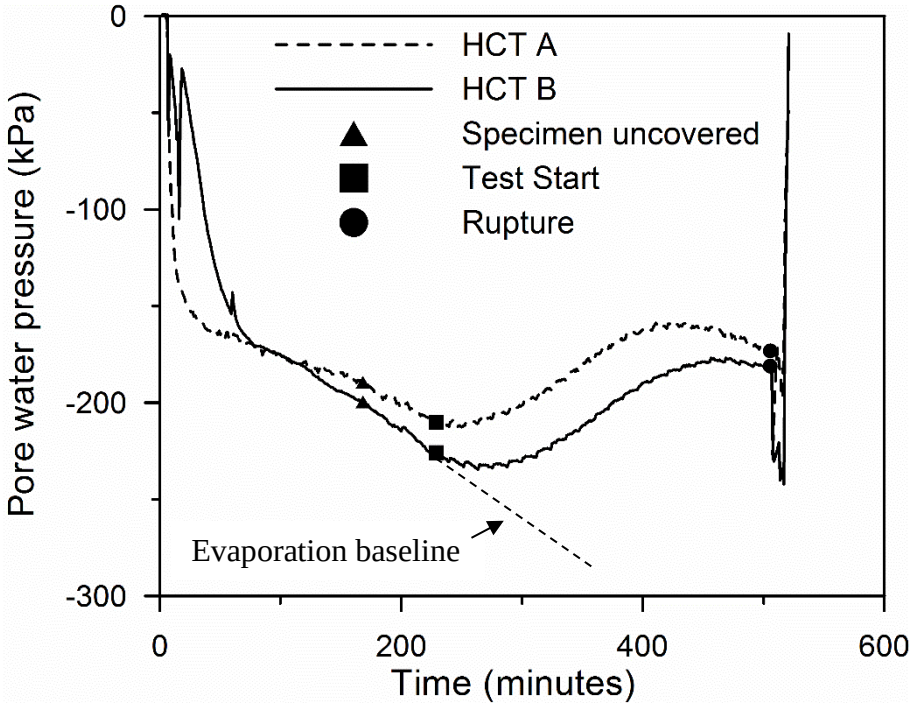

Figure 3-8 Evolution of pore-water pressure measured by the HCTs during the uniaxial compression test on VC (Test 05-06, w=19.7%).

Figure 3-9 also shows the critical state data in the compression plane together with the normal consolidation line (*ncl*) obtained from samples air-dried to target water content with suction measured using the tensiometers. The critical state data for the specimens tested in triaxial compression are located below the *ncl* as expected. On the other hand, the water content of the specimens tested in uniaxial compression were unexpectedly above the *ncl*. This was attributed to a water exchange during loading with the petroleum jelly, which was removed from the specimen before being placed in the oven, used to coat the specimen. For this reason, no petroleum jelly coating was used in the subsequent tensile tests.

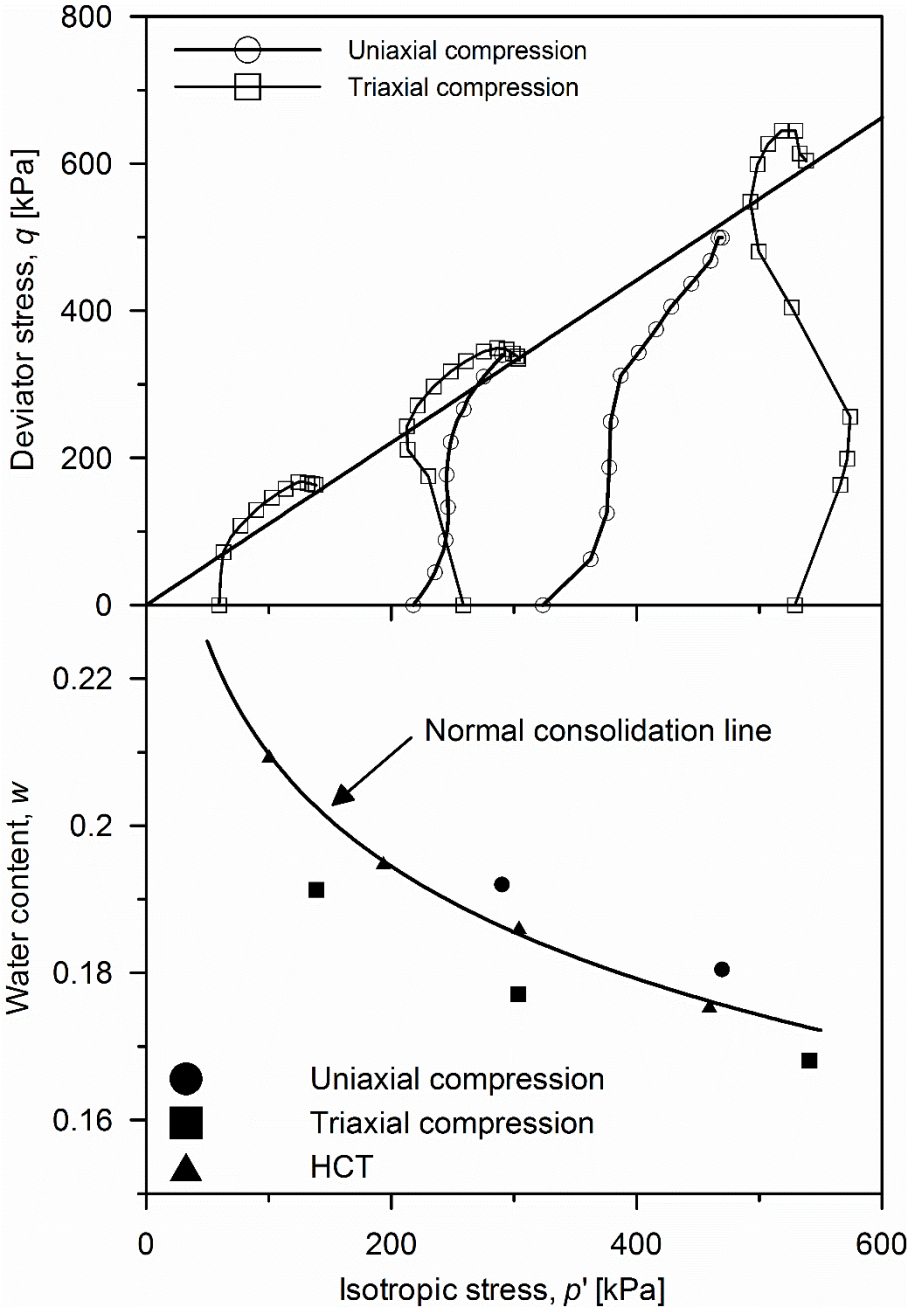

Figure 3-9 Stress-paths and water contents at failure for uniaxial and triaxial compression tests for VC

Table 3-1 Initial conditions for uniaxial compression and triaxial compression tests

	VC		SK	
	W_0 (%)	p'_0 (kPa)	W_0 (%)	p'_0 (kPa)
UC 1	19.7	218	-	-
UC 2	18.5	323	-	-
Triaxial 1	19.1	60	51.4	59
Triaxial 2	17.7	259	47.6	253
Triaxial 3	16.8	529	40.7	516

Nine uniaxial tension tests under 'quasi-undrained' conditions were carried out on VC specimens, having initial water contents ranging from 20 to 17%, calculated from the initial pore water pressures recorded by the tensiometers. All these samples were tested under saturated conditions. Figure 3-10 shows the evolution of pore-water pressure for the sample tested at w=17.7%. After the installation of the three tensiometers (two at the ends and one in the middle) an equilibrium was reached after about 120 min. To ensure that proper equilibrium was reached with the tensiometers, water evaporation was prevented by using Parafilm®, cling film and a plastic cover as described previously.

At t~200min, the cling film and the plastic cover were removed (leaving the Parafilm® layer in place) and a slight decrease in pore-water pressure was observed due to the slight evaporation occurring from the sample. This decrease in pore-water pressure was significantly less than the one observed on samples tested in uniaxial compression (Figure 3-8) due to the better insulation system created by the Parafilm®. The specimen was finally subjected to a tensile uniaxial stress t≈260 min. The three tensiometers showed consistent measurement and recorded a decrease in pore-water pressure upon tension.

The tensiometer installed in the middle of the specimen recorded a greater decrease in pore-water pressure and this has been the typical response for the majority of the tests. The pore-water pressure recorded by the centre tensiometer was then used to quantify the changes in isotropic effective stress during the tensile test, the other two tensiometers were used to check the consistency of the measurement of the centre tensiometer.

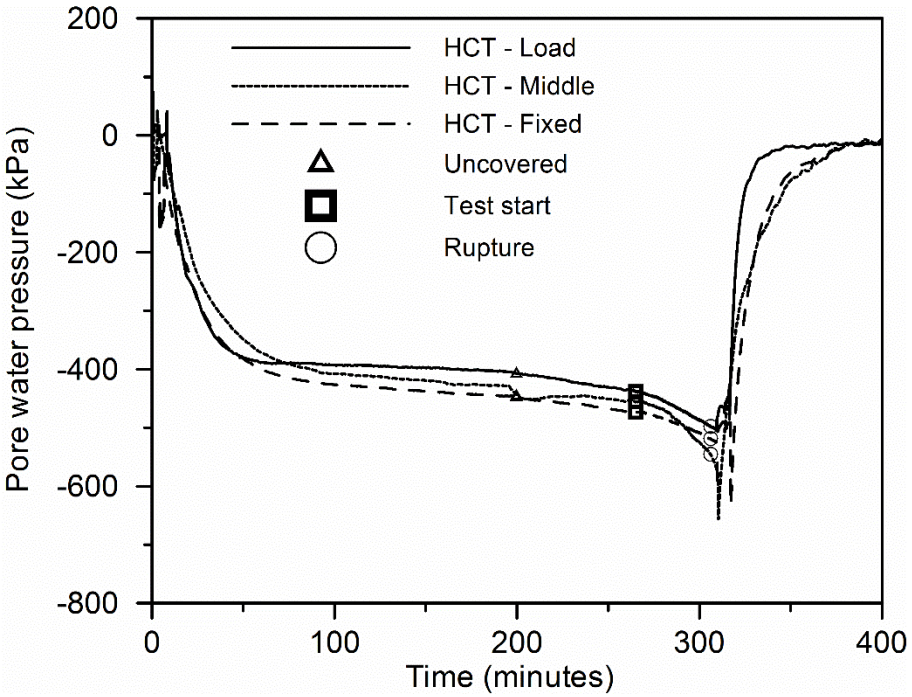

Figure 3-10 Evolution of pore-water pressure measured by the HCTs during the uniaxial tension test on non-de-aired VC (Test 21-10).

The stress paths for the non-de-aired VC uniaxial tension tests in the *p*'-*q* plane are shown in Figure 3-11 together with the critical state line from the triaxial and uniaxial compression tests converted from compression to extension. It has been assumed that the soil is characterised by a unique friction angle, φ', in extension and compression, which leads to two different slopes of the critical state line in the compression, M_c, and extension, M_e, planes respectively. M_e is

calculated using the friction angle from Eq.3-3 from:

$$M_e = \frac{6sin\varphi'}{3 + sin\varphi'} \quad [3.4]$$

It can be observed that only the two specimens with low suctions reach the failure envelope. For all the remaining specimens, the failure data point at rupture lie above the critical state line, i.e. they failed at lower tensile uniaxial stress).

A similar response was observed in the volumetric plane. The two specimens at low suction match reasonably well with the critical state line derived from triaxial compression tests, whereas the other specimens generally appear to lie between the *ncl* and *csl*.

3.6.2 Speswhite kaolin (SK)

Only CU triaxial compression tests could be performed on SK specimens. Uniaxial compression tests were attempted but none were successful due to bending of the specimen upon uniaxial compression. Three samples were tested in triaxial compression having a suction of ~150 kPa after removal from mould. These sample were subjected to a confining effective stress of 59, 252, and 516 kPa respectively. As a result, the sample subjected to the lowest effective confining pressure was slightly over-consolidated whereas the other two were normally consolidated at the onset of shearing.

The stress data points at the critical state were fitted using a linear envelope passing through the origin as shown in Figure 3-12. The corresponding critical state friction angle is φ'_{cs}=23.5°.

Figure 3-12 also shows the critical state data in the volumetric plane together with the normal consolidation line (*ncl*) obtained from samples air-dried to target water content with

suction measured using tensiometers. The critical state data for the specimens tested in triaxial compression are located below the *ncl* as expected.

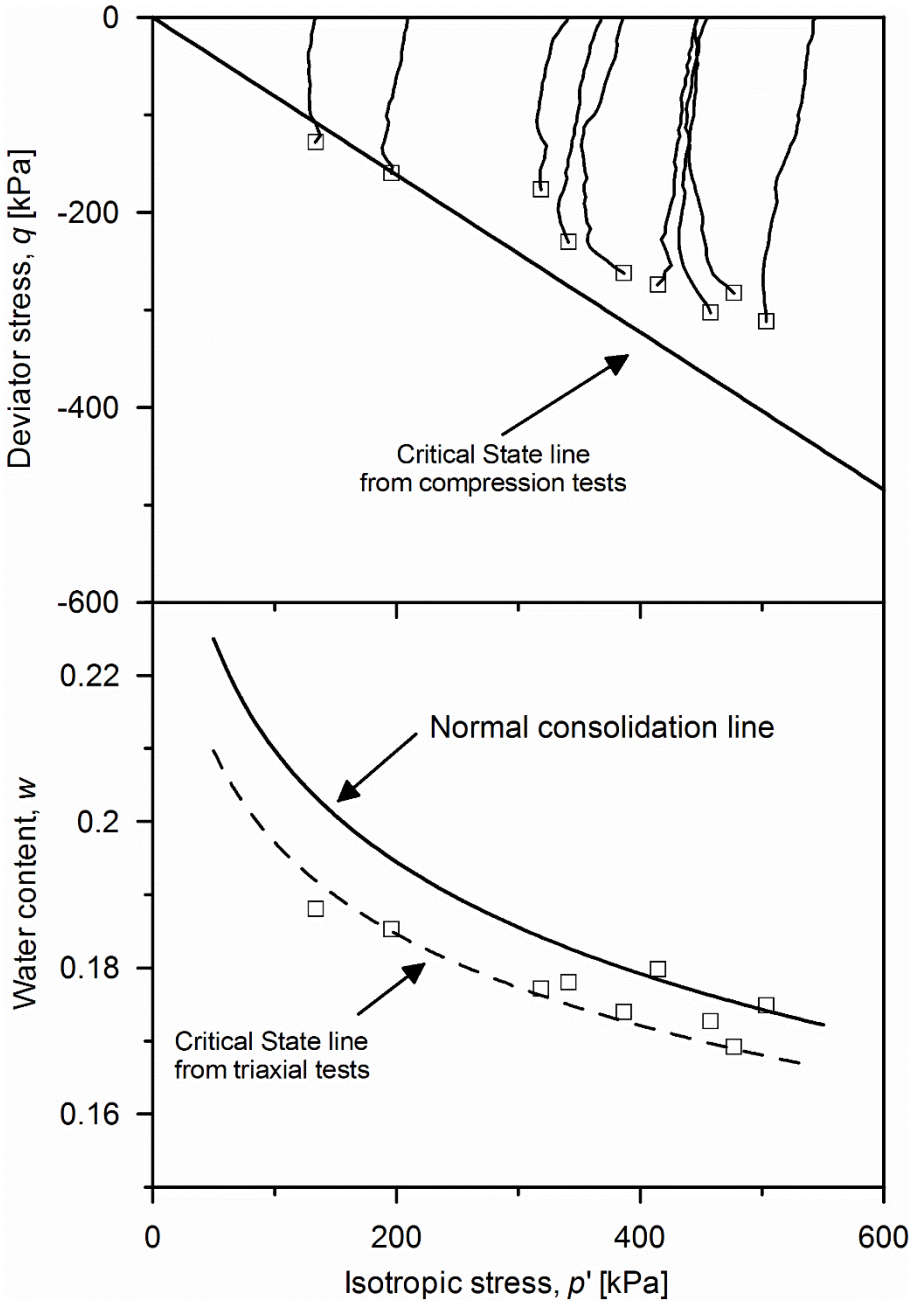

Figure 3-11 Stress-paths and water contents at failure for uniaxial tension tests for non-de-aired VC

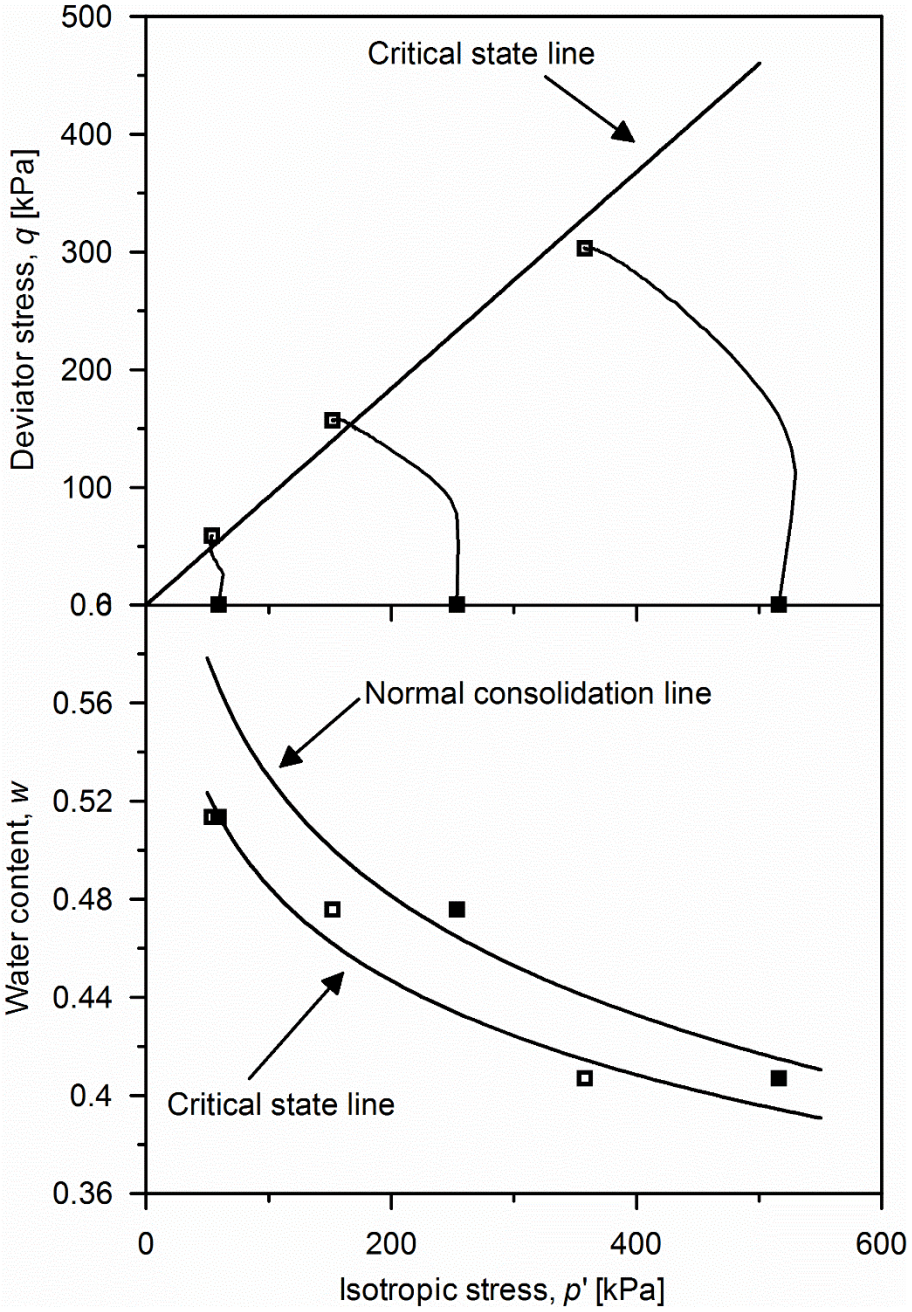

Figure 3-12 Stress-paths and water contents at failure for uniaxial and triaxial compression tests for SK

The stress paths in the *p*'-*q* plane are shown in Figure 3-13 together the critical state line derived from the triaxial compression tests. It can be observed that most of the specimens tested in tension are reaching the same critical state derived from the triaxial compression tests line,

except from the three specimens at high suction (closer to the air-entry suction but still in the saturated range) where the failure data point at rupture lies above the critical state line, i.e. they failed at lower tensile uniaxial stress.

3.7 Failure behaviour of de-aired samples in saturated state

Tensile test data on Vitreous China (VC) and Speswhite Kaolin (SK) have shown that the rupture of the specimens (crack formation) is i) associated with failure in shear and ii) the critical state lines do not appear to be significantly different from the ones inferred from triaxial and uniaxial compression tests. However, it was observed that failure data points depart from the critical state line as suction approaches the air-entry value, i.e. specimens fail at a tensile stress lower than the one predicated by the critical state line inferred from compression tests. Although all specimens were tested in the saturated range, it was speculated that small air cavities could develop in the soil when suction approaches the air-entry value. When the specimen is pulled under undrained conditions, suction increases and some air cavities can trigger cavitation within the pore-water. The loss in suction is in turn associated with a loss in ‘confining’ effective stress and the sample experiences an early failure.

To corroborate this assumption, tests on VC and SK specimens were prepared after de-airing the slurry. This was expected to reduce the amount of air present in the pore-water in the form of tiny undissolved air cavities (cavitation nuclei) and, hence, to reduce the susceptibility of the pore-water to cavitation.

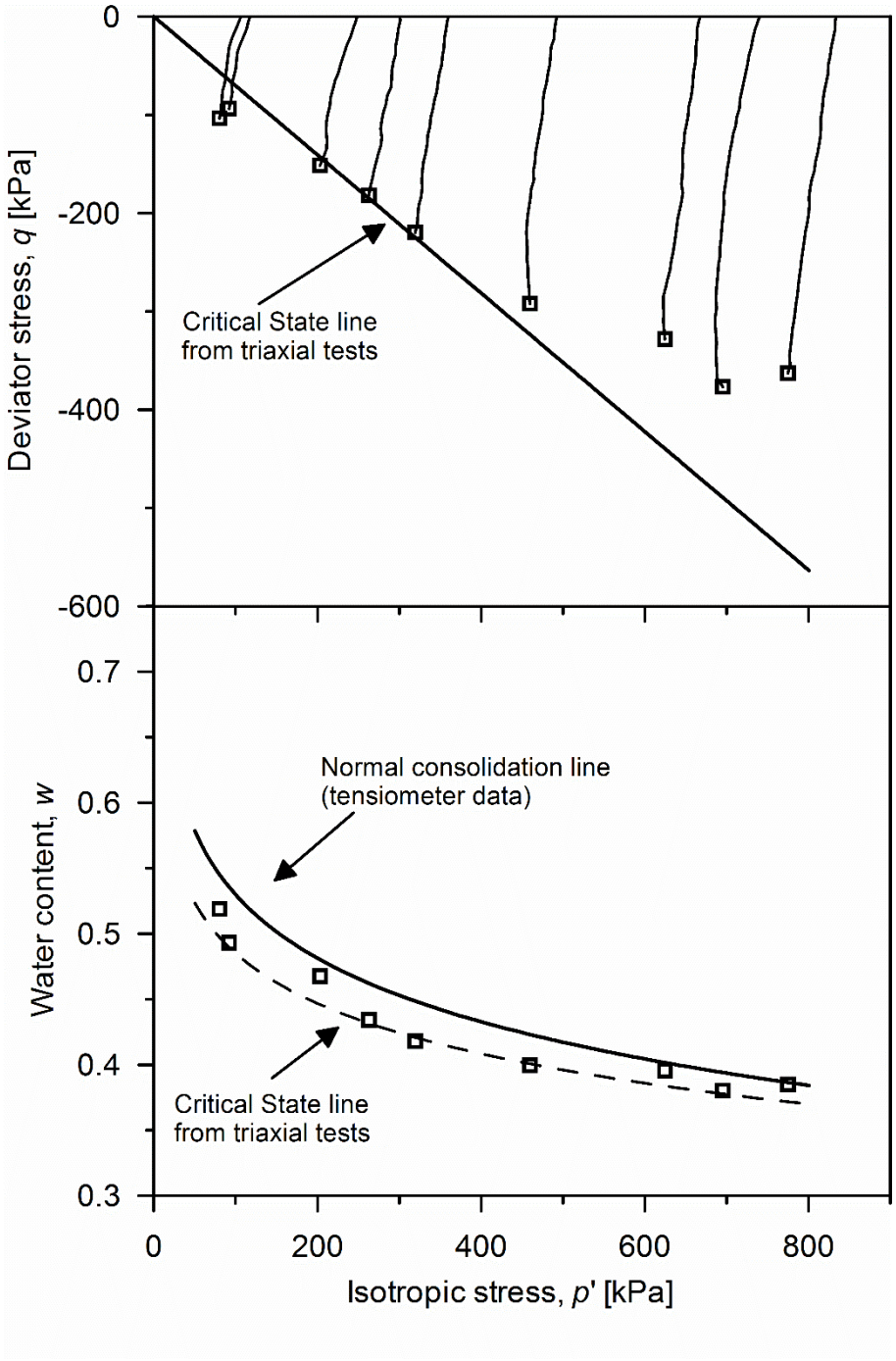

Figure 3-13 Stress-paths and water contents at failure for uniaxial tension tests for non-de-aired SK

The results from tensile tests on de-aired specimens of VC are shown Figure 3-14. The critical state data for the non-de-aired specimens are also shown for comparison. It can be

observed that around 50% of the failure data points for the de-aired specimens in the p’-q plane lie on the critical state line. Similarly, data points for de-aired samples in the p’-w plane are better aligned with the critical state line than non-deaired samples.

The results from tests on de-aired specimens on SK are shown in Figure 3-15. Although the data from de-aired specimens are not falling in the same range of the non-de-aired specimens at high suction that depart from the critical state line, there seems to be similar tendency for de-aired specimens to remain closer to the critical state line than non-de-aired specimens.

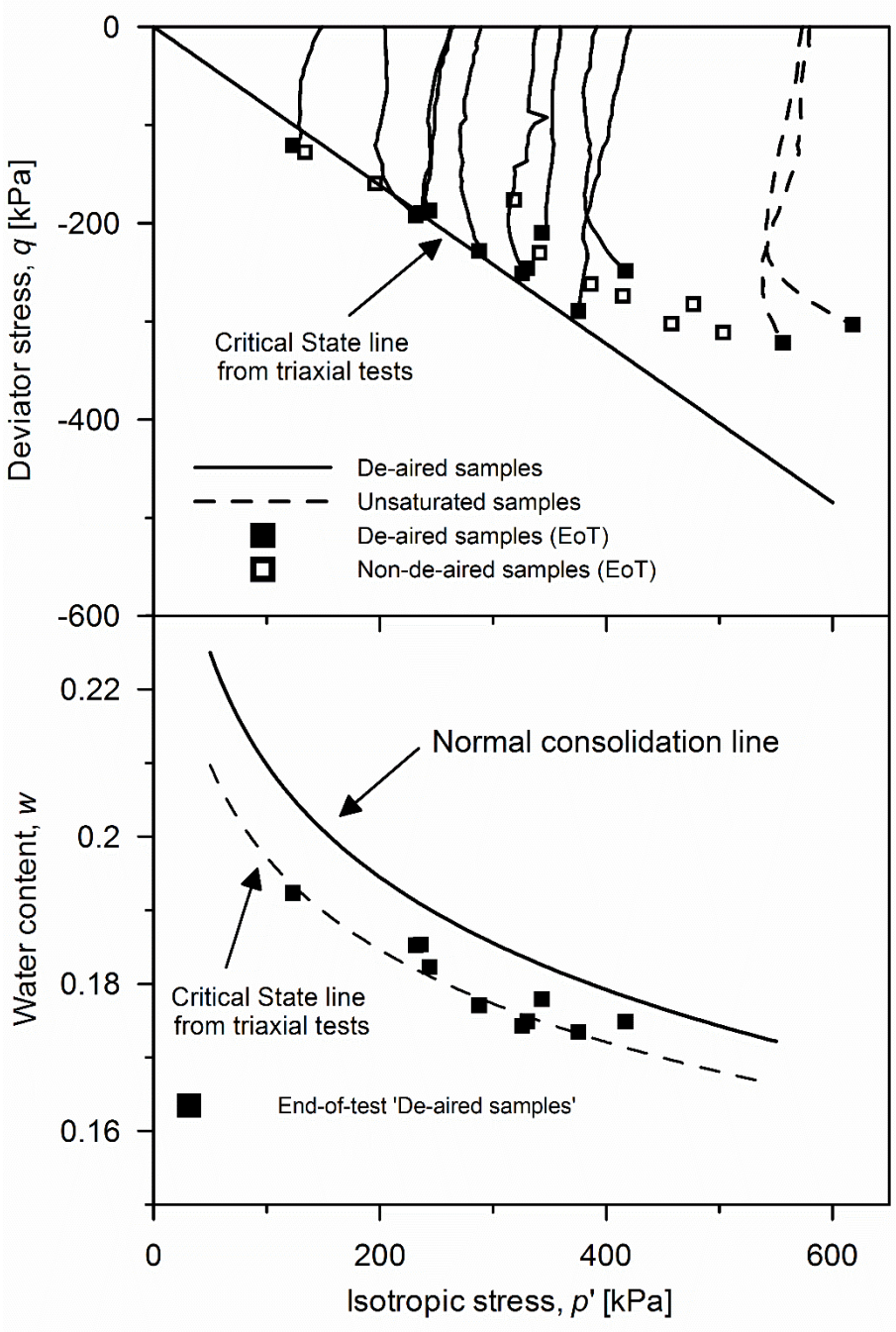

Figure 3-14 Stress-paths and water contents at failure for uniaxial tension tests for -de-aired VC

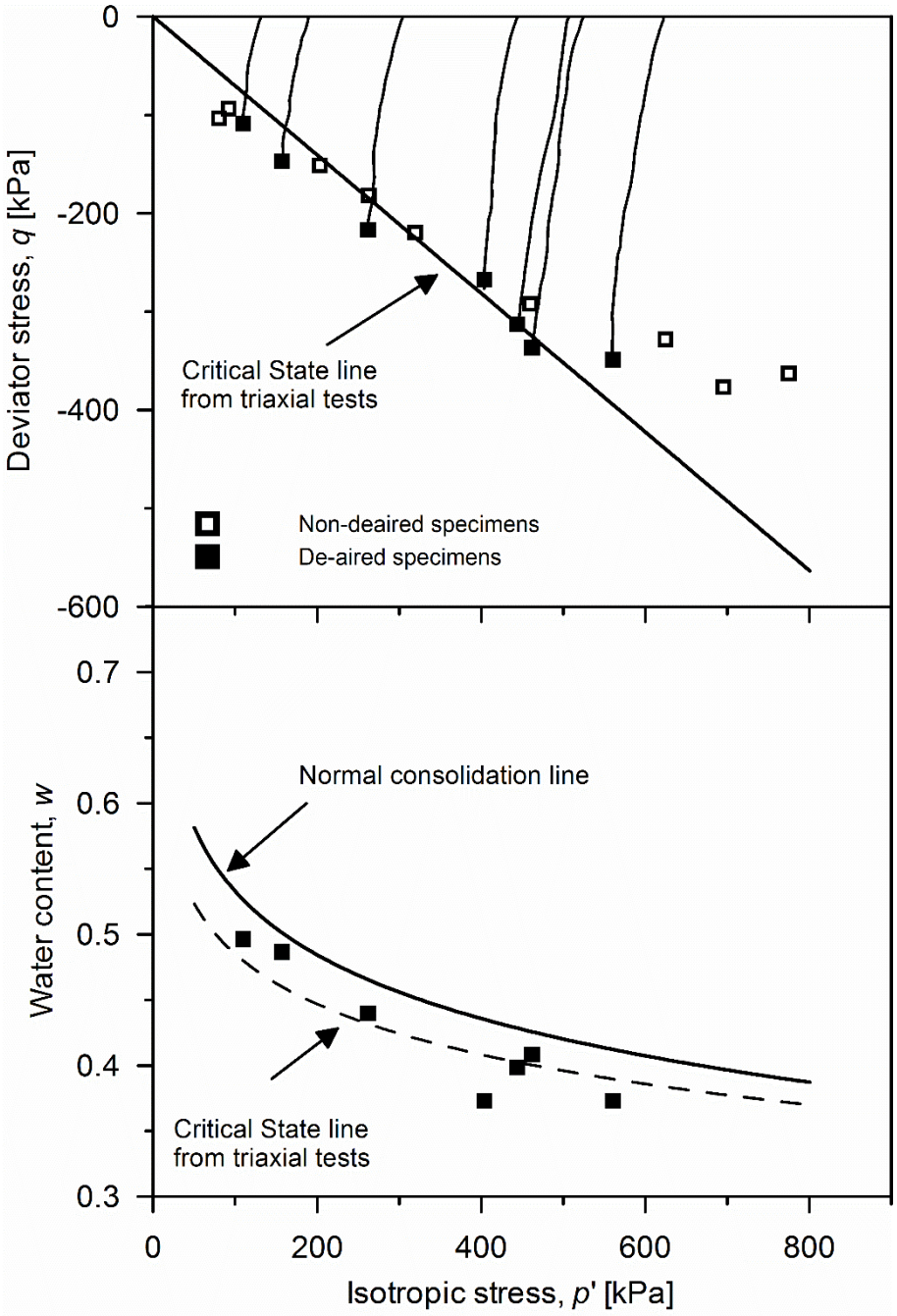

Figure 3-15 Stress-paths and water contents at failure for uniaxial tension tests for -de-aired SK

3.8 Failure behaviour of samples in unsaturated state

Six specimens of VC were tested in the unsaturated range, one prepared from non-de-aired

slurry and the other five prepared from de-aired slurry. The tensile stress data versus suction (at failure) are shown in Figure 3-18 together with the tensile stress data for the saturated specimens prepared from de-aired slurry.

Since tensile test data in the saturated range could be fitted by a traditional Mohr-Coulomb failure criterion, it was tentatively assumed that data in the unsaturated range could also be modelled by extending the Mohr-Coulomb criterion to the unsaturated range.

The criterion proposed by Vanapalli et al. (1996) and validated by Tarantino and El Mountassir (2013) for a wide range of clayey geomaterials was considered here:

$$q = M(p + s \cdot S_r^k) \qquad [3.5]$$

where M is the 'saturated' critical state parameter, p is the isotropic total stress, s is the suction, S_r is the degree of saturation, and k is a scaling parameter for the degree of saturation. This failure criterion requires the parameter k to be derived by the best-fitting of data points in the unsaturated range. To this end, the degree of saturation at failure needs to be estimated for the tensile tests performed in this programme.

Since the void ratio at failure could not be measured, the degree of saturation could not be determined directly, and a different route has been pursued. At the onset of shearing, unsaturated specimens lie on a main-drying surface in the space (s, e, e_w), where s is the suction, e is the void ratio, and e_w is the water ratio. Upon shearing, the void ratio increases at constant water content. The degree of saturation therefore keeps decreasing and moves along a main-drying surface. If an equation is derived for the main drying surface, the degree of saturation at failure can be inferred from the main drying surface and from the measurement of s and e_w at failure.

Tarantino (2009) proposed and validated a model for a water retention surface in the space (s, e, e_w):

$$S_r = \frac{e_w}{e} = \left\{1 + \left[\left(\frac{e}{a}\right)^{\frac{1}{b}} s\right]^n\right\}^{-\frac{b}{n}} \qquad [3.6]$$

where S_r is the degree of saturation, a and b are two parameters derived explicitly from experimental data at very high suction in the plane (s, e_w) and n is an additional parameter to be determined by best fitting. Water retention data for values of high suction in the plane (s, e_w) are plotted in Figure 3-16, where they are interpolated by a straight line in a log-log plot. The parameters of the power function are directly associated with the parameters of the main drying surface (a=16.231, b=0.544). The last parameter was determined by best fitting as shown in Figure 3-17. Two possible values for n are shown in the figure, n=3 and n=4. The overlap between the tensiometer and WP4C data show that the Osmotic suction for the VC material is negligible.

Once the parameters of the main drying surface are determined, the void ratio and, hence, the degree of saturation at failure can be derived from Eq. [3.6] for given values of suction and water ratio at failure. Eq. [3.5] can be therefore be used to predict the deviator stress at failure for specimens tested under unsaturated conditions.

The performance of the shear strength model given by Eq. [3.5] is shown in Figure 3-18 for two values of the water retention parameter n (k=2.2). It can be observed that tension data can be reasonably fitted by a shear strength model, confirming that tensile failure is associated with failure in shear even for unsaturated specimens.

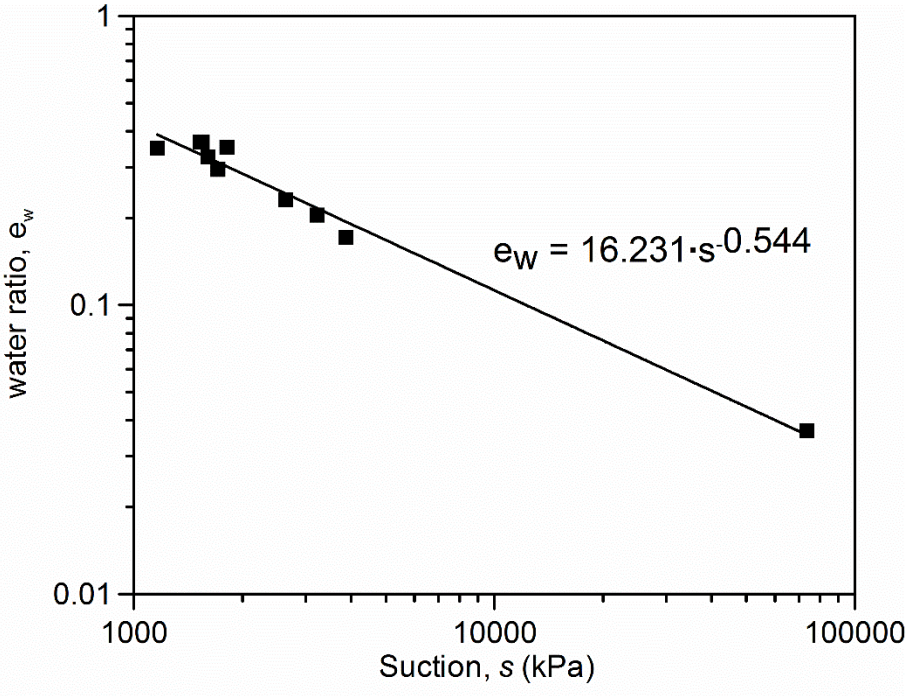

Figure 3-16 Vitreous China water retention drying data at high suction

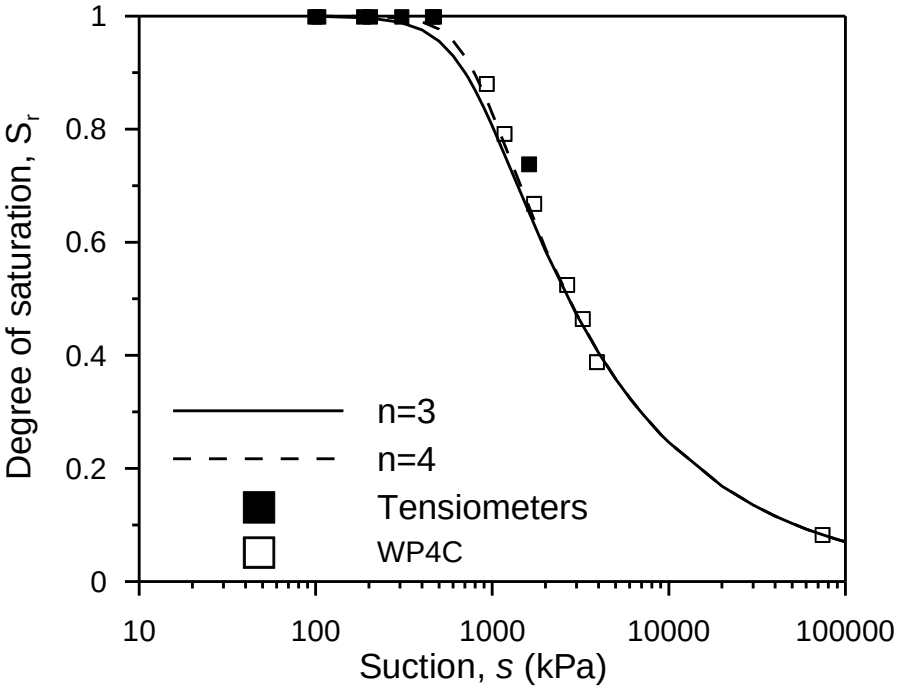

Figure 3-17 Vitreous China water retention drying curve

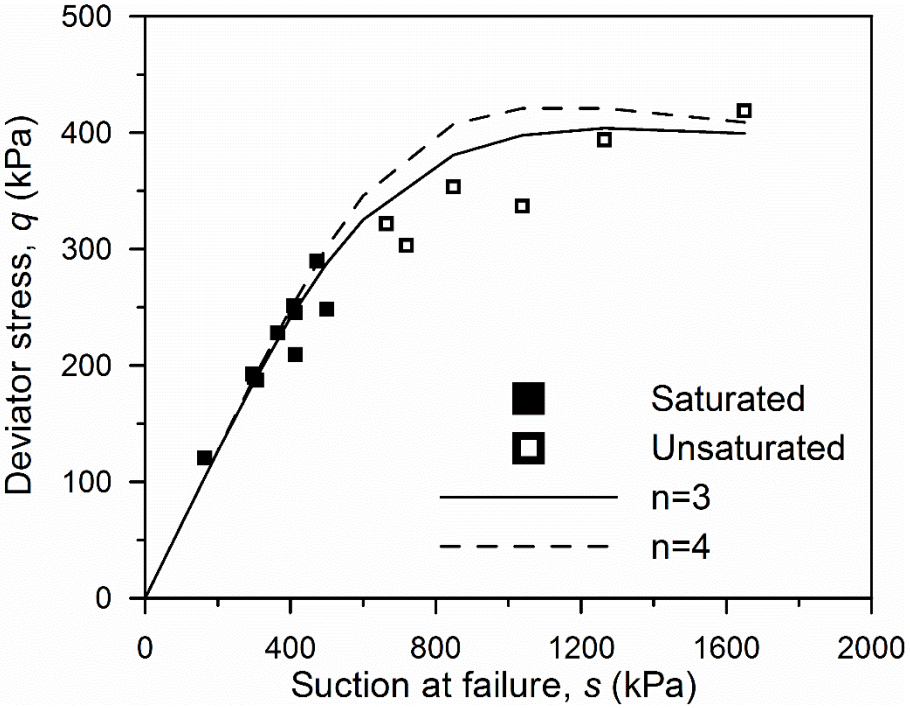

Figure 3-18 Failure data points for saturated (de-aired) and unsaturated specimens and failure envelopes for two different values of the water retention parameter n.

3.9 Discussion

The results from uniaxial tensile tests performed on samples prepared with de-aired water (Figure 3-14 and Figure 3-15) have suggested that cavitation occurring at suction below the air-entry value can trigger early rupture of the specimen.

The possible interplay between the formation of cracks in clay and the process of cavitation has been already suggested by Haigh et al. (2013). In particular, they have assumed that the cracks appearing within the soil thread during the plastic limit test may result from an expansion of cavitation nuclei until the gas occupies the entire cross-section of the thread and the water tension can no longer be transferred through the fluid.

Although Haigh et al. (2013) gave convincing arguments in support of this hypothesis, no direct experimental evidence was provided. Based on the lesson learned from the uniaxial tests

performed in this programme, a difference in the plastic limit would be expected depending on whether de-aired or non-de-aired water is used to prepare the clay thread. In particular, if cavitation is not occurring, a higher suction and, hence, a lower water content could be reached before cracks appears in the clay thread. In other words, preparing the clay with de-aired water should decrease the water content at the apparent plastic limit.

Plastic limit tests were therefore performed on the SK and VC mixes. Two bars of each soil type were cast: one using de-aired slip and the second with normal slip. The plastic limit tests were performed in accordance with BS 1377-2. While performing the plastic limit tests the operator did not know if it was soil that had been de-aired or non-de-aired to prevent any operator bias from affecting the results. Eleven tests were performed on each bar type.

The results of the plastic limit tests are shown in Figure 3-19 for both VC and SK mixes. Data are presented in terms of cumulative distribution, i.e. the probability that the plastic limit is lower than the value read on the horizontal axis. It can be clearly seen that the cumulative distributions shifts to the left (towards lower water contents) for the case where specimens are prepared with de-aired water. The average plastic limit reduced by Δw=0.5 for the VC and Δw=1.7 for the SK.

These results provide further evidence of the role played by cavitation on crack formation and corroborates the mechanism postulated by Haigh et al. (2013).

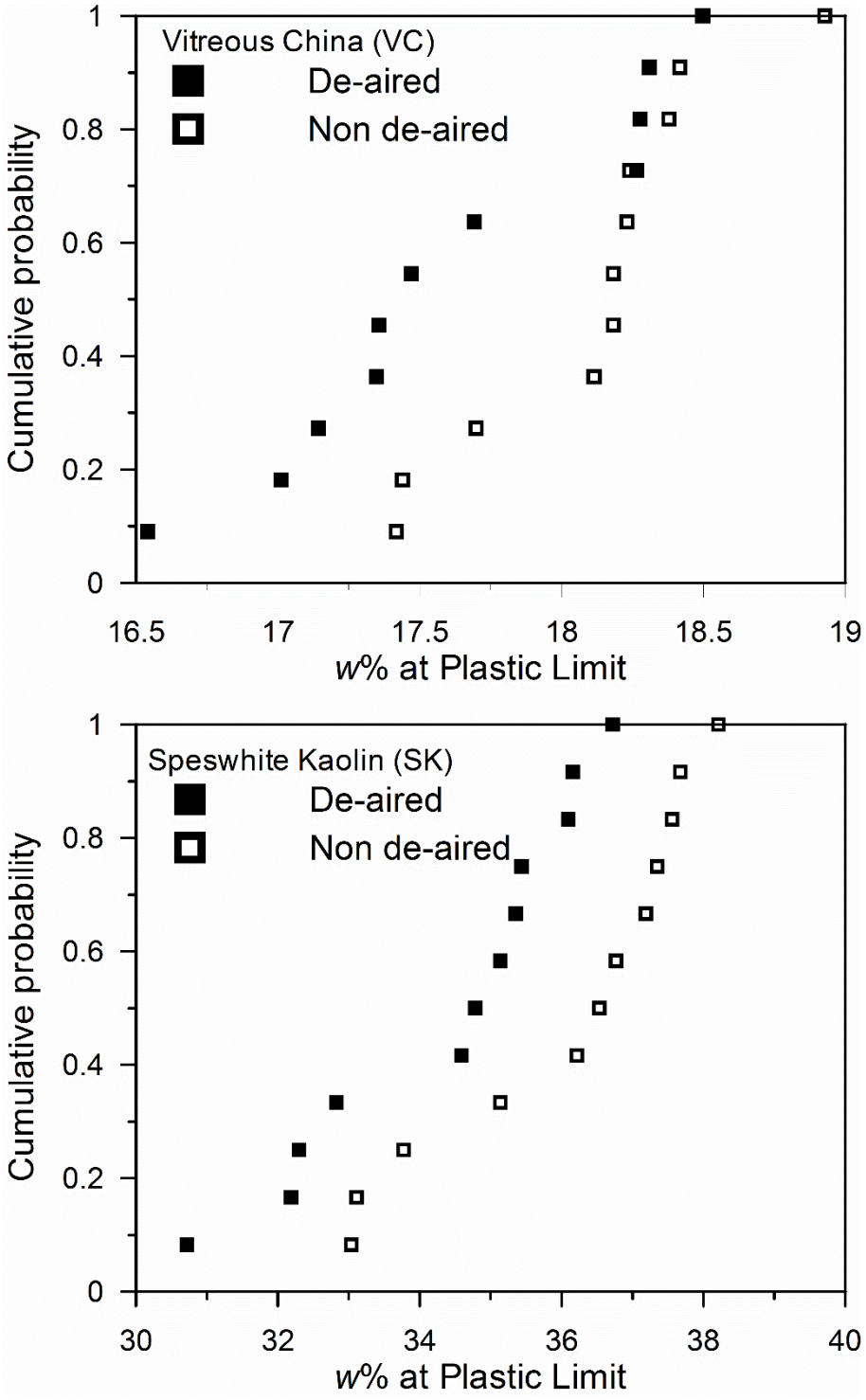

Figure 3-19 Plastic limit tests de-aired and non de-aired specimens of VC and SK

3.10 Conclusions

The paper has presented an experimental investigation of the mechanisms of crack initiation in clayey geomaterial under saturated and unsaturated conditions. To this end, an experimental apparatus was developed to test specimens in uniaxial tension with the facility to monitor suction using high-capacity tensiometers. This allowed interpretation of the data to be done in terms of effective stress for the saturated specimens and in terms of average skeleton stress for the unsaturated specimens.

The first series of test was performed on saturated samples of Vitreous China clay and Speswhite kaolin clay. Samples were reconstituted from slurry (prepared by slip-casting) and prepared using non-de-aired water. When suction approaches the air-entry value, failure occurs at a deviator stress lower than the one corresponding to the critical state line derived from triaxial and uniaxial compression. This behaviour was observed for both of the clays tested.

Although all specimens were tested in the saturated range, it was speculated that small air cavities could develop in the soil when suction approaches the air-entry value. When the specimen is pulled under undrained conditions, suction increases and some air cavities can trigger cavitation within the pore-water. The loss in suction is in turn associated with a loss in ‘confining’ effective stress and the sample experiences an earlier failure.

To corroborate this assumption, a second series of tests were performed on saturated specimens with the slurry preventatively de-aired before slip casting. The de-airing process was aimed at reducing the number of cavitation nuclei the clay and, hence, at reducing the probability of early failure due to water cavitation. Indeed, the de-airing process realigned the deviator stress at failure recorded in the tensile test with the critical state line derived from uniaxial and triaxial compression tests. It was therefore demonstrated that water cavitation is

one of the mechanisms that can control rupture of clay when subjected to a (total) tensile stress state.

Failure data on unsaturated specimens could be fairly modelled by the Mohr-Coulomb criterion extended to unsaturated states (by replacing the effective stress for saturated geomaterials with the average skeleton stress). This has confirmed that tensile failure is associated with failure in shear, even in the unsaturated state.

Finally, the plastic limit was determined for the two clays tested in this experimental programme by preparing the clays with either non-de-aired or de-aired water. The water content at the plastic limit decreases for the case where the pore-space is filled with de-aired water and this corroborates the assumption made in the literature that cavitation influences the cracking that occurs during the plastic limit test.

3.11 Acknowledgements

The authors wish to thank Ideal Standard International for supporting the research and Fernando Francescon from Ideal Standard Italia s.r.l. for his helpful discussions. Additionally, Derek McNee for his help constructing the test apparatus and Arianna Gea Pagano and Elena Prato for their assistance with the triaxial tests.

4 INITIATION OF DESICCATION CRACKING IN CLAY FORMS SUBJECTED TO NON-UNIFORM HYDRAULIC AND MECHANICAL BOUNDARY CONDITIONS

The Lagamine simulations in this chapter were performed by Pierre Gerard of Université libre de Bruxelles.

4.1 Abstract

This paper presents a numerical study using a simple coupled hydro-mechanical Finite Element Method (FEM) model to simulate the desiccation of a clayey soil to the point of crack initiation. The model utilises an effective stress based shear failure criterion, in accordance with recent experimental evidence by the authors (Chapter 3). The results of four laboratory desiccation tests of specimens with non-uniform geometry and different hydraulic boundary conditions are presented. These tests were simulated via FEM, and the time and location of cracking compared to test the validity of the model and the failure criterion. The results show a promising correlation between the time and location of cracking for a majority of the tests, but do not show satisfactory simulation of the forces generated upon the restraints. Further refinement of the model could result in a better match of the forces at the cost of poor prediction of time of cracking.

4.2 Introduction

During drying, the shrinkage of clayey soils can often lead to crack initiation. The development of cracks is of importance to many engineering applications due to the effects these cracks have on the hydraulic and mechanical behaviour of the soil. Clay soils are often chosen, due to their low permeability, to act as barriers e.g. landfill liners/covers and earth dams. The formation of cracks can increase the hydraulic conductivity of clay soils by several orders of magnitude, creating pathways for water flow that can increase erosion rates and pore-water pressure causing leaks and possible structure failure (Marsland & Cooling, 1958; Marsland, 1968; Yessiler et al., 2000; Albrecht & Benson, 2001; Dyer, 2005). Desiccation cracks are also a problem in the ceramics industry (Cooper, 1978) where 5-10% of sanitarware production is lost due to the formation of cracks in wares during air drying (Tarantino et al., 2010).

Various methods have been developed to simulate cracking propagation due to drying-induced shrinkage. These are based upon linear elastic fracture mechanics (Morris, 1992; Konrad and Ayad, 1997; Hallet and Newson, 2001; Lakshmikantha et al., 2012), cohesive crack method (Amarasisri and Kodikara, 2013; Amarasisri et al. 2014,), FEM with mesh fragmentation (Sanchez et al., 2014), and eXtended FEM (Mohammednejad and Khoei, 2012).

However, the mechanism used for crack initiation in all these models is based upon a total stress approach, cracking being initiated when the total tensile stress reaches the materials tensile strength, where the soil tensile strength has been experimentally tested using some form of tensile testing apparatus, e.g. Heibrock et al., 2003; Nahlawi et al., 2004; Stirling et al., 2015. The only notable exception is represented by Shin and Santamarina (2011) where an effective stress approach was used.

Cracking in clays dried from an initial slurry state occurs in the saturated range or at the transition from saturated to unsaturated (Lloret et al., 1998; Costa et al., 2008; Peron et al., 2006; Peron et al., 2009; Tang et al., 2011). In the saturated range the mechanical behaviour should be controlled by the effective stress, σ', and not by the total stress. Models based upon a total stress criterion are not consistent with this principle. Indeed, Thusyanthan et al. (2007) and Chapter 3 show that cracking is associated with a failure in shear and that failure in compression does not differ from failure in tension, i.e. the friction angle parameter ϕ' derived from conventional triaxial compression tests can be enough to characterise the failure condition in cases where there is a negative (total) tensile stress.

This paper presents the results of laboratory desiccation tests on restrained clay soils subjected to different hydraulic boundary conditions. A simple hydro-mechanical approach to model the desiccation and shrinkage of clay forms is presented. Using an 'effective' stress' shear failure criterion, the model is used to predict the location and time of cracking of the laboratory tests in order to validate the shear failure concept.

4.3 Material and sample preparation

The material used for the four tests was a Vitreous China (VC) mix (ball clay, Kaolin, quartz and feldspar). This material mix is commonly used in the ceramic industry. Figure 4-1 shows the particle size distribution for the VC mix.

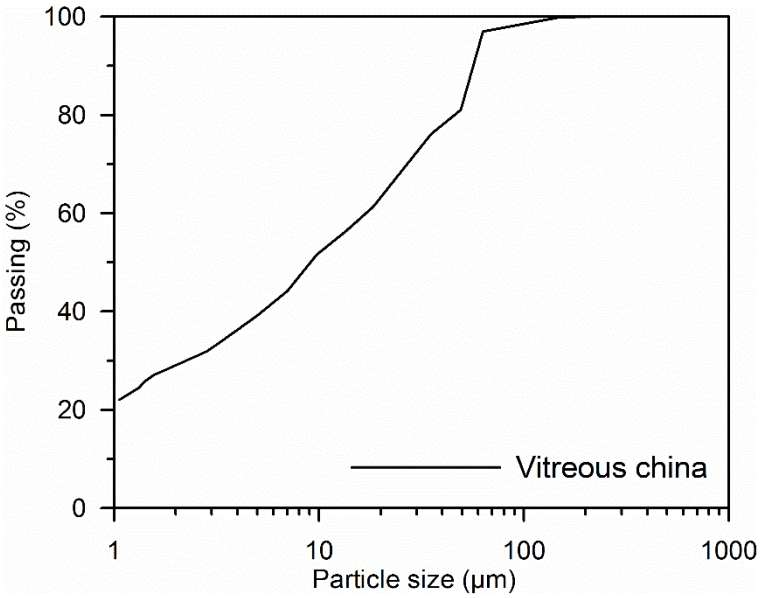

Figure 4-1 Grain size distribution of VC material

The VC slip was obtained by mixing the four different 'ingredients', each component being added to influence the final behaviour of the overall mix, making it suitable for use in the ceramics industry for the production of sanitary ware products. To ensure consistency for each specimen, a large quantity of the VC slip was prepared prior to beginning the experimental programme by mixing the dry powdered constitutive parts with demineralised water to a moisture content of approximately 0.30. The mixed slip was then stored in an air tight container for the period of the experiments. Individual specimens were prepared by taking a portion of the re-mixed slip and adding de-mineralised water to reach the slip density required for successful casting (1.84kg/l for VC, w≈0.35).

Specimens were prepared by slip casting in plaster moulds. Two different moulds were used. The first produced a bar from which individual samples for the material characterisation tests were cut. The second mould produced a specimen of the shape required for the four main evaporation tests. The plaster has a high suction which removes water from the liquid slip to

form a plastic specimen. Plaster moulds were used because they were able to produce the complex shape designed for the evaporation tests.

The slip was added to the plaster mould and left to dry for 90 minutes. Upon removal from the mould the moisture content of the specimens was in the range 0.2-0.21.

Specimens were vacuum sealed and stored for 24 hours prior to testing to obtain an equilibrium in the moisture content throughout the specimen. Where necessary for the material characterisation tests, specimens were air-dried upon removal from the mould to a target moisture content before being vacuum packed.

4.4 Description of Evaporation Test

4.4.1 Specimen shape and test equipment

This study is concerned with simulating the time and location of cracking during desiccation tests. A number of tests using different specimen geometries and restraints were trialled. The commonly used tests, either a long bar (e.g. Peron et al., 2006) or thin cylindrer of soil (e.g. Rodriguez et al., 2007) on a base designed to restrain shrinkage in some way is considered unsuitable as it creates an unknown boundary effect where the degree of restraint is unknown, and/or the stress field generated upon drying makes it obvious where cracks will occur. Tests were trialled using specimens of different shapes and restraint configurations, restraining the specimen using glue, for example Murray et al. (2014). However, it was found that the rigid restraint created by glue caused cracking to always occur at the clay-glue boundary, which meant accurate determination of the time of cracking was difficult and it was considered that such a restraint was too severe. It was found that shrinkage must be prevented by the specimen itself and not by using an adhesive, in order to produce a test with a non-

homogeneous stress field so that the location of cracking was consistent but also identifiable. The final configuration, shown in Figure 4-3, uses a specimen of 1 cm thickness with a “double T” geometry, similar to that of Avila (2013), but using the arms of the specimen to provide the restraint against axial shrinkage, instead of the restraint being a frictional effect between the bottom of the specimen and the base upon which the specimen sits.

The test apparatus has 4 restraints, acting to prevent axial shrinkage at each arm of the double T specimen, with an 85mm by 15mm long section connecting the two end sections, the shrinkage of which causes the generation of stresses. The restraints are made of Teflon to prevent the generation of shear stresses at the contact between the sample and the restraints. Two of the restraints are connected by rods through linear ball bearing blocks to button load cells which measure the force that the sample is applying to the restraint during desiccation. These two restraints are also retractable to allow access for the sample to be easily installed. The specimen sits on a layer of ball bearings which negate any frictional effect between the specimen and the base. The equipment is placed on a balance which measures mass loss throughout the test. A digital camera is used in conjunction with time lapse imaging software to record the location and time of cracking.

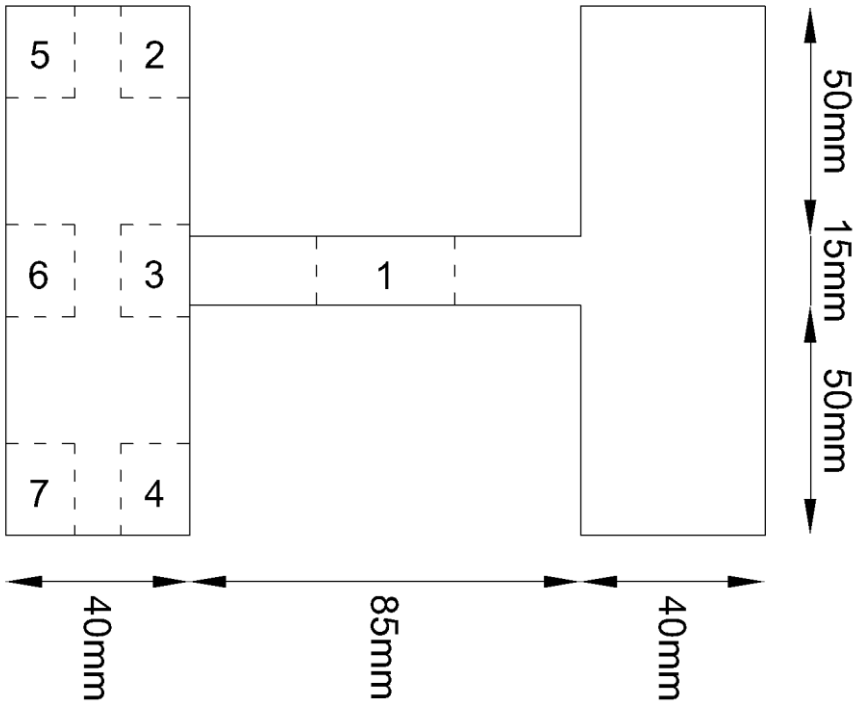

Figure 4-2 Dimensions of test specimen and location of moisture contents taken at end of test

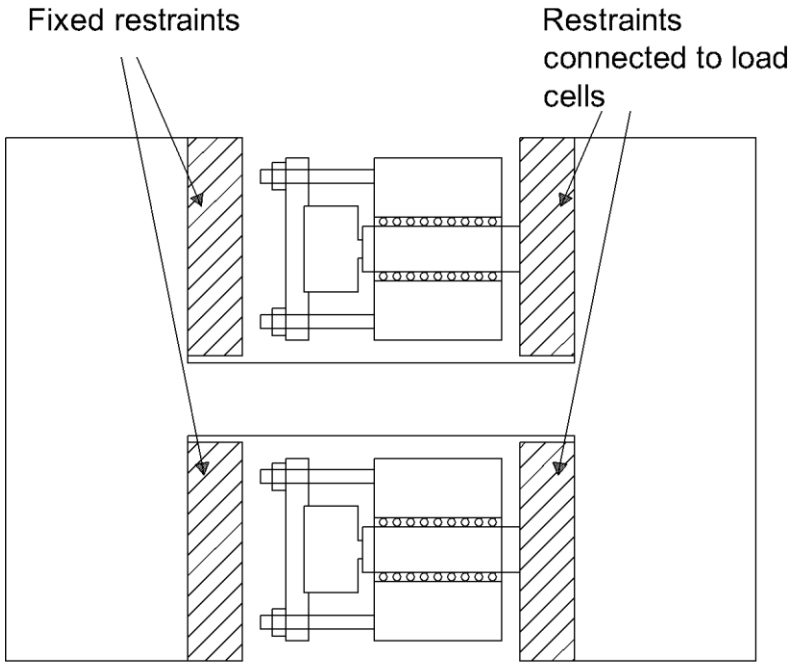

Figure 4-3 Evaporation test restraints and load cells

4.4.2 Experimental Procedure

The mould produced a specimen that was 135mm wide. This allowed 10mm strips to be removed from each of the four arms prior to the start of the experiment to obtain the initial moisture content of the specimen, giving a specimen of the dimensions shown in Figure 4-2. The specimen was then weighed, allowing for a calculation of the weight of solid material in the specimen. The top and bottom surfaces of the specimens were then covered with a known weight of silicone grease to significantly reduce the evaporation from these faces. To adjust the hydraulic boundary conditions of the four tests silicone grease was applied to the lateral faces. The hydraulic boundary conditions of the four tests are shown in Figure 4-4.

The specimen was then placed onto the restraints. The two moveable restraints were tightened until the load cells both recorded a nominal force. The distance between the four restraints was then measured to ensure that the restraints were aligned correctly. The specimen was then left to evaporate, with time-lapse software recording images of the process and the mass loss of water from the specimen recorded by the balance, giving the overall moisture content of the sample throughout the test. After cracking, the specimen was removed, and the moisture content taken from seven sections of the specimen, as shown in Figure 4-2.

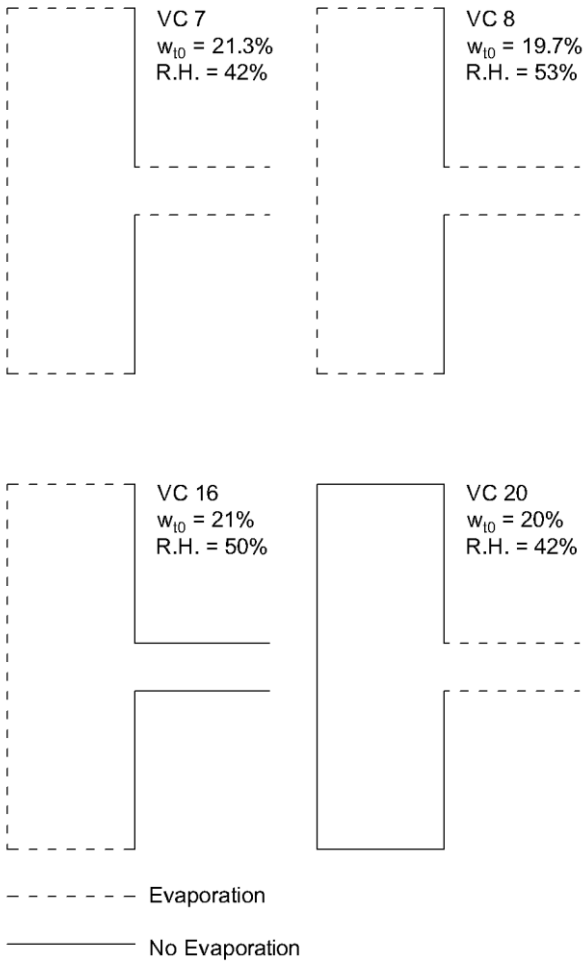

Figure 4-4 Experimental conditions

4.5 Results from evaporation tests

4.5.1 Crack Location

Of the four evaporation tests only VC 20 did not result in a clear crack. VC 7, 8 and 16 all cracked in the same location, at one of the four corners where the centre section transitions to the end sections. Figure 4-5 shows the location of cracking for VC 8. The times of crack initiation are shown in Table 4-3. VC 7 and 8 have the same test conditions, except for the relative humidity of the atmosphere (VC 7 = 42%, VC 8 = 53%). As expected the lower relative humidity of VC 7, and hence higher rate of evaporation, resulted in a crack in VC 7 occurring

earlier than in VC 8.

VC 8 and VC 16 have similar relative humidities, the difference being that the lateral faces of the centre section of VC 16 were covered in silicone grease. This would result in a slower evaporation rate from the centre section and hence the time of cracking is longer for VC 16 than VC 8. These results demonstrate a reliability in the test methods.

The test of VC 20 did not result in a crack where the time of crack initiation could be clearly identified. The test was dismantled when load cell B recorded a drop in force (approximately 600 mins). While dismantling a small crack in the same location from where cracking initiated and propagated in the other three tests was apparent. The time when this crack initiated is unknown from the time-lapse images.

4.5.2 Forces vs Time

The forces measured during the evaporation tests are shown in Figure 4-6. The growth of the force in the VC 7 and VC 8 tests show a similar shape and maximum value (≈8N) at the point of crack initiation, as would be expected due to the similar test conditions. As evaporation is allowed from the lateral faces of the centre section, the restrained axial shrinkage of which is the cause of the force growth recorded by the load cells, the force growth is relatively linear with time. In the case of VC16, where evaporation from the centre section is reduced with silicone grease on the lateral faces, the force grows exponentially with time. The transfer of water from the centre section is mainly as a result of an increase in suction in the end sections, where there is no silicone grease on the lateral faces. Once the suction gradient between the end and centre sections is established, the centre section begins to dry, and the force is generated more rapidly. In contrast to this, the force recorded in VC 20 grows rapidly in the initial phase of the test and then slows as fluid from the end sections moves into the centre section. The force

vs time curve of test VC 20 is concave downward, as opposed to the other tests.

4.5.3 Moisture content at time of cracking

The moisture contents, taken from the seven locations at the time of cracking, or in the case of VC 20, at the point where the test was dismantled, are shown in Table 4-1. The main point of note is the difference in VC 16 and VC 20 for the relative moisture contents between the centre and average end parts. It can be seen that the moisture content in the centre section of VC 16 is slightly higher than that of the ends, as expected with evaporation mainly occurring from the end sections. Whereas, in VC 20 the moisture content in the centre is lower than in the ends. In VC 7 and VC 8, where there is evaporation allowed from all of the lateral faces, the moisture contents are within a small range for all of the areas.

The moisture contents of VC 20 may provide an explanation as to why the small crack observed when the test was stopped did not propagate as was the case for the other 3 tests. The moisture content in the centre section of VC 20 at the time of dismantling was 15.1%, which corresponds to a suction beyond the air entry value for the VC material. It is likely that the small crack occurred around the point of air entry, but did not propagate as there was no further restrained shrinkage in the centre section. This assessment is corroborated by the plateau in force recorded by load cells.

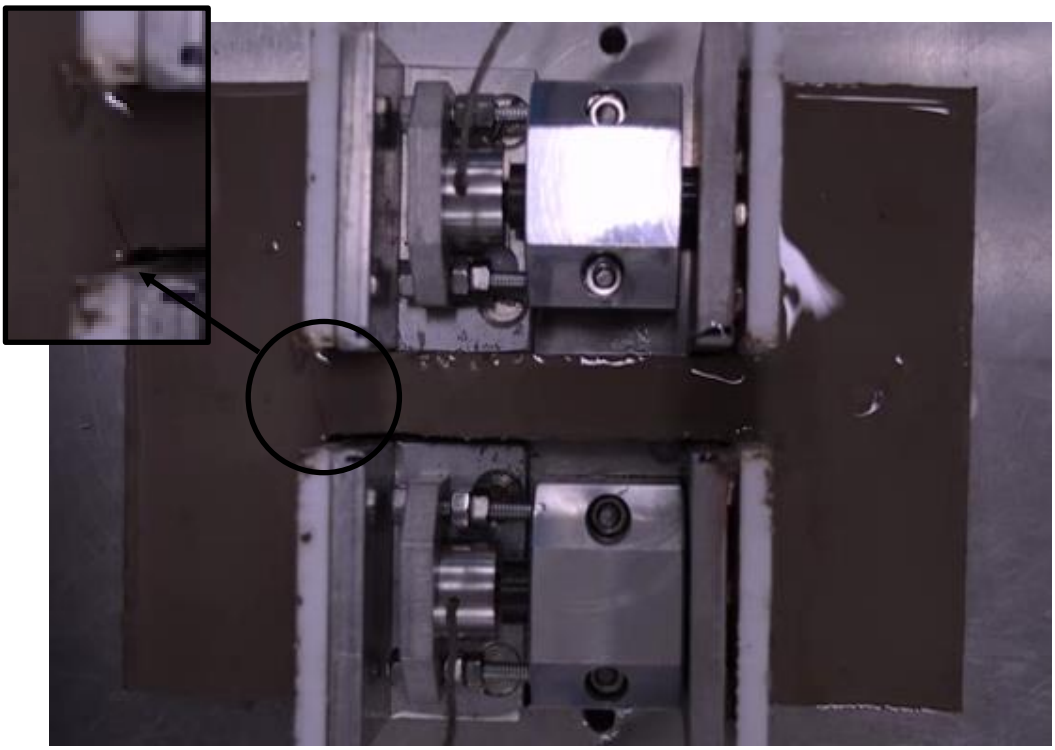

Figure 4-5 Location of crack (VC 8)

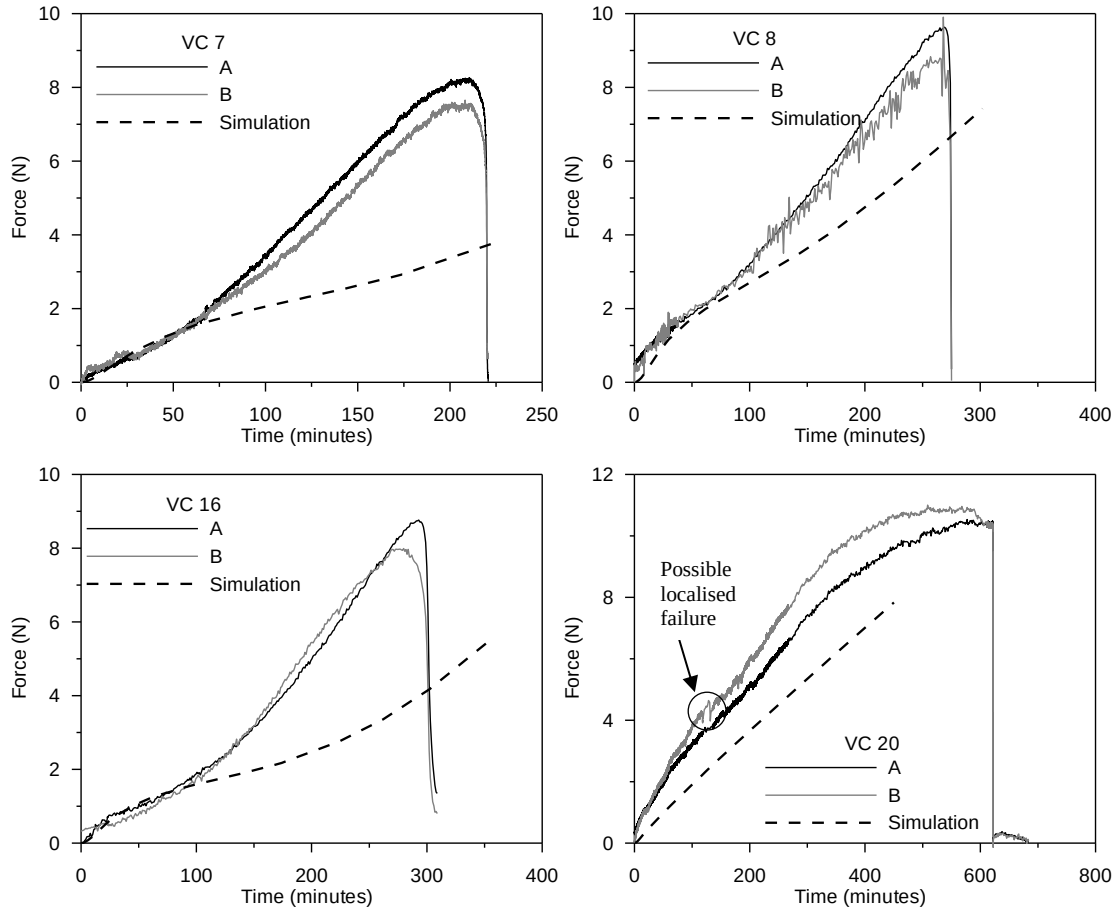

Figure 4-6 Force evolution in evaporation tests

Table 4-1 Water contents at time of cracking/end of test for evaporation tests

	w_{crack} (%)						
Location	1	2	3	4	5	6	7
VC7	17.5	17.8	17.8	17.9	17.3	17.8	17.7
VC8	17.1	16.9	17	16.7	16.7	16.9	17.1
VC16	18.4	18.1	18.4	18.1	-	18.3	18.2
VC20	15.1	17	16.8	16.5	16.5	16.3	16.2

4.6 Numerical model

4.6.1 Geometry

Investigation has shown that evaporation from greased faces is reduced but is not completely prevented. Therefore, due to evaporation occurring from the top face, 3D hydro-mechanical simulations are required to properly reproduce the gradients of pore pressures that developed within the bars and the corresponding shrinkage. The finite element code Lagamine is used (Collin et al., 2002; Gerard et al., 2008) to compare the numerical time and location of cracking with those observed experimentally. The geometry of the model corresponds to the one defined in Figure 4-2, with the sample height equal to 1 cm.

4.6.2 Boundary conditions

For reasons of symmetry only one quarter of the test is modelled. Vertical displacement is prevented at the bottom of the bar, and horizontal displacement is prevented perpendicularly to the restraints, but shrinkage is allowed parallel to the four restraints i.e. axial shrinkage is prevented but radial is allowed. Evaporation is prevented from the base of the sample and from the faces that are in contact with the restraints. The evaporation rate, q is imposed through a convective evaporation condition:

$$q = \alpha\left(\rho_{v,\Gamma} - \rho_{v,air}\right) \quad [4.1]$$

where α is the overall mass transfer coefficient that is independent of the drying conditions (Gerard et al., 2008), $\rho_{v,\Gamma}$ and $\rho_{v,air}$ are the vapour densities at the specimen face and of the surrounding air respectively. The vapour density is derived from the relative humidity via the ideal gas law. The mass transfer coefficient α is fitted using the experimental mass loss of the

test specimen during evaporation. As explained previously, parts of the specimen were covered with silicone grease to reduce evaporation. The respective evaporation ratio through greased and non-greased faces in free conditions was determined under controlled laboratory conditions by comparing the evaporation rates from cylindrical VC samples where evaporation was reduced on all the faces using silicone grease with a second identical cylinder where free evaporation was allowed. From this a ratio of approximately 8.5:1 between non-greased and greased faces is imposed for the mass transfer coefficient. It is also assumed that there is a reduction in the flux rate from the faces of the centre section of the bar due to the close presence of the load cells and restraints, which will reduce the convection of air around the centre faces. The 4 flux rates for the greased and non-greased external faces and greased and non-greased internal faces were determined by best fitting the overall mass loss for the 4 experimental tests, maintaining the 8.5:1 ratio for the external faces. The mass transfer coefficient used, shown in Table 4-2, were maintained for all of the four simulations.

Table 4-2 Mass transfer coefficient, α (m/s) for different specimen locations

	External Faces	Internal Faces
Greased	1×10^{-3}	6×10^{-4}
Non-Greased	8.5×10^{-3}	1.8×10^{-3}

4.6.3 Water retention behaviour

Measurement of suction

The relationship between suction (negative pore-water pressure) and moisture content along a drying path was measured using high-capacity tensiometers (Tarantino & Mongiovì, 2002), which consists of a water reservoir, a high air-entry ceramic disk (1.5 MPa) and a strain-gauged diaphragm. A review of this measurement technique can be found in Tarantino (2004)

and Marinho et al. (2008). The tensiometers used could measure suction pressure up to 2000 kPa, with a measured standard deviation of error of ±1.5 kPa.

Specimens were cut from the cast bars using a 60mm diameter metal cutting ring. The measurement of suction was carried out in a box with the specimen enclosed in the cutting ring. O-rings were used to seal the box and to ensure that the water vapour in the box could reach equilibrium with the specimen water.

Two tensiometers were used simultaneously to measure the suction. The use of two tensiometers made it possible to check the reliability of the measurement by ensuring that the two tenisiometers returned similar values. Once the tensiometers recorded a stable value for the suction of the specimen pore water, the specimen was placed in the oven for 24hrs to obtain the gravimetric moisture content related to the measured suction.

Measurement of suction beyond the range of the tensiometers was performed using a WP4C dewpoint potentiometer. Calibration of the device was achieved by using sodium chloride solutions with known water potentials, with a measured standard deviation in accuracy of ±30 kPa. Further information on the use of the WP4C can be found in Decagon devices (2014).

Small specimens were cut from the dried bars and placed into the device. At the end of the measurement the specimen was placed into an oven to obtain the gravimetric moisture content related to the pore water tension.

Measurement of void ratio

Disc samples were cut from the cast bars dried to target water contents using a small cutting ring, 15.5 mm inner diameter and 12.5 mm high. Excess clay was carefully trimmed from the top and base of the cutter. The volume of the specimen was then derived from the inner

dimensions of the cutting ring. The cut specimen was put in the oven at 105°C for 24 hours to determine the moisture content. The void ratio was then calculated from the measurements of specimen volume and moisture content.

By combination of the relationship between pore-water pressure versus gravimetric moisture content and void ratio versus moisture content, it was possible to derive the water retention curve in terms of degree of saturation shown in Figure 4-7. The soil water retention curve was modelled using the van Genuchten's function (van Genuchten, 1980):

$$S_{re} = \frac{S_r - S_{res}}{1 - S_{res}} = [1 + (\alpha \cdot s)^n]^{-m} \quad [4.2]$$

where S_r is the degree of saturation, S_{res} is the residual degree of saturation, S_{re} is the effective degree of saturation, s is the suction and α = 0.0007, n =2.45 and m = 0.45 are soil parameters derived by best-fitting using the least-square method.

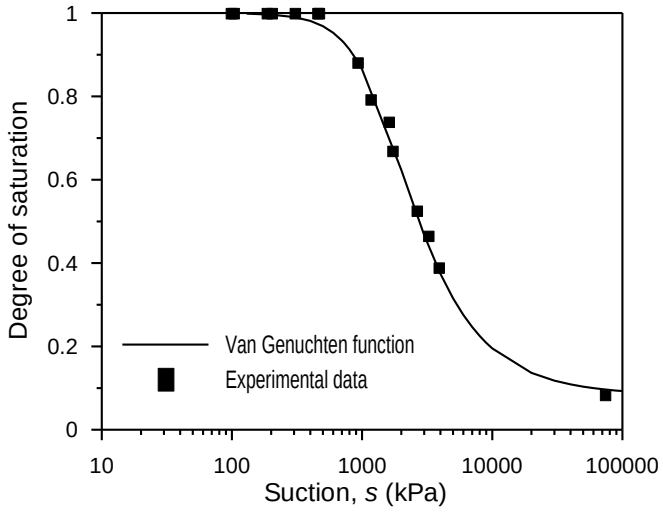

Figure 4-7 Drying curve for VC

4.6.4 Fluid Transfer

The fluid transfers within the clay are reproduced by a two-phase flow model, accounting for water in both liquid and vapour phases. It takes into account the advection of the liquid phase using the generalised Darcy's law and the diffusion of the water vapour through Fick's law.

The hydraulic conductivity K in the unsaturated domain is based on a Kozeny-Karman relationship, and is assumed to depend on void ratio e and the degree of saturation S_r via a hyperbolic relationship:

$$K = K_{sat,ref}\left(\frac{e}{e_{ref}}\right)^3\left(\frac{1+e_{ref}}{1+e}\right)(S_r)^{\beta} \qquad [4.3]$$

where $K_{sat,ref}$ is a reference saturated hydraulic conductivity at reference void ratio e_{ref} and β is a material parameter.

Saturated Hydraulic Conductivity

Values for $K_{sat,ref}$ and e_{ref} were obtained using a constant head hydraulic conductivity test carried out in a modified oedometer cell. A specimen was cut from the cast bar using the oedometer cutting ring. The sample was placed into the oedometer and the cell was covered with water. The specimen was loaded in steps, as with a standard oedometer test, to a vertical pressure of 620 kPa.

The oedometer cell was connected to a reservoir of water and the flow through the cell controlled with a valve. When the valve was opened water was able to flow through the sample. The quantity of water passing though the sample was measured by weighing the water reservoir before and after the tap was opened, accounting for loss of water through evaporation from the reservoir. Darcy's law was used to calculate the hydraulic conductivity, $K_{sat,ref}$ (= $1.94\ 10^{-11}$

m/s) at the reference void ratio, e_{ref} (=0.47)

Unsaturated Hydraulic Conductivity (evaporation test)

The material parameter β is obtained by inverse analysis of an evaporation test. A sample was prepared from a cast bar using the oedometer cutting ring. The lateral surfaces of the sample were covered with silicone grease to prevent evaporation from those faces, evaporation therefore was only possible from the top surface of the sample. The sample was placed on a balance to record the weight of the sample throughout the drying test. The final water content was obtained by placing the sample in the oven at the end of the test; water content of the sample throughout the test was back-calculated using the balance data. To determine the mass transfer coefficient, a beaker of water with the same area open to the atmosphere is placed beside the sample during the test and the weight of water recorded at the start and end of the test. The relative humidity of the air was also measured throughout the test period.

The evaporation test was then simulated to best fit the value of β, by matching the mass loss with respect to time. Figure 4-8 shows the best fitting of the simulated mass loss, using β=3.7.

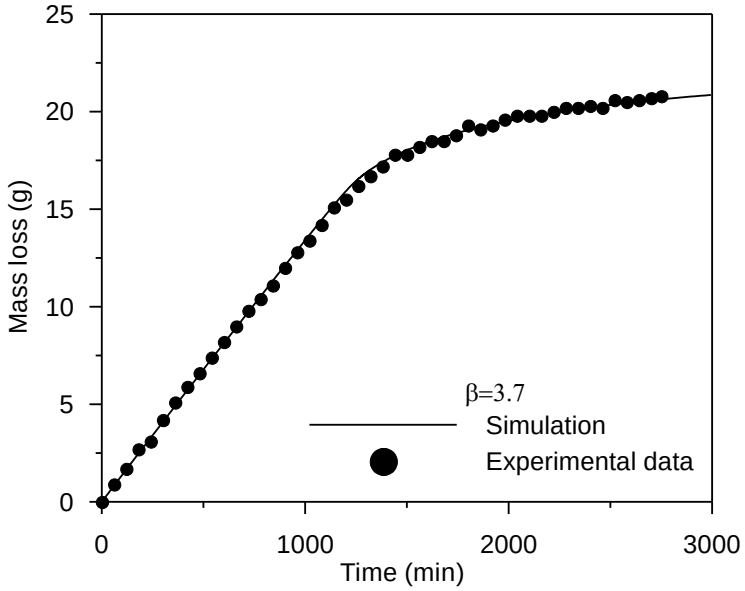

Figure 4-8 Comparison of experimental mass loss and simulated mass loss for unsaturated hydraulic conductivity

4.6.5 Compression behaviour

The slope of the normal consolidation line, λ and the slope of the unloading-reloading line, κ were determined from the results of a standard 1-D oedometer consolidation test on a VC sample taken from a cast bar, Figure 4-9. The assumption was made that the slope of the unloading-reloading line under 1-D conditions coincides with the slope of the unloading-reloading line under isotropic conditions.

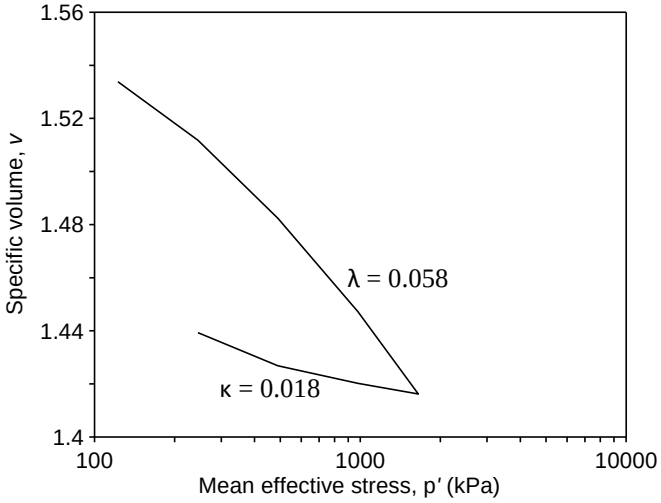

Figure 4-9 Normal compression line and unloading-reloading line for VC

The mechanical constitutive law is written in terms of generalized isotropic effective stress p':

$$p' = p + S_r^{\zeta} s \qquad [4.4]$$

where p is the total stress. In this expression, it has been decided to use a hyperbolic function of the degree of saturation for the expression of the effective stress parameter, as suggested by Alonso et al. (2010), where ζ is a material parameter (ζ=2.2).

Non-linear elasticity, to fit the normally consolidated initial conditions of the specimens, is considered for the Vitreous-China mix as follows:

$$d\varepsilon_v^e = \frac{\lambda}{1+e_0}\frac{dp'}{p'} \qquad [4.5]$$

$$d\varepsilon_d^e = \frac{2(1+v)}{9\kappa(1-2v)}dq \qquad [4.6]$$

where ε_v^e and ε_d^e are the volumetric and deviatoric elastic strain respectively, q the deviatoric stress, p' the mean effective stress, k is the bulk modulus and ν is the Poisson ratio (assumed equal to 0.3).

4.6.6 Shear strength behaviour

The failure criterion was determined using a direct tensile test covering specimens in both saturated and unsaturated states, with pore water pressure being monitored using high capacity tensiometers. It was shown that saturated specimens failed at stress states corresponding to a critical state line derived from the materials friction angle, ϕ', of 27.8° taken from uniaxial and triaxial compression tests. Failure data on unsaturated specimens could also be reasonably modelled by the Mohr-Coulomb criterion extended to unsaturated states (by replacing the effective stress for saturated geomaterials with the average skeleton stress). Full details of these tests can be found in Chapter 3. The full failure envelope is given by:

$$\tau = \left(\sigma + s \cdot S_r^{\zeta}\right) \cdot tan\varphi' \qquad [4.7]$$

where τ is the shear strength, σ is the total normal stress, s is the suction, S_r is the degree of saturation.

4.7 Results

4.7.1 Location of cracking

All of the simulations resulted in the initiation of a crack at the corner between the middle and end sections, which matched well with the location of cracking in the laboratory tests.

4.7.2 Time of Cracking

Figure 4-10 shows the simulated evolution of q/p' in the location of cracking for the four laboratory evaporation tests. The simulated failure for the four tests all occur while the corner of the specimen is still saturated. The figures also show the values of M in triaxial extension (M_e=0.8) and triaxial compression (M_c=1.1) associated with the material friction angle of 27.8°. It is assumed that the critical value of M for a 3-D (true triaxial) stress state is between M_e and M_c. The tests were done assuming that failure occurred with M equal to M_c.

A comparison between the simulated time of cracking and the laboratory results is shown in Table 4-3. The simulated times for VC 7, 8 and 16 correspond very well with the experiments. In all three cases experimental cracking occurs between the crack time simulated for failure in extension and compression.

The simulated crack time of VC 20 is 105 or 135 minutes for failure in extension and compression respectively. The macro crack time of the VC 20 laboratory test is taken as being approximately 600 minutes. The difference between the simulation and test are clearly substantial. A possible explanation for this difference is discussed later.

4.7.3 Force vs Time

The results of the simulated forces with respect to time are shown in Figure 4-6. It is clear that the forces generated on the restraint in the simulations are lower than for the corresponding laboratory test. The reason why the simulated force at the restraint does not replicate the experimental force is still under investigation. One possible explanation is explored later in the paper.

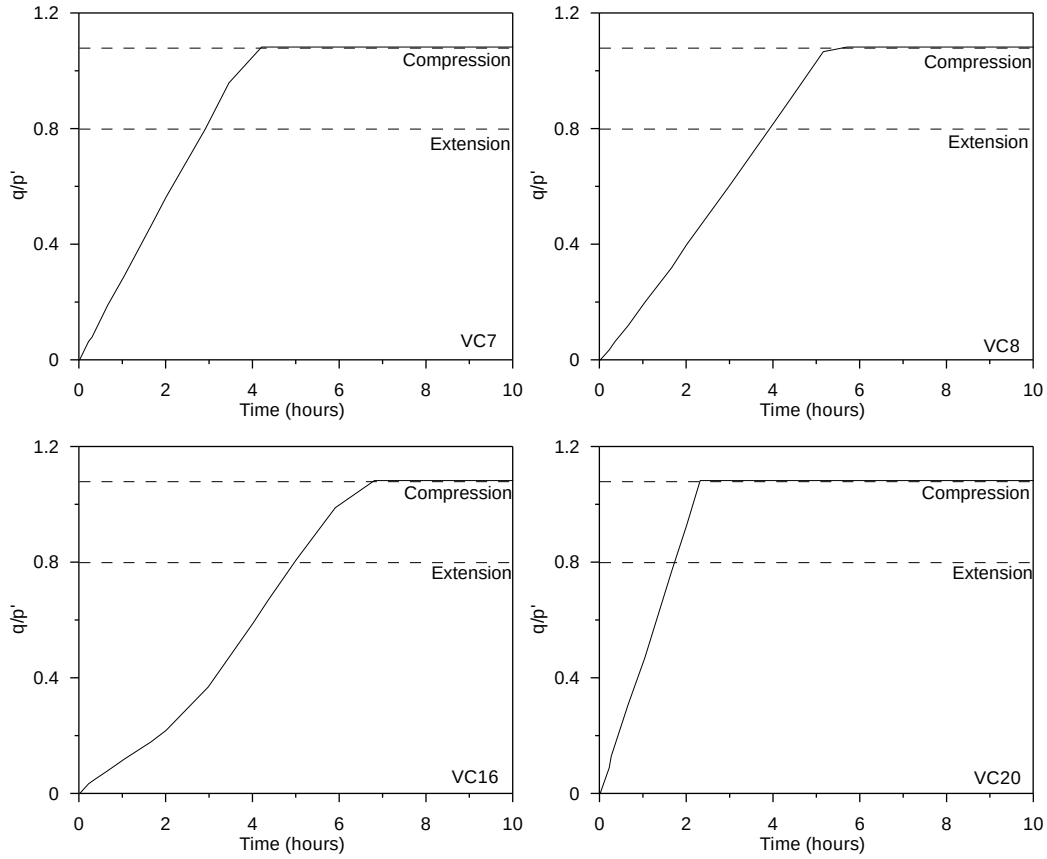

Figure 4-10 Evolution of simulated stress state in location of crack initiation

Table 4-3 Cracking times for laboratory and modelling evaporation tests (minutes)

	VC 7	**VC 8**	**VC 16**	**VC 20**
Simulation (extension)	170	240	300	105
Simulation (compression)	250	330	400	135
Experimental	222	275	302	-

4.8 Discussion

The simulated crack times for the VC 7, 8 and 16 reproduce the experimental results well. However, VC 20 suggests that there is an unknown error in the simulation. The time of cracking

in the model is taken as the point when any location in the specimen has a q/p' ratio that reaches the shear strength. It is speculated that in this test the simulated failure is local to the corner and that in the laboratory test there is a redistribution of stress which prevents any failure from propagating into a macro crack. From Figure 4-6, at approximately 100 minutes, there is an unexplained variance in the force recorded by load cell B. It is speculated that this may be caused by a local failure, as predicted by the model. This hypothesis is somewhat corroborated by the overall force trends with time for the 4 tests. For the VC7, 8 and 16 tests the force grows exponentially with time, meaning any local failure is more likely to propagate into a macro crack that is visible on the time lapse video, whereas for VC 20 the force tends to level off.

The simulation of the force upon the restraints generally resulted in a force that was approximately half that of the experimental test force. In order to understand the influence of Poisson's ratio on the simulated force evolution, the simulations were repeated using a Poisson's value of 0.2. The results of these simulations are shown in Figure 4-11 and Figure 4-12. It can be seen that the change in Poisson's ratio has produced a better replication for the force vs time, particularly for VC 8 and 20, while improving the results of the other 2 tests. However, as shown in Figure 4-12, this change has resulted in the simulated crack time decreasing, so that there is no longer a good agreement with the experimental crack times.

If it is assumed that the Poisson's ratio of 0.2 is closer to the real value for the specimens, then a justification for the poor replication of the crack time should be discussed. In the model the transition corner from the centre section to the end sections is considered to be a 90-degree corner. Such a simulation causes a severe concentration of stresses on the node at the corner. For the experimental specimen it is not possible to have such a severe transition and it is likely that this corner will be slightly smoothed. Incorporating this small change to the geometry of the simulation should reduce the stress concentration, thus delaying the simulated crack time,

but not affecting the simulated force upon the restraint. These simulations are the next piece of work to be done.

Another aspect of the model that has yet to be compared to the experimental results is the water contents in the different locations of the specimen at the time of cracking. If these water contents do not match well with the experimental results it may give indications of errors in the hydraulic aspects of the model, i.e. the values of the fluxes from the different locations of the specimen.

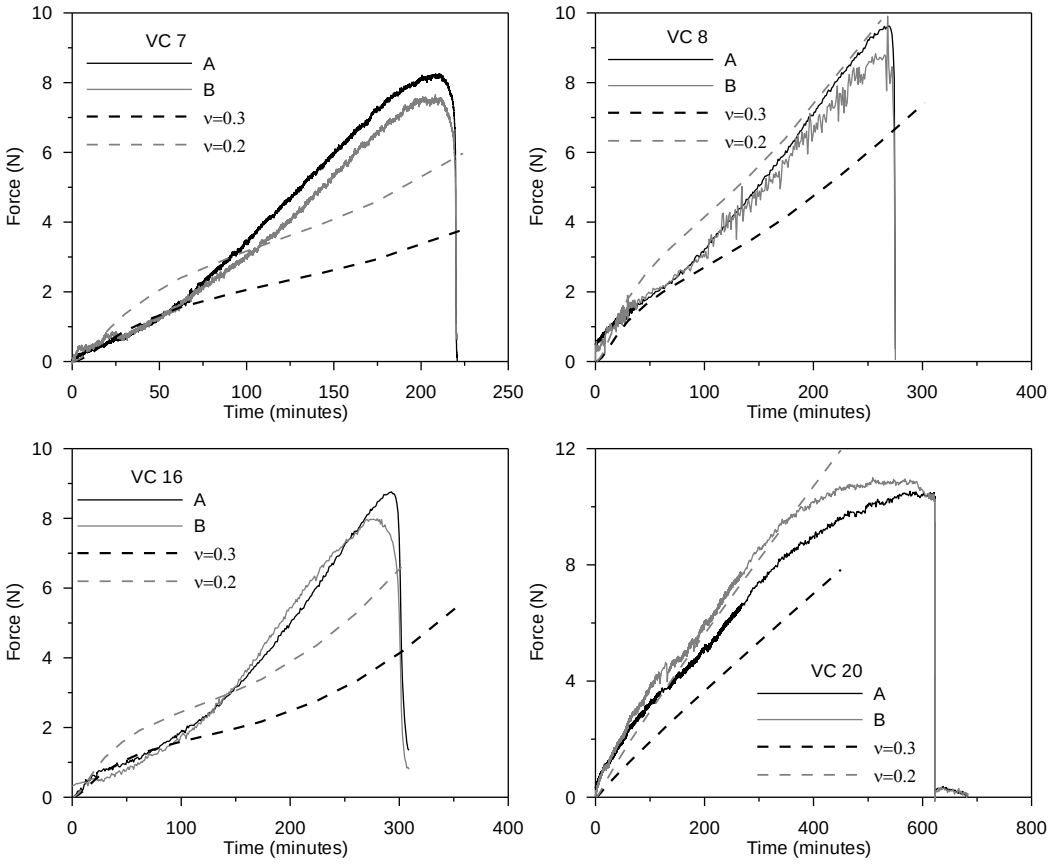

Figure 4-11 Simulation of forces using v=0.2

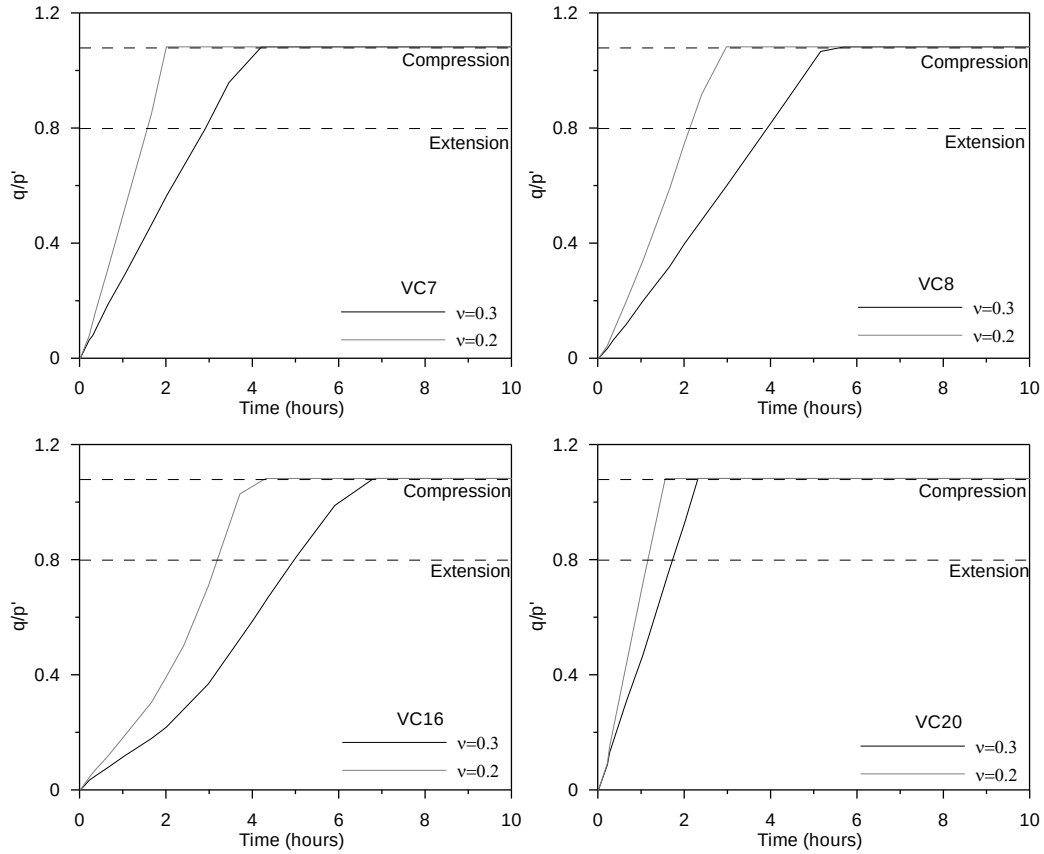

Figure 4-12 Simulation of stress evolution with time using ν=0.2

4.9 Summary

A simple 3D coupled hydro-mechanical Finite Element Method model has been presented and used to simulate the drying, to the point of crack initiation, of laboratory evaporation tests on restrained specimens with different hydraulic boundary conditions. The model uses an effective shear failure mechanism to predict the time and location of cracking.

The results of the simulations show some promising results. Prediction of the cracking location was achieved, in addition to a good correlation of the experimental cracking times for three of the four evaporation tests. However, the model was not able to accurately simulate the forces generated on the restraints. To overcome this, new simulations using a different value

for Poisson’s ratio were performed. The results of these simulations gave a better match for the experimental force. However, this change resulted in a poor match for the time of cracking.

Proposals are made for the next set of simulations where the geometry at the location of cracking will be modified slightly to better represent the laboratory test. It is hoped that this will result in a better simulation of cracking time, while not affecting the location of cracking and simulated forces on the restraints.

5 AN INVESTIGATION INTO THE INTERPLAY BETWEEN GRAIN- AND PORE-SIZE DISTRIBUTION AND SUSCEPTIBILITY TO CRACKING OF CLAYS IN GREENWARE STATE

5.1 Abstract

Measures undertaken to reduce susceptibility to cracking of greenware during drying often include modifying the composition of the casting slip. This is generally achieved by trial and error due to a general lack of understanding of cracking mechanisms. This paper presents a comparison of two casting slips, Vitreous China and Fine Fire Clay, selected because of their different susceptibility to cracking. It is shown that the material with lower cracking susceptibility has a more well graded grain and pore-size distribution and a more gradual transition from the saturated to the constant volume branch of the Bigot curve. To validate the role played by this transition, a hydro-mechanical coupled FEM analysis was also carried out for a disc subjected to non-uniform drying. The lesson learnt from this work is that susceptibility to cracking can be minimised by acting on the gradation of the composition of the grain size distribution.

5.2 Introduction

The removal of water from greenware during the early drying of the manufacturing process is one of the most perplexing problems of the ceramic industry. Practical observations indicate that many of the defects and cracks that appear during the firing of clay objects are caused by poor air-drying conditions prior to firing. The losses due to air-drying defects alone can be in the order of 5-10% of sanitaryware production.

It is widely recognised that cracking tends to be promoted by i) high evaporation rates (Bowman, 1926; Ford, 1986; Scherer, 1990; Clausen & Fish, 1994; Zhu & Leak, 2017) and ii) uneven drying from greenware surfaces (Sokolov & Gak, 1959; Fraser, 1986; Reed, 1988; Gur’yanov & Zakharov, 2007). In both cases, high spatial gradients of pore-water tension are generated within the green form by surface drying. In turn, these generate shear strains and, hence, shear stresses within the greenware, eventually leading to cracking when the shear strength is exceeded.

The susceptibility to cracking of greenware during drying can be reduced, in principle, by slowing down the evaporation rate and/or ensuring uniform drying from all faces. However, these ‘remedial’ measures are impractical in the industrial manufacturing process. Slowing down the drying process requires more space to maintain the same output. For example, reducing the evaporation rate by half means doubling the drying space, which may require a significant amount of additional space. An even evaporation from the different drying surfaces may be difficult to achieve in an industrial environment, especially for the case of hollow greenware. The inner surfaces will inevitably suffer from slower evaporation rates than the outer surfaces. In other words, the qualitative understanding of the mechanisms leading to cracking offers no simple solutions.

The only feasible countermeasure consists of modifying the slip mixture used for casting, by acting on the nature of the ingredients and/or their mass fraction. This is what ceramic manufacturers pursue by a process of trial and error. However, there is lack of understanding of how particle size distribution affects the mechanisms of drying and cracking. This makes it difficult to design new slip mixtures effectively.

This paper addresses the problem of the interplay between particle size distribution and the mechanisms of cracking in green forms subjected to drying, with the aim of guiding mix design. To the best of writers' knowledge, there are no contributions in the literature addressing this aspect.

To this end, two materials were selected in this experimental programme, Vitreous China (VC) and Fine Fire Clay (FFC). These materials have been selected because of their differing susceptibility to cracking.

The response of the two materials upon drying was investigated by monitoring the volume change and the water content against the increase in pore-water tension generated by the surface drying. To gain an insight into the evolution of the clay microstructure upon the drying process, Mercury Intrusion Porosimeter (MIP) tests were carried out on samples at different stages along the drying curve. It was expected that features controlling the susceptibility to cracking could be understood by comparative inspection of the Pore-Size Distribution (PSD) and drying curves of the two different materials. In turn, this would lead to possible cracking remedial measures in terms of slip mixture design.

The effectiveness of the remedial measures proposed in this paper were investigated via numerical analyses of the hydro-mechanical response of a simple green form subjected to drying. The numerical model was firstly validated against its capability to reproduce qualitatively the known effect of evaporation rate on crack initiation. The same model was then

used to ‘test’ the effect of the proposed remedial measures.

5.3 Material and methods

5.3.1 Material and sample preparation

Two material mixes, commonly used in the ceramics industry, were used in the experiments: Vitreous China (VC) and Fine Fireclay (FFC). Their grain size distributions are shown in Figure 5-1.

Specimens were prepared by slip casting in cuboidal plaster moulds (200 mm long, 100 mm wide and 15 mm high). The high suction possessed by the plaster removes water from the liquid slip to create a plastic specimen. Plaster moulds were used because it allowed specimens to be created in a short time and is the same process as used in the ceramic industry.

The VC and FFC slips were obtained by mixing different ‘ingredients’, each component included to influence the behaviour of the overall mix and make it suitable to produce sanitaryware products. To ensure consistent specimens, a large quantity of the VC and FFC slips were prepared prior to beginning the experimental programme by mixing the dry powdered constitutive parts with demineralised water to moisture content of approximately 0.30 for VC and 0.25 for FFC. The slip was stored in an air tight container for the duration of the experiments. Individual specimens of VC and FFC were prepared by taking a portion of the slip, which had been mixed for 30 minutes prior, and adding de-mineralised water to take the slip portion to the required casting density (1.84kg/l, w≈0.35 for VC, and 1.94kg/l, w≈0.29 for FFC).

Slip was added to the plaster mould. The time required to consolidate the slips of VC and FFC to a moisture content of 0.2-0.21 and 0.18-0.19 respectively in the mould was approximately 90 minutes.

Once removed from the mould the bars were air dried to different target moisture content for the required test. Once the target water content was attained, each bar was sealed and stored for 24 hours prior to testing to obtain equilibrium in the moisture content throughout the bar. From each bar, individual specimens were taken for specific tests (i.e. pore-water tension, void ratio, and pore-size distribution measurements).

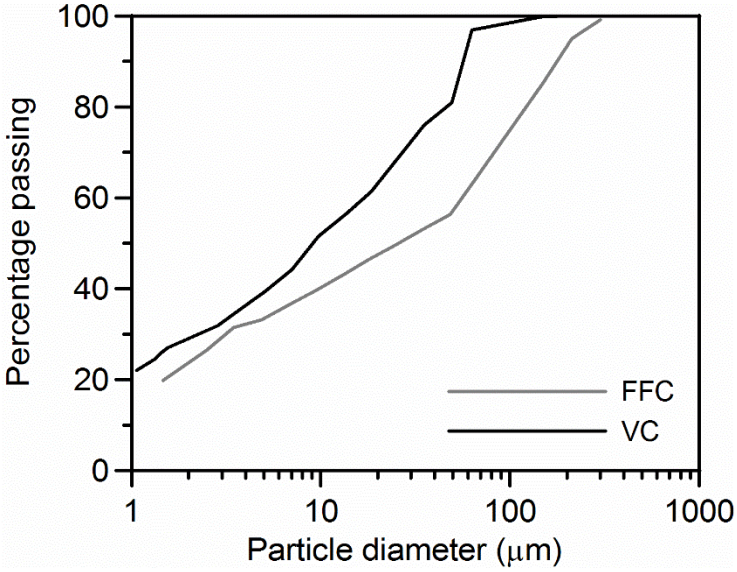

Figure 5-1 Grain size distributions of tested materials

5.3.2 Measurement of pore-water tension in the low pore-water tension range

The relationship between pore-water tension and moisture content along a drying path was measured using a high-capacity tensiometer (Tarantino & Mongiovì, 2002), which consists of a water reservoir, a high air-entry ceramic disk (1.5 MPa) and a strain-gauged diaphragm. A review of this measurement technique can be found in Tarantino (2004) and Marinho et al. (2008). The tensiometers used were able to measure pore-water tension up to 2000 kPa, with a measured standard deviation of the error ±1.5 kPa.

Specimens were cut from the cast bars using a 60mm diameter metal cutting ring. Pore-

water tension measurement was carried out in the box illustrated in Figure 5-2 with the specimen enclosed in the cutting ring. O-rings were used to seal the box and to ensure that the water vapour in the box could reach equilibrium with the specimen water.

Two tensiometers were used simultaneously to measure the pore-water tension. The use of two tensiometers made it possible to check the reliability of the measurement by ensuring that the two probes returned similar values.

Once the tensiometers recorded a stable value of the pore water tension the specimen was placed in the oven for 24hrs to obtain the moisture content at the measured pore-water tension.

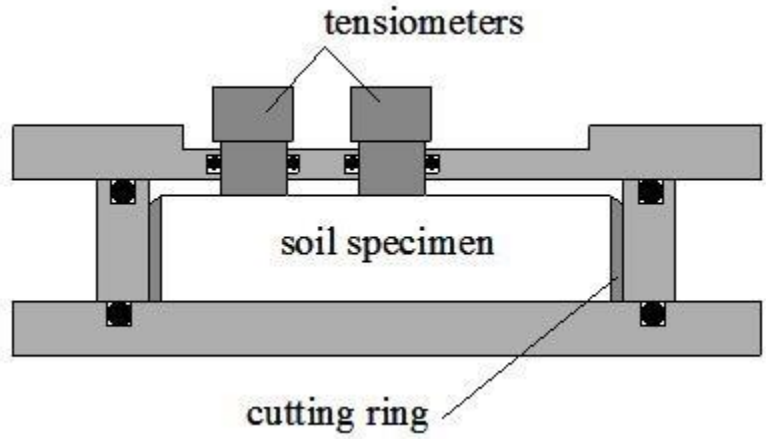

Figure 5-2 Suction measurement box (Tarantino et al. 2010)

5.3.3 Measurement of pore-water tension in the high pore-water tension range

Measurement of pore water tension beyond the range of the tensiometers was performed using a WP4C dewpoint potentiometer. The WP4C uses the chilled mirror method to determine the relative humidity of the air around a sample in a sealed chamber once the sample has come into equilibrium with the vapour in the surrounding air. At the dew point the WP4C measures the temperature of the sample and the surrounding air. Calibration of the device was achieved by using sodium chloride solutions with known water potentials with a measured standard

deviation in accuracy of ±30 kPa. Further information on the use of the WP4C can be found in Decagon devices (2014).

Small specimens were cut from the dried bars and placed into the device. At the end of the measurement the specimen was placed into an oven to obtain the moisture content related to the pore water tension.

5.3.4 Measurement of void ratio

Disc samples were cut from the cast bars dried to target water contents using a small cutting ring, 15.5 mm inner diameter and 12.5 mm high. Excess clay was trimmed from the top and base of the cutter. The specimen volume was then derived from the inner dimensions of the cutting ring. The specimen was put in the oven at 105°C for 24 hours to determine the moisture content. The void ratio was then calculated from the measurements of specimen volume and moisture content.

5.3.5 Measurement of pore-size distribution

Specimens cut from the cast bars and dried to target water content were dehydrated using a freeze-drying technique, using liquid nitrogen and Isopentane, as described in Tarantino & De Col (2008) and Pedrotti (2016).

Mercury intrusion porosimetry was carried out using a PoreMaster–60 produced by Quantachrome Instruments. The equipment is designed to measure pore entrance diameters in the range of 1000 μm to 0.003 μm, corresponding to 1.5-420,000 kPa mercury intrusion pressure respectively. The parameters used for the interpretation of the test are as follows:

- Mercury surface tension, γ = 0.484 N/m (Diamond, 1970)
- Mercury-specimen contact angle, θ =147° (Diamond, 1970)

- Specific gravity, $G_{s,VC}$ = 2.63 g/cm^3, $G_{s,FCC}$ = 2.66 g/cm^3 (tested using pycnometer in accordance with BS 1377-Part 2, 1990)

5.4 Results

5.4.1 Water and volume change upon drying

Figure 5-3 shows the response of the two materials upon drying in terms of void ratio, *e* (ratio of volume of voids to volume of solids) versus gravimetric moisture content *w* (ratio of mass of water to mass of solids). The curve represented in the figure is essentially the classic Bigot's curve with a slightly different representation of the volume change.

The slope of the line at high values of moisture content (saturated range) is determined by the specific gravity, G_s, of the material (2.63 for VC and 2.66 for FFC). This is defined as the ratio between the density of the solids and the density of the pore-water. Since the values of specific gravity are very similar, the slopes of the two Bigot's curves in the saturated range for the two materials are very similar.

The VC material shows a slightly larger reduction in void ratio than the FFC from the initial state to the point where the value of void ratio effectively becomes constant (Δe = 0.10 for VC and Δe = 0.07 for FFC). In other words, the VC materials experiences slightly higher volume change upon drying after removal from the casting mould.

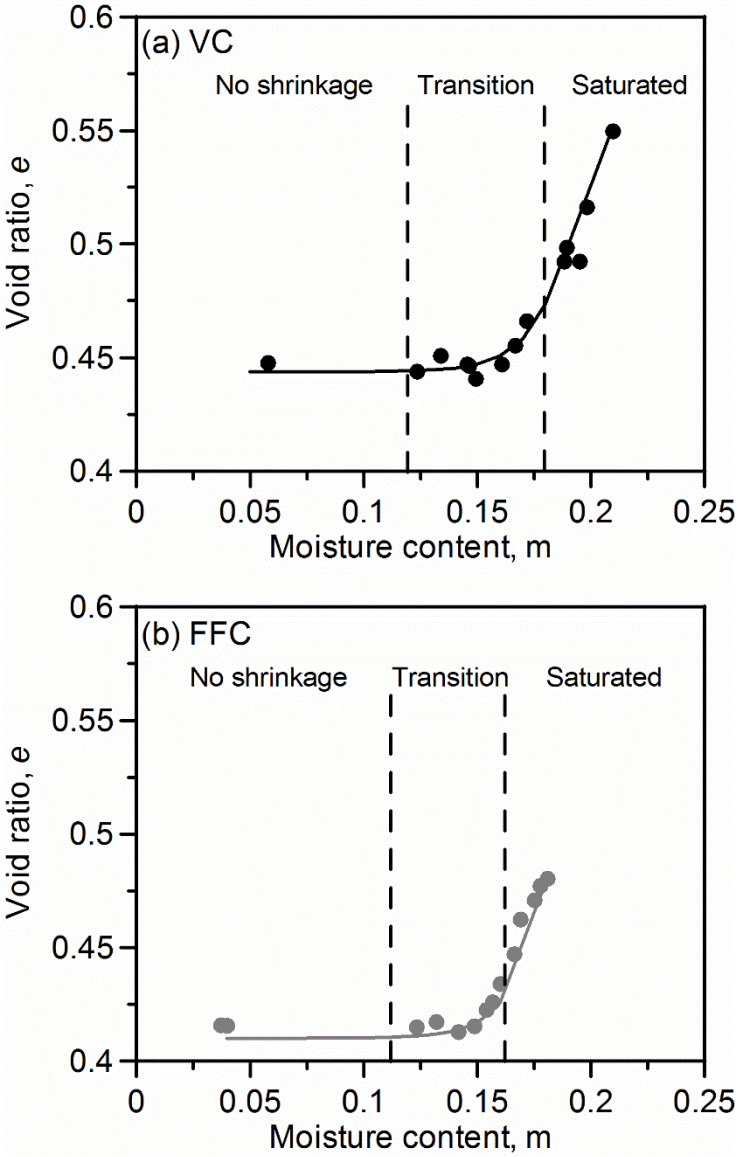

Figure 5-3. Bigot's curves for (a) VC and (b) FFC

The experimental data in Figure 5-3 can be fitted with the following equations:

$$e = w.G_s \quad (w > w_{AE}) \qquad [5.1a]$$

$$e = e_{res} + \frac{(e_{AE} - e_{res})}{exp[\delta(w_{AE} - w)]} \quad (w < w_{AE}) \qquad [5.1b]$$

where w_{AE} is the moisture content at air entry, G_s is the specific gravity of the material, e_{res} is the residual void ratio, e_{AE} is the void ratio at air entry, and δ is a fitting parameter. The values of the parameters used are given in Table 5-1.

Table 5-1. Parameters of the Bigot's curve

	w_{AE} [–]	G_s [–]	e_{res} [–]	e_{AE} [–]	δ [–]
VC	0.182	2.63	0.444	0.48	73.2
FFC	0.159	2.66	0.410	0.423	75.4

The drying curves in the pore-water tension T versus degree of saturation S_r (water retention behaviour) and water tension T versus void ratio e (volume change behaviour) planes are shown in Figure 5-4. These show the evolution of the volumetric variables as the pore-water tension increases upon drying.

The degree of saturation S_r was calculated from the value of moisture content w of the specimens whose pore-water tension was measured with high-capacity tensiometers or WP4C, and the void ratio e was inferred from Eq. 5.1 ($S_r = w \cdot G_s / e$).

The overall change in void ratio accumulated over the drying process is not significantly different for the two materials. The major difference appears to be the transition from saturated to unsaturated states, which is much more gradual for the FFC. The same response appears in the plane T-S_r. The onset of desaturation occurs at a very similar water tension range for the two materials. However, the FFC shows a much more gradual decrease in degree of saturation as pore-water tension increases.

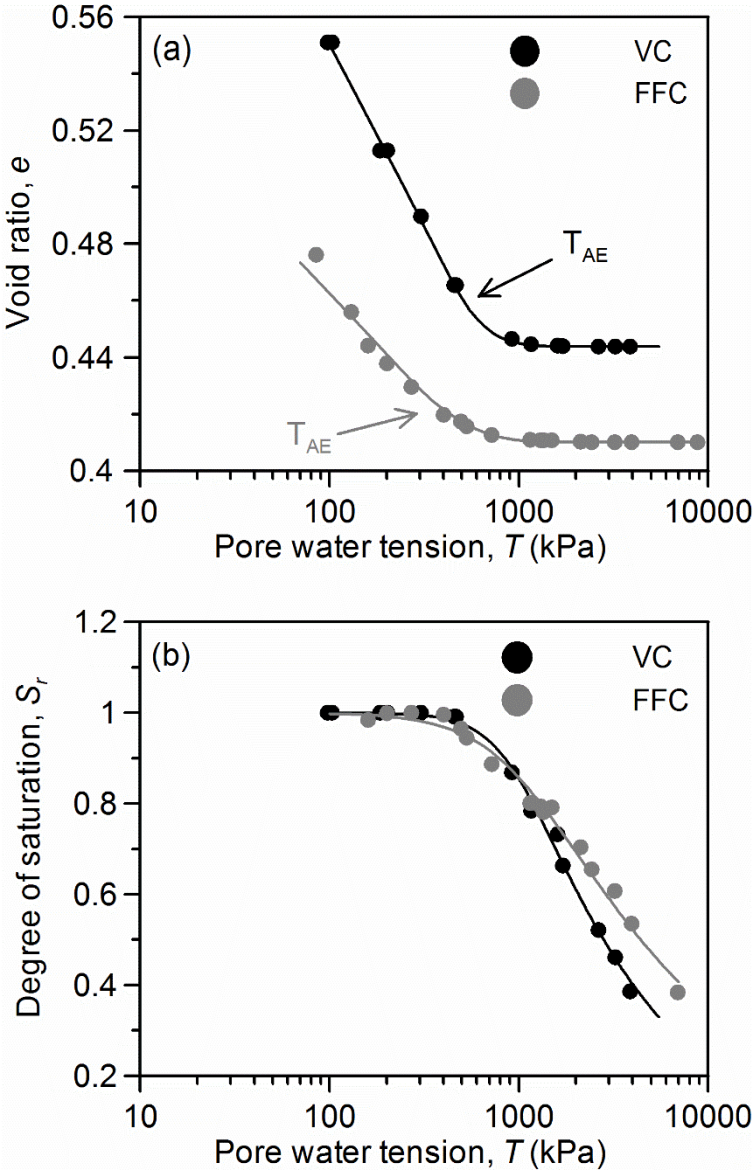

Figure 5-4 Drying curves for the tested materials (a) void ratio (b) degree of saturation

The experimental void ratio data in Figure 5-4a were fitted using the following equations:

$$e = N - \lambda \cdot ln(T) \qquad (T < T_{AE}) \qquad [5.2a]$$

$$e = e_{res} + \frac{(e_{AE} - e_{res})}{exp(a(s - s_{AE}) + b(T - T_{AE})^c)} \qquad (T > T_{AE}) \qquad [5.2b]$$

where N, λ, a, b and c are fitting parameters and T_{AE} is pore-water tension at air entry. The values of the parameters used are given in Table 5-2.

The experimental data in terms of degree of saturation in Figure 5-4b were fitted using the van Genuchten (1980) equation:

$$S_r = (1 + (\alpha \cdot T)^n)^{-m} \qquad [5.3]$$

where α, n and m are fitting parameters, shown in Table 5-2.

Table 5-2. Parameters of volume change and water retention curves

	N [–]	**λ** [–]	***a*** [kPa^{-1}]	***b*** [kPa^{-1}]	***c*** [–]	T_{AE} [kPa]	**α** [kPa^{-1}]	***n*** [–]	***m*** [–]
VC	0.807	0.056	0.0045	0.001	1	400	0.0011	3.23	0.193
FFC	0.603	0.031	0.0036	0.001	1	320	0.001	2.07	0.222

5.4.2 Pore-size distribution upon drying

Figure 5-5 shows the samples that were tested in the Mercury Intrusion Porosimeter (MIP) to obtain their Pore-Size Distribution (PSD). Three samples were tested for both materials, with one sample each taken from the saturated branch, the transition zone, and the constant volume branch of the Bigot curve.

Figure 5-6a and Figure 5-6b show the evolution of the frequency pore-size distributions for the VC and FFC materials respectively. As drying proceeds, the modal value decreases and frequency increases. This occurs because larger pores are shrinking and therefore add to the

number of small and intermediate sized pores already existing at the point where the pores were formed. It can be seen from the figure that the small pores, below 0.06 μm for the VC and 0.03 μm for the FFC, are largely unaffected by the drying.

It is interesting to compare the PSDs of the two materials in the saturated, transition zone, and constant volume zones respectively as shown in Figure 5-7. The PSD is significantly wider for FFC in the saturated state, in the sense that the FFC material is populated by larger pores (Figure 5-7a). These larger pores tend to reduce in the transition zone (Figure 5-7b) and eventually disappear when the constant volume stage is attained (Figure 5-7c). It is interesting to note that no pores larger than 1 μm exist for both materials in the constant volume zone.

The more graded PSD of the FFC in the saturated state (Figure 5-7a) is a result of the better graded grain size distribution of the FFC as shown in Figure 5-1. In turn, the better graded PSD of the FFC in the saturated state generates a more gradual desaturation of the material as shown Figure 5-4b.

In other words, a well graded grain size distribution generates a material that desaturates more gradually, and this is a key factor in controlling the mechanisms of drying-induced cracking, as will be discussed in the next section.

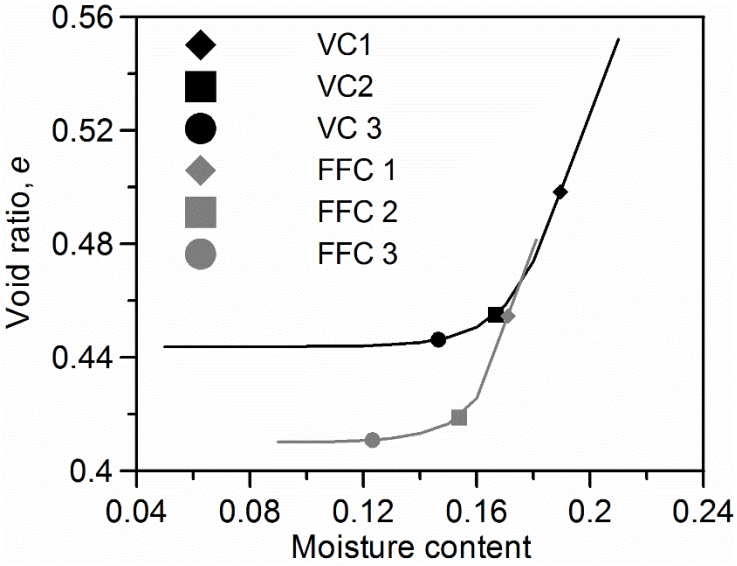

Figure 5-5 Location of MIP test samples on Bigot curve

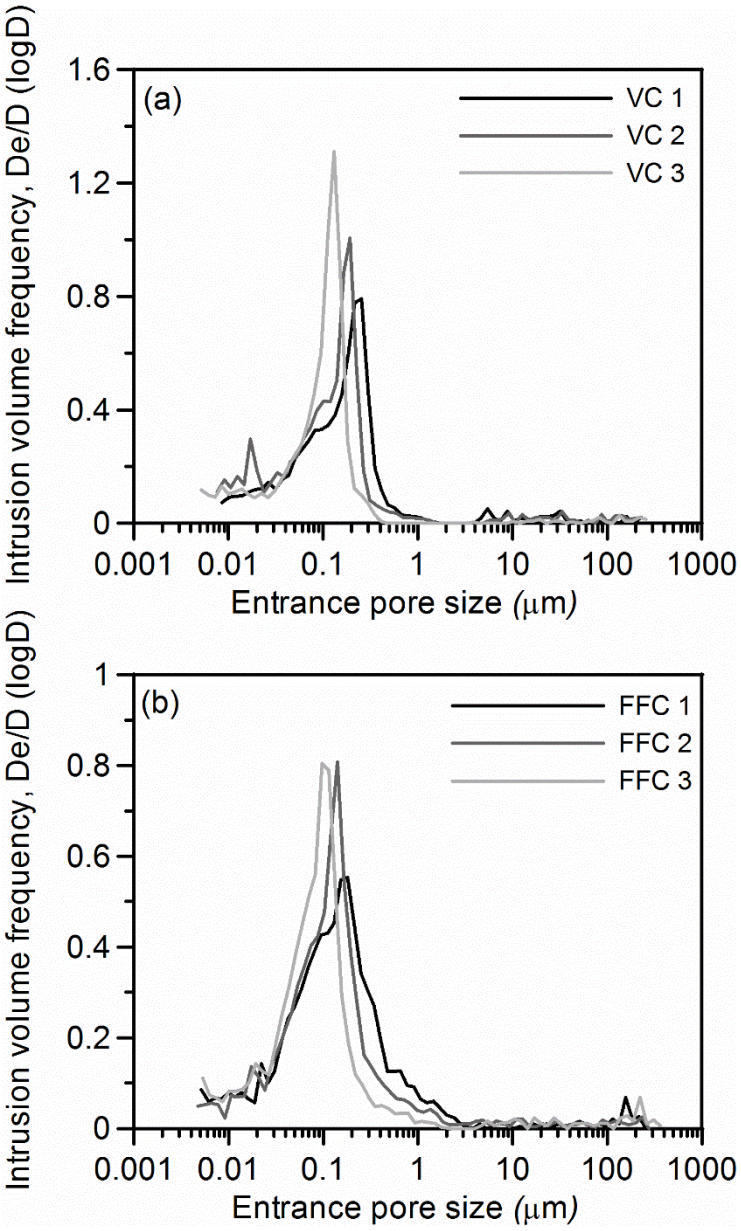

Figure 5-6 Pore size distribution for (a) VC and (b) FFC materials

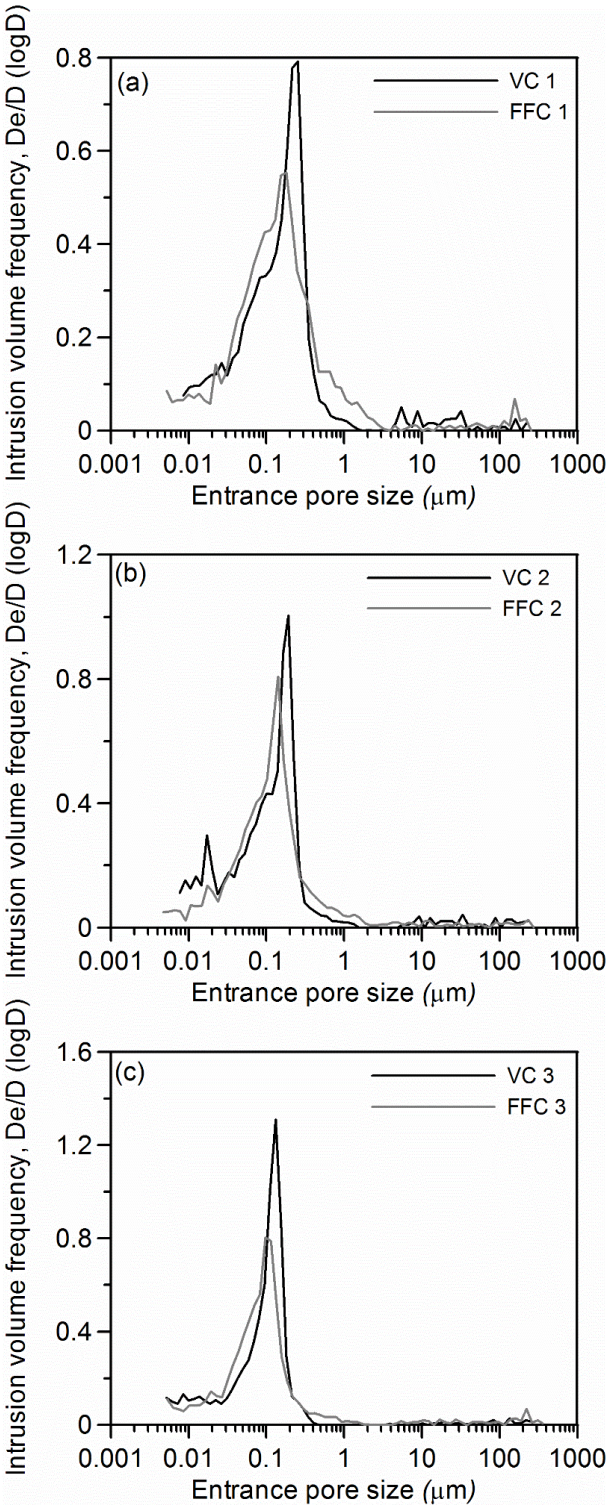

Figure 5-7. Comparison of the pore size distributions of the tested materials at different stages

of drying (a) saturated, (b) transition, and (c) constant volume

5.5 Discussion

The two materials investigated in this experimental programme, the Vitreous China (VC) and the Fine Fire Clay (FFC) respectively, have been selected because of their different susceptibility to cracking in a green state. In particular, the VC material has been observed to be more prone to cracking upon drying than the FFC. The Grain Size Distribution (GSD) of the two materials and the Pore-size distribution (PSD) and Water Retention Curve (WRC) therefrom, can be the key to understanding the microstructural reasons for this.

Prior to analysing the interplay between susceptibility to cracking and grain- and pore-size distribution from a quantitative point of view, a conceptual (qualitative) model for crack initiation is discussed. Because evaporation rate and uniformity of drying have been widely acknowledged to control the susceptibility to cracking of green bodies (Bowman, 1926; Sokolov & Gak, 1959; Ford, 1986; Fraser, 1986; Reed, 1988; Scherer, 1990; Clausen & Fish, 1994; Gur’yanov & Zakharov, 2007; Zhu & Leak, 2017), we consider the case of a simple clay green form subjected to non-uniform drying. The quality of the conceptual model can then be tested against its capability to reproduce, at a qualitative level, the effect of evaporation rate during drying on the susceptibility to cracking. The case of a disc subjected to drying at its edge and the outer portion of its top surface was considered (Figure 5-8).

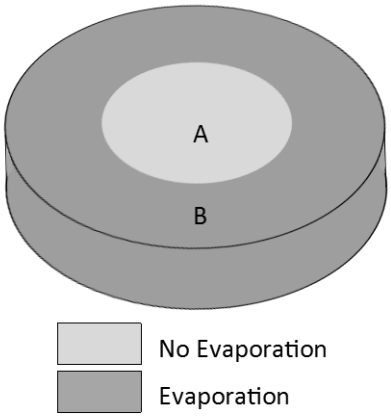

Figure 5-8 Drying conditions of disk

After removal from the casting mould, pore-water tension is uniform within the body (point A=B in Figure 5-9). During the initial stage of drying, both the inner (A) and outer parts (B) move along the saturated curve. Despite having different values of pore water tension, they are both deforming (A’ and B’ Figure 5-9) and no significant shear strains and stresses develop between the inner and outer parts. As drying proceeds, the outer part of the bar will reach the rigid part of the drying curve (A’’ Figure 5-9) while the inner part will be still be on the deformable part of the drying curve (B’’ Figure 5-9). As the inner part continues to dry, it will shrink against the rigid outer part. This causes differential shear strains and stresses, leading to cracking.

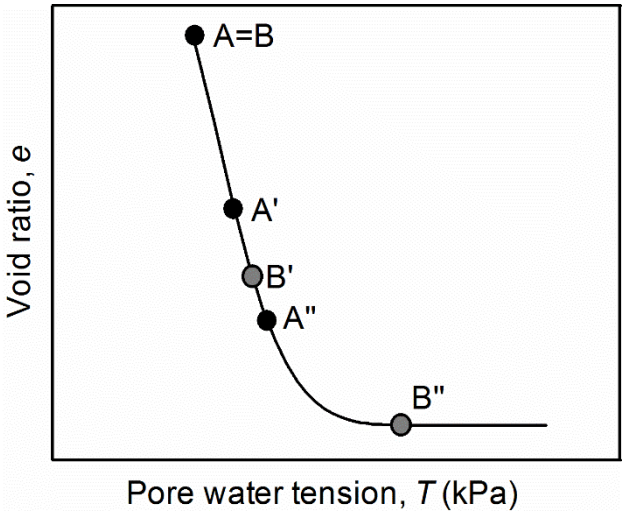

Figure 5-9 Conceptual model for cracking

This conceptual model can explain the effect of evaporation rate in a straightforward fashion. For the case of low evaporation rate, smaller gradients of pore-water tension will develop across the sample. The points associated with the inner and outer part would therefore lie very close to each other, on either the deformable or rigid part of the drying curve and no significant differential shrinkage between the inner and outer regions would occur. On the other hand, a high evaporation rate will generate higher gradients in pore-water tension and hence, the likelihood that the inner and outer parts of the bar fall on the two parts of the drying curve. The susceptibility to cracking will therefore increase due to significant differential shrinkage associated with the evaporation rate, as is often reported in literature.

With this conceptual model in mind, one can attempt to explain why the VC material is more susceptible to cracking than the FFC material. As shown in Figure 5-4, the transition zone for the FFC (the range of pore-water tension between the desaturation point and the constant volume zone) is much wider than the VC, i.e. the transition from the deformable to the rigid part of the drying curve is much more gradual for the FFC. As a result, the chance that the inner

and outer parts are on the two different parts of the drying curve is lower and, hence, the likelihood of cracking is reduced.

The gradual transition for the FFC is in turn associated with a more graded pore size distribution (Figure 5-6b), which is in turn associated with a more graded grain size distribution (Figure 5-1). In the end, it can be considered that the gradation of the grain size distribution is a key aspect in the design of the mix.

5.6 Numerical testing of remedial measures

In order to probe the conceptual model and demonstrate convincingly that the gradual transition between the deformable and rigid part of the drying curve plays a critical role in the cracking mechanism, a numerical model has been developed using GeoStudio, based on a simple case study.

5.6.1 Case study

The numerical model is based upon cracking in a cylindrical disk of clay, shown in Figure 5-10. The centre part of the disk is initially covered to prevent evaporation from the centre part of the top of the disk, while evaporation is allowed from the outer half of the top face and the sides of the disk. This allows the outer parts of the disk to dry more rapidly, creating a gradient in the pore water tension between the centre and outer parts of the disk, eventually leading to cracking. As shown in Figure 5-10, a crack developed from the centre and propagated towards the periphery of the disk.

The mechanisms leading to cracking were discussed in qualitative fashion in the previous section. The challenge pursued here is the capability of a numerical model to capture the initiation of a crack at the centre of the disk.

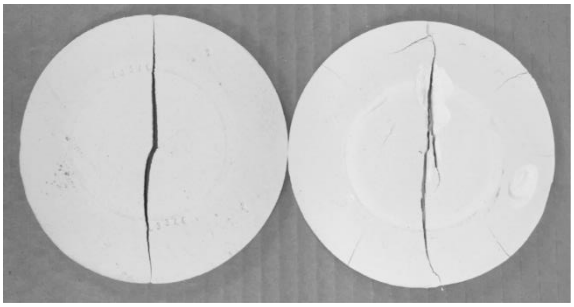

Figure 5-10 Case study - Cracking in cylindrical disk
(https://digitalfire.com/4sight/glossary/glossary_drying_crack.html *courtesy of Tony Hansen*

5.6.2 Hydro-mechanical model

The water flux imposed at the boundary by the evaporation process generates a water flux with the clay form and, hence, gradients in pore-water tension. In turn, changes in pore-water tension cause mechanical deformation of the clay skeleton affecting its water storage capacity. In other words, the evaporation-induced water flow in an initially saturated body is a hydro-mechanical coupled process that requires water mass balance and momentum balance equations to be solved simultaneously.

The water mass balance can be written as follows:

$$div\left(\vec{v}\right) = -\frac{\partial \theta}{\partial t} \qquad [5.4]$$

where $\vec{v}$ is the flow velocity, θ is the volumetric water content (volume of water per total volume), and t is the time. In Eq. [5.4], the flow velocity is given by the Darcy-Buckingam law (Fredlund & Rahardjo, 1993; Lu & Likos, 2004):

$$\vec{v} = -k\left(e, S_r\right) \cdot grad\left(\frac{u_w}{\gamma_w} + z\right) \qquad [5.5]$$

where u_w is the pore-water pressure (the opposite of the pore-water tension), z is the vertical coordinate increasing upward, γ_w is the specific weight of water, and k is the hydraulic conductivity, which depends on void ratio e and degree of saturation S_r (Mitchell, 1993). Eq. 5.5 neglects diffusive and advective transport of water vapour and this assumption is corroborated by numerical simulation of isothermal drying in low-permeability materials (Baroghel-Bouny, et al., 2001; Coussy, 2004). The volumetric water content can be expressed as a function of S_r and e as follows:

$$\theta = \frac{e\left(\sigma_{ij}, u_w\right)}{1 + e\left(\sigma_{ij}, u_w\right)} \cdot S_r\left(u_w\right) \qquad [5.6]$$

Since the void ratio e and, hence, the volumetric water content θ, also depend on the total stress tensor σ_{ij}, Eq. [5.6] can only be solved if coupled with the momentum balance equations (Biot, 1941), which can be written under the assumption of static equilibrium as follows:

$$\frac{\partial \sigma_{ij}}{\partial x_i} + \rho b_j = 0 \qquad [5.7]$$

where ρ is the clay bulk density and b_j is the body force. For the desiccation test examined here, which involves shrinkage of a thin clay disc, we can assume $b_j \cong 0$.

Finally, a mechanical constitutive law needs to be introduced to pair the number of equations with the number of unknowns. The clay has been assumed to have non-linear elastic

behaviour (constant Poisson's ratio ν and non-linear Young's modulus E), with the strains dependent on the effective stress tensor $\sigma'_{ij} = \sigma_{ij} - u_w$. Although the Young's modulus E depends on the isotropic effective stress, in principle it actually depends, essentially, on the pore-water tension T in the application considered herein since there are no external stresses applied to the disk and this generates small isotropic total stresses within the disk.

This is the reason why the Young Modulus E has been derived experimentally from the relationship between the volumetric strain and pore-water tension T (rather than the relationship between volumetric strain and isotropic effective stress p'). In particular, the Young modulus E was derived from the drying curve in the void ratio-pore water tension plane (T,e) (Figure 5-4a) as follows:

$$E = 3(1-2\upsilon)K = 3(1-2\upsilon)\frac{dT}{d\varepsilon_v} = 3(1-2\upsilon)\frac{dT}{d\left(\frac{e}{1+e}\right)} \quad [5.8]$$

where K is the bulk modulus and ε_v is the volumetric deformation.

5.6.3 Hydro-mechanical properties of the clay

In order to model the hydro-mechanical effects of drying, a number of constitutive relationships need to be defined. The degree of saturation S_r appearing in Eq. [5.6] was modelled using the function shown in Eq. [5.3]. The void ratio e appearing in Eqs. [5.6] and [5.6] was modelled using the function shown in Eq. [5.2]

To characterise the hydraulic conductivity k appearing in Eq. [5.5], the Kozeny-Carman equation was used according to Tarantino et al. (2010):

$$k = k_{sat} \cdot S_r^3 \qquad [5.9]$$

where k_{sat} is the saturated hydraulic conductivity, which was assumed to be equal to $5 \cdot 10^{-11}$ m/s in this exercise.

The numerical model implemented is based upon the assumption that the material has a linear elastic behaviour without explicitly introducing a yield and failure criterion in the model.

To characterise the onset of cracking, the assumption is made that failure occurs when a critical value of the deviator stress is attained:

$$q_f = M(p + T \cdot S_r) = Mp'' \qquad [5.10]$$

where p is the isotropic total stress and M is a soil parameter, and p'' is the effective stress. This is consistent with tensile failure criterion proposed in paragraph 3, based on uniaxial tensile tests on the VC material.

The deviator stress q and the isotropic effective stress p' under axisymmetric conditions are defined as follows:

$$q = \frac{1}{\sqrt{2}}\sqrt{(\sigma_a - \sigma_r)^2 + (\sigma_r - \sigma_\theta)^2 + (\sigma_\theta - \sigma_a)^2} \qquad [5.11a]$$

$$p'' = \frac{\sigma_a + \sigma_r + \sigma_\theta}{3} + \mathrm{T} \cdot S_r \qquad [5.11b]$$

where σ_r is the radial stress, σ_a is the axial stress, and σ_θ is the circumferential stress.

5.7 Numerical modelling of evaporation test

The numerical modelling of the coupled hydro-mechanical process induced by drying requires the definition of the initial and boundary conditions, for both the hydraulic and the mechanical components of the model.

The initial pore-water tension was assumed to be hydrostatic and equal to 130 kPa at the base of the disc. A hydraulic flux v_z was imposed on a portion of the boundary as shown in Figure 5-11. This figure only shows the axisymmetric part of the disc with the vertical axis representing the axis of symmetry of the disc.

The pore-water tension of 130 kPa also establishes the initial stress condition for the mechanical component of the numerical model. The disc was allowed to shrink in a radial direction, i.e. rollers were placed at the bottom of the disc.

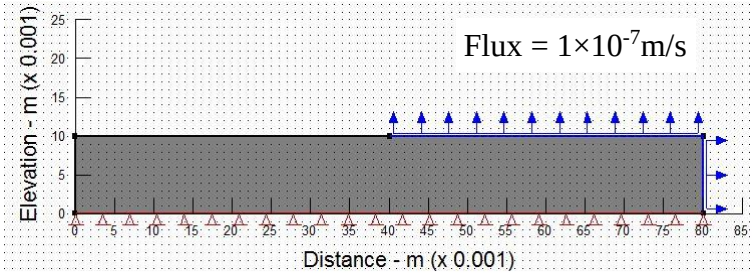

Figure 5-11 Boundary conditions of reference evaporation test

The results of an evaporation test in terms of the evolution of the mobilised strength q/p'' at the bottom centre of the disc is shown in Figure 5-12 (evaporation rate of $v_z = 10^{-7}$ m/s). This simulation was performed using the stiffness vs pore water tension relationship derived from

the real material (*VC2*).

It can be observed that the mobilised strength q/p'' first increases and then decreases until reaching a minimum where cracking can potentially occur if the mobilised strength q/p'' exceeds the shear strength M according to Eq. [5-10].

The non-monotonic evolution of the mobilised shear strength can be explained qualitatively as shown in Figure 5-13 . Initially, only the outer part of the disk tends to shrink because pore-water tension gradients are only generated close to the boundary where water is extracted. The horizontal deformation of the outer part towards the inner part of the disk compresses the inner part (Figure 5-13a). As pore-water tension propagates from the outer to the inner part, the inner part also starts deforming. At this point the outer part is semi rigid and so the horizontal deformation of the inner part is greater. The differential deformation tends to reduce and so do the tangential stresses between the inner and outer part of the disk (Figure 5-13b). This is the reason why the deviator stress first reaches a peak and then starts declining until becoming nil again.

As drying proceeds, the outer part becomes rigid as it reaches the constant volume branch of the Bigot's curve. Since the inner part still undergoes deformation, the outer part now restrains the deformation of the inner part (Figure 5-13c). This causes the inner part to "stretch" as a result of the restrained drying and creates a tensile total stress, generating a deviatoric stress q. This stretching is greatest at the centre of the disk and is the reason the cracks in Figure 5-10 initiate at the centre of the disk. This uneven drying between the inner and outer part explains the change in sign of the mobilised shear strength q/p'' shown in Figure 5-12.

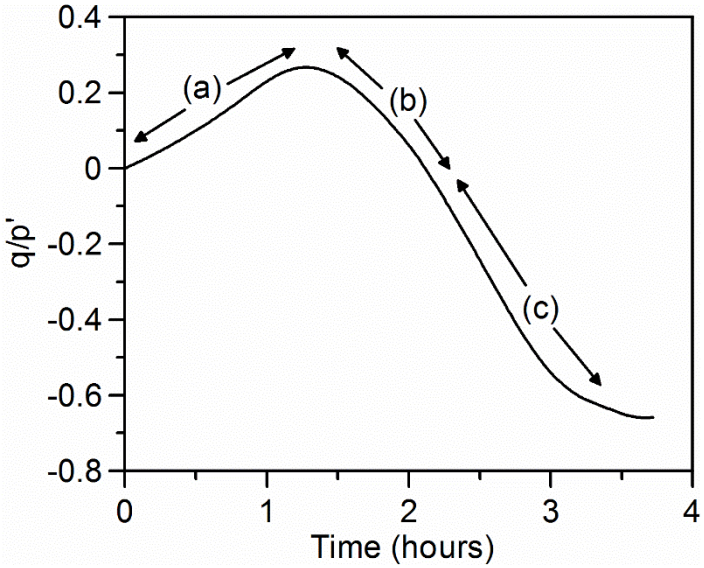

Figure 5-12 Results of numerical simulation for reference test (v_z= 10-^{7} m/s)

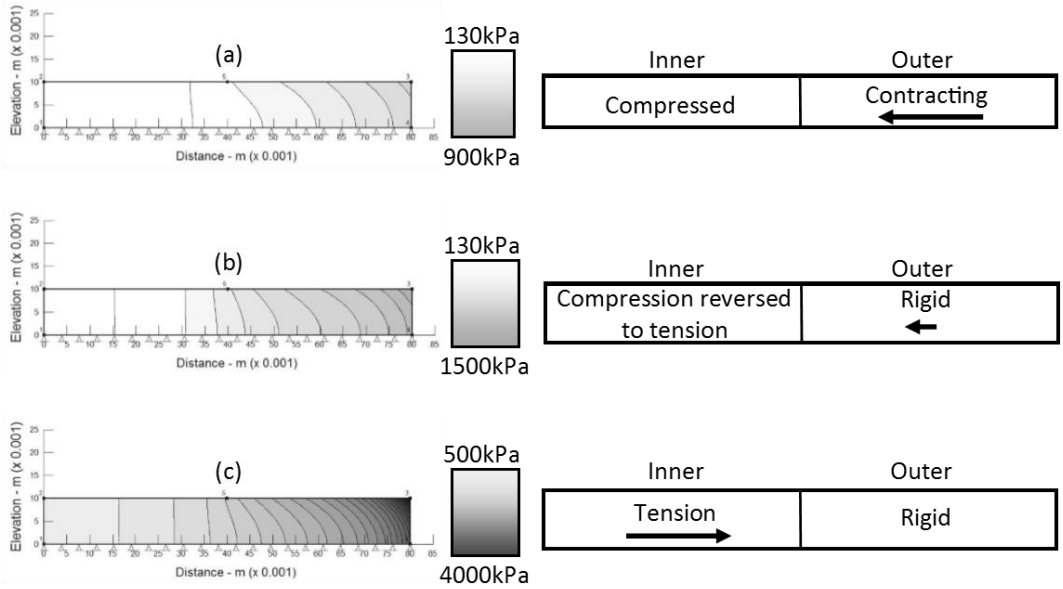

Figure 5-13 Pore water tension and deformation at different stages of standard evaporation simulation

5.7.1 Effect of evaporation rate

To test the capability of the hydro-mechanical model to capture the mechanisms of cracking upon drying, the case of a disc subjected to different evaporation rates was considered. As mentioned previously, it is well known that susceptibility to cracking can be reduced by slowing down the rate of evaporation.

Figure 5-14 indeed shows that the deviatoric to isotropic stress ratio reaches its lowest values for the highest evaporation rate, which makes the clay disc more prone to failure.

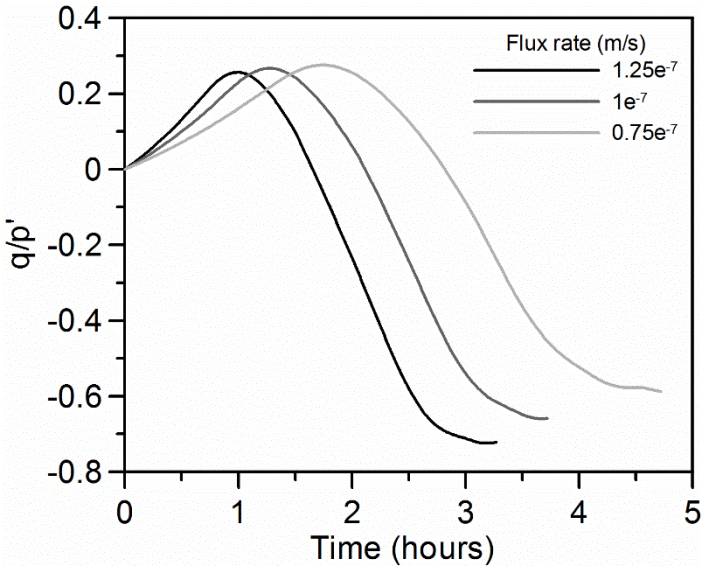

Figure 5-14 Effect of the evaporation rate

5.7.2 Effect of gradation of shrinkage curve

To test numerically the effect of the gradation of the transition zone, i.e. the zone marking the transition from the saturated branch to the constant volume branch of the drying curve, two fictitious materials were considered (VC A and VC C) as shown in Figure 5-15. These are differentiated from the real material (VC B) by a different gradation of the transition zone.

As shown in Figure 5-16, when the materials transition zone is sharper (VC A), the peak

deviatoric stress is lower and, hence, the susceptibility to failure is higher. This is because it has a higher contrast in stiffness between the inner saturated zone and the outer drier zone as shown in Figure 5-17. The opposite effect to this can be seen for VC C.

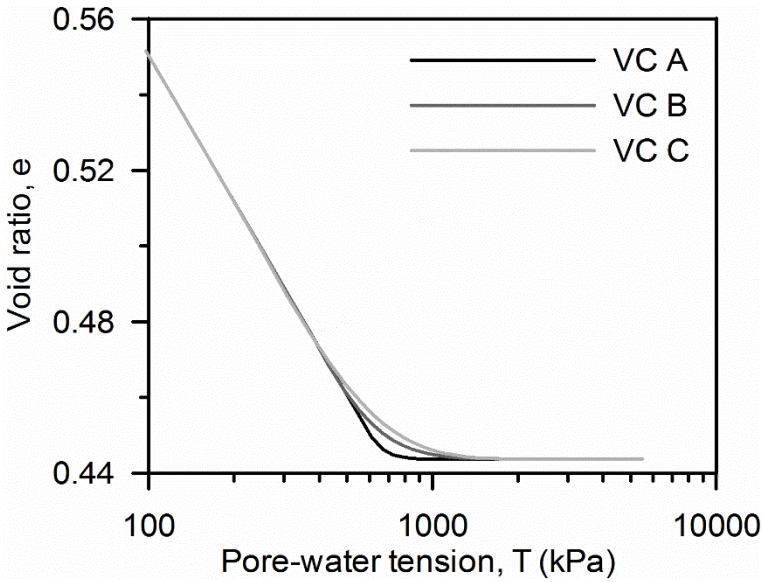

Figure 5-15 Materials used to assess the effect of the gradation of the transition zone

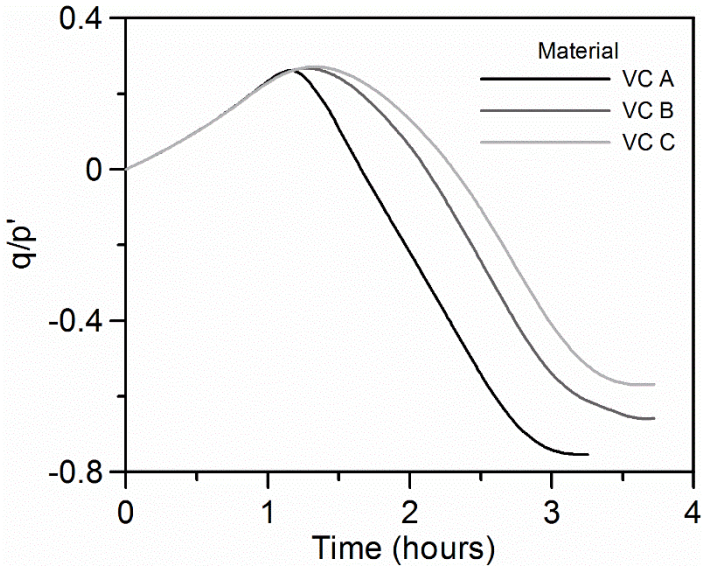

Figure 5-16 Results of evaporation simulations for the 3 materials with different sharpness of transition zones

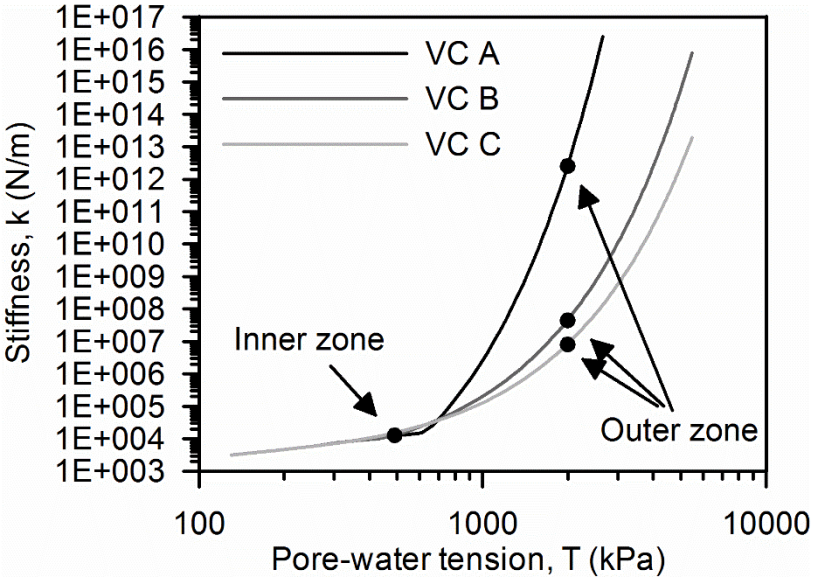

Figure 5-17 Effect of changing the gradation of transition zone in terms of stiffness

5.8 Conclusions

This paper has presented an experimental investigation into the microstructural features characterising the susceptibility to cracking of greenware upon drying. Fine Fire Clay and Vitreous China have been selected in this investigation because of their different susceptibility to cracking and have been compared in terms of grain-size distribution, pore-size distribution, and drying (Bigot) curve.

It has then been observed that the material characterised by lower susceptibility to cracking shows more graded grain-size and pore-size distributions and, hence, a more gradual transition from the saturated branch to the constant volume branch of the Bigot curve. It has been demonstrated that this transition plays a key role in controlling the formation of cracking upon drying via a hydro-mechanical coupled FEM analyses of a disc subjected to non-uniform drying.

These numerical analyses have therefore suggested a potential remedial measure for

greenware cracking. If the grain size-distribution is modified to be more well graded, a more graded pore-size distribution and, hence, a more gradual transition from the saturated to the constant volume branches are generated. In turn, this reduces the contrast in stiffness between zones subjected to a different degree of drying and then reduces the susceptibility to cracking.

5.9 Acknowledgments

The authors wish to thank Ideal Standard International and EPSRC Doctoral Training Grant for supporting the research.

6 CONCLUSIONS

This thesis was aimed at enhancing the understanding of cracking behaviour of clayey geomaterials by applying experimental, numerical and theoretical approaches.

The main goals of this work were to:

5. Develop a new tensile experimental test for clays with the ability to measure negative pore-water pressure.
6. Identify the crack initiation mechanism for both saturated and unsaturated states.
7. Develop a numerical model that encapsulates the crack initiation mechanism to simulate the drying of clay forms and predict the time and location of cracking.
8. Provide practical guidance for the ceramic industry on how to prevent/reduce instances of cracking in their production.

6.1 New tensile testing method

A new apparatus for investigating the behaviour of clayey geomaterials subjected to a directly applied tensile (negative) total stress has been presented. A key feature of the apparatus is the facility to monitor, using high capacity tensiometers, the pore-water pressure of the test specimen. This allowed for the data at failure to be interpreted in terms of effective stress rather than total stress. To date, the vast majority of tensile testing apparatus did not include pore-water pressure measurement. The specimen shape has been improved from those found in the literature to ensure that the direction of the major principal stress in the failure zone coincides with the direction of the externally applied tensile force, allowing for a more accurate analysis of tensile failure.

Results are shown for saturated specimens and compared to results obtained for the same

soil in uniaxial compression, using a modified version of the presented uniaxial tensile method, and a triaxial compression test. It is demonstrated that that crack initiation occurs by shear failure if data are interpreted in terms of effective stress rather than total stress and that the failure mechanisms under tension do not differ from compression.

6.2 Mechanism of crack initiation

An experimental investigation of the mechanisms of crack initiation in clayey geomaterials under saturated and unsaturated conditions utilising the developed tensile testing equipment was shown. Using high-capacity tensiometers allowed interpretation of the data to be done in terms of effective stress for the saturated specimens and in terms of average skeleton stress for the unsaturated specimens.

A first series of test were performed on saturated samples of Vitreous China clay and Speswhite kaolin clay reconstituted from slurry (prepared by slip-casting) using non-de-aired water. The results showed that for specimens tested at low suction, the state of stress at failure was aligned with the critical state line derived from the compression tests, indicating a shear failure mechanism. However, the results showed that, for specimens where the suction was approaching the material air-entry value, failure occurred at a deviator stress lower than the one corresponding to the critical state line derived from triaxial and uniaxial compression tests. This behaviour was observed for both clay materials tested.

Although all specimens were tested in the saturated range, it was speculated that small air cavities could exist in the soil when the suction approaches the air-entry value. When the specimen is pulled under undrained conditions, suction increases and some pre-existing air cavities can trigger cavitation within the pore-water. The loss in suction in the cavitated area is

in turn associated with a loss in the ‘confining’ effective stress and the sample would experience an earlier than expected failure.

This assumption was assessed by performing a second series of tests on saturated specimens with the slurry preventatively being de-aired before slip casting. The de-airing process was aimed at reducing the number of cavitation nuclei within the clay, therefore reducing the probability of an early failure due to water cavitation. The results of this test series showed that the de-airing process realigned the deviator stress at failure, recorded in the tensile test, with the critical state line derived from uniaxial and triaxial compression tests. It was therefore demonstrated that water cavitation is one of the mechanisms that can control rupture of clay when subjected to a (total) tensile stress state.

Failure data on unsaturated specimens (only one material was tested) could be fairly modelled by the Mohr-Coulomb criterion extended to unsaturated states. This was achieved by replacing the effective stress for saturated geomaterials with the average skeleton stress. This has confirmed that tensile failure is associated with failure in shear, even in the unsaturated state.

Finally, the effect of cavitation on the plastic limit was determined for the two clays tested in this experimental programme by preparing the clays with either non-de-aired or de-aired water. The results showed that the water content at the plastic limit decreases for the case where the specimens were prepared using de-aired water, corroborating the theory proposed in the literature that cavitation influences the cracking that is used to determine the plastic limit of soils.

6.3 Modelling of the drying process to predict crack initiation

A simple 3D coupled hydro-mechanical Finite Element Method model was presented. The model was used to simulate the drying, to the point of crack initiation, of laboratory evaporation tests on restrained specimens with different hydraulic boundary conditions. The model uses an effective shear failure mechanism, as shown in Chapter 3, to predict the time and location of cracking.

The results of the simulations showed some promising results. The prediction of cracking location was realised, in addition to a good agreement of the experimental cracking times for three of the four evaporation tests. However, the model was not able to accurately simulate the forces generated upon the restraints. To overcome this, new simulations using a different value for Poisson’s ratio were performed. The results of these simulations gave an improved match for the experimental force. However, this change resulted in a poor match for the time of cracking.

Proposals have been made for the next set of simulations, where the geometry at the location of cracking will be modified slightly to better represent the laboratory test. It is predicted that this will result in a better simulation of cracking time, while not affecting the location of cracking and simulated forces on the restraints.

6.4 Cracking in the Ceramic Industry

An experimental investigation into the microstructural features that characterise the susceptibility to cracking of ceramic greenware upon drying was shown. Commonly used materials from the ceramics industry, Fine Fire Clay and Vitreous China, were selected for this

investigation because of their differing susceptibility to cracking during drying. The materials grain-size distributions, pore-size distributions, and drying (Bigot) curves were compared to try to identify the reasons for the differing cracking susceptibility.

It was observed that the material showing lower susceptibility to cracking had a more well graded grain-size and pore-size distribution and, therefore a more gradual transition from the saturated section to the constant volume section of its Bigot curve. A hydro-mechanical coupled FEM analysis was then used to simulate the non-uniform drying of a disc. It was demonstrated that this transition plays a key role in controlling the formation of cracking upon drying where the rate of drying was high enough to generate non-uniform pore water pressure gradients that cause different parts of the specimen to be on different parts of the Bigot curve.

These numerical analyses therefore suggested a potential remedial measure for greenware cracking in the ceramic industry. By modifying the grain size-distribution to be more well graded, a more graded pore-size distribution and, hence, a more gradual transition from the saturated to the constant volume branches would be generated. In turn, this reduces the contrast in stiffness between zones subjected to different rates of drying and therefore the susceptibility to cracking.

7 RECOMMENDATIONS FOR FUTURE WORK

7.1 Tensile testing method

Although the testing method presented in this work represents an improvement to existing tensile testing methodologies, there are some modifications to the equipment and testing methods that would improve testing.

The measurement of the specimen's cross-sectional area in the region of failure immediately before cracking was not performed during testing, but was instead calculated form the post failure area. A mechanism which allows this area to be directly measured would increase the accuracy of the calculated stress state at point of failure.

Additionally, the apparatus could be modified to allow strain controlled loading tests to be performed. Stress controlled tests result in the sudden creation and propagation of a fracture, whereas strain controlled tests result in a more stable fracture propagation. This may provide further insight into crack mechanisms

7.2 Mechanism of crack initiation

The author recognises that the conclusions on the mechanism of crack initiation were based upon results from two soils in the saturated range and only one soil in the unsaturated range. Testing of further soils in both saturated and unsaturated states would be useful to further verify the shear failure mechanism. The same suggestion can also be made towards the evidence of cavitation and its effect on the plastic limit.

7.3 Modelling of the drying process to predict crack initiation

The modelling of the time and location of cracking using the model presented in this thesis showed mixed results. Further refinement of the model is therefore required to better reproduce these aspects of the drying process.

The laboratory evaporation tests used only resulted in one location of cracking. It may be possible to modify the test specimen geometry, most likely by using a curve transition from the centre section to the end sections, to be able to generate cracking in the centre section. This would further test the model in terms of its ability to predict the location of cracking.

The model presented is only capable of simulating the drying process to the point of crack initiation. There are numerous examples in the literature where methods of modelling crack propagation have been shown. The combination of the shear failure mechanism with a method of simulating the growth of cracks would allow for the entire process of drying and cracking to be modelled.

7.4 Cracking in the Ceramic Industry

The suggested means by which to reduce a materials susceptibility to cracking by modifying the grain size distribution was presented based upon numerical results. Attempts to verify this should be made in the laboratory by modifying the VC and FFC materials used, in line with the suggestions proposed in this thesis, and subjecting them to cracking tests under controlled drying conditions.

8 REFERENCES

8.1 Chapter 1 References

Ajaz, A., & Parry, R.H.G. 1975. Stress-strain behaviour of two compacted clays in tension and in compression. *Geotechnique*, 25(3): 495-512.

Akazawa, T. 1953. Tension test method for concretes. R.I.L.E.M Bulletin 16, 13-23.

Albrecht, B.A. & Benson, C.H. (2001). Effect of desiccation on compacted natural clay. *J Geotech Geoenviron Eng,* 127, No. 1, 67–75.

Amarasiri, A.L., Costa, S. & Kodikara, J.K. 2011. Determaination of cohesive properties for mode I fracture from compacted clay beams. *Can. Geotech. J*. 38: 1163-1173.

Ayad, R., Konrad, J. M., & Soulie, M. 1997. Desiccation of a sensitive clay:Application of the model CRACK. *Can.Geotech. J*., 34(6), 943–951.

Amarasiri, A. L., & Kodikara, J. 2013. Numerical modeling of desiccation cracking using the cohesive crack method. *Int. J. Geomech*., 10.1061/(ASCE)GM.1943-5622.0000192, 213–221.

Baker, R. 1981. Tensile strength, tension cracks and stability of slopes. *Soils and Foundations,* 21, No. 2, 1–17

Blazejczak, D., Horn, R., & Pytka, J. 1995. Soil tensile strength as affected by time, water content and bulk density," *Int. Agrophysics*, Vol. 9, No. 3, pp. 179–188.

Bronswijk, J.J.B. 1991. Relation between vertical soil movements and water content changes in cracking clays. *Soil Sci. Soc. Am. J*. 55, 1220–1226

Carneiro, F. & Barcellos, A. 1953. Tensile strength of concretes. R.I.L.E.M. Bulletin 13, 99-125.

Colina, H., & Roux, S. 2000. Experimental model of cracking induced by drying shrinkage. *European Physical Journal E*, 1:189-194.

Cooper, A.R. 1978. Quantitative theory of cracking and warping during the drying of clay bodies. In Ceramic Processing Before Firing, GY Onoda and LL Hench (eds). John Wiley & Sons, New York.

Corte, A., & Higashi, A. 1960. Experimental research on Desiccation Cracks in Soil. Research report 66, U.S. Army Snow and Ice and Permafrost Research Establishment.

Costa, S., & Kodikara, J. 2012. Evaluation of J-integral for clay soils using a new ring test. *Geotech. Test. J*., 35(6), 1–9.

Coussy, O., Eymard, R., & Lassabatère, T. 1998. Constituitive modelling of unsaturated drying deformable media. *Journal of Engineering Mechanics*, 124(6): 658-667.

Darcy, H. 1856. Les fontaines publiques de la ville de Dijon. Paris, Dalmont.

Dyer, M.R. 2005. Further tests on fissuring of clay fill at the thorngumbald flood embankment. *Proc. International symposium on advanced experimental unsaturated soil mechanics*, Trento, Italy.

Farrell, D.A., Greacen, E.L., & Larson, W.E. 1967. The effect of water content on axial strain in a loam soil under tension and compression. *Soil Science Society of America Proceedings*, 31(4): 445-450.

Fredlund, D.G., & Rahrdjo, H. 1993. Soil Mechanics for Unsaturated Soils. John Wiley & Sons.

Frydman, S. 1964. The applicability of the Brazilian (indirect tension) test of soils. *Aust. J. Appl. Sci.*, Vol. 15, pp 335–343.

Griffith A.A. 1924. Theory of Rupture. In Proceedings of the First International Conference on Applied Mechanics, Delft, Holland, pp. 55-63.

Hallett, P.D., Dexter, A.R., & Seville, J.P.K. 1995. The application of fracture mechanics to crack propagation in dry soil. *European Journal of Soil Science*, 46: 591-599.

Heibrock, G. 1997. Desiccation cracking of mineral sealing liners. In Proceedings of the sixth International Landfill Symposium, Sardinia 97, Lining, Drainage and Stability in Landfills, pp. 101-114.

Heibrock, G., Zeh, R., & Witt, K.J. 2003. Tensile strength of compacted clays. In Proceedings of the International Conference -From Experimental Evidence towards Numerical Modelling of Unsaturated Soils, Weimar, Germany, Schanz Ed., vol. 1, pp. 395-412.

Hu, L.B., Peron, H., Hueckel, T. & Laloui, L. 2007. Drying shrinkage of deformable porous media: mechanisms induced by the fluid removal. In H.W. Olson (ed.), ASCE Geotechnical Special Publication 157: Geo-Denver 2007, New Peaks in Geotechnics. 10 pages, CD-ROM.

Hueckel, T. 1992. Water-mineral interaction in hygromechanics of clays exposed to environmental loads: a mixture-theory approach. *Canadian Geotechnical Journal*, 29: 1071-1086.

Hvorslev, M.J. 1937. "Ûber die Festigkeitseigenschafter gesstörter bindiger Böden," Ingvidensk Skr., A, No. 45 (English trans. No. 69-5, Waterways Experiment Station, Vicksburg, Miss. (1969).

Jaeger, J.C., & Cook, N.G.W. 1969. Fundamentals of Rock Mechanics. Methuen and Co Ltd, London.

Kim, T., & Hwang, C. 2003. Modelling of tensile strength on moist granular earth material at low water content. *Engineering Geology*, 69: 233-244.

Kodikara, J. K., & Choi, X. 2006. A simplified analytical model for desiccation cracking of clay layers in laboratory tests. Proc., 4th Int. Conf. on Unsaturated Soils, Geotechnical Special Publication 147, G. A. Miller, C. E. Zapata, S. L. Houston, and D. G. Fredlund, eds., Vol. 2, ASCE, Reston, VA, 2558–2567.

Krahn, J. & Fredlund, D.G. 1971. On total , matric and osmotic suction. *Soil Science*. 114, 5, 340-347.

Krishnayya, A.V.G., & Eisenstein, Z. 1974. Brazilian tensile test for soils, *Can. Geotech. J.*, Vol. 11, pp. 632–642.

Lachenbruch, A.H. 1961. Depth and spacing of tension cracks. *Journal of Geophysical research*, 66(12): 4273-4292.

Lima, L.A. & Grismer, M.E. 1994. Application of fracture mechanics to cracking of saline soils. *Soil Science,* 158(2):86-96.

Marinho, F.A.M. 1994. Shrinkage behaviour of some plastic soils. Ph.D. Thesis. The University of London.

Marsland, A. 1968. The shrinkage and fissuring of clay in flood banks. Building Research Station, Internal report No. 39/68.

Marsland, A. & Cooling, L.F. 1958. Tests on Full Scale Clay Flood Bank to Study Seepage and the Effects of Overtopping. Building Research Station, Internal report No. C562.

Miller, G. A., Hassanikhah, A., & Varsei, M. 2015. Desiccation crack depth and tensile strength in compacted soil. Unsaturated Soil Mechanics– From Theory to Practice: Proc., 6th Asia Pacific Conf. on Unsaturated Soils, CRC Press, Boca Raton, FL.

Mitchell, J.K., & Soga, K. 2005. Fundamentals of Soil Behavior. John Wiley and Sons.

Morris, PH., Graham, J. & Williams, DJ. 1992. Cracking in drying soil. *Can Geotech*, 29, 263–77.

Nahlawi, H., Chakrabarti, S., & Kodikara, J. 2004. A direct tensile strength Testing Method for unsaturated geomaterials. *Geotechnical Testing Journal*, 27(4): 356-361.

Nahlawi, H., & Kodikara J.K. 2006. Laboratory experiments on desiccation cracking of thin soil layers. *Geotechnical and Geological Engineering*. 24: 1641-1664

Park, J.W., Chang, K., & Kim, C.L. 2001.Numerical simulations of the moisture movement in unsaturated bentonite under a thermal gradient. *J. of Korean Nuclear Society* 33(1), 62–72

Prat, P.C., Ledesma, A., Lakshmikantha, M.R., Levatti, H.U., & Tapia, J. 2008. Fracture mechanics for crack propagation in drying soils. 12th International Conference of IACMAG, pp.106-1067.

Parry, R. H. G. 1960. Triaxial compression and extension tests on remoulded saturated clay. *Geotechnique*, 10, No. 4, 160–180.

Péron, H. 2008. Desiccation cracking of soils. Ph.D. Thesis. École Polytechnique Fédérale de Lausanne.

Péron, H., Delenne, J.Y., Laloui, L. & El Youssoufi, M.S. 2009. Discrete element modelling of drying shrinkage and cracking of soils. *Comput Geotech*, 36, (1–2), 61–69.

Péron, H., Laloui, L., Hu, L.B. & Hueckel, T. 2012. Formation of drying crack patterns in soils: a deterministic approach. *Acta Geotechnica*. DOI 10.1007/s11440-012-0184-5

Rice, J.R. 1967. A path independent integral and the approximate analysis of strain concentration by notches and cracks. *Journal of Applied Mechanics*, 35, pp. 379–386.

Rodriguez, R., Sanchez, M., Ledesma, A. & Lloret, A. 2007. Experimental and numerical analysis of desiccation of a mining waste. *Can Geotech J*, 44, No. 6. 644–658.

Saada, A.S., Chudnovsky, A., & Kennedy M.R. 1985. A fracture mechanics study of stiff clays. *In* Proceedings of the Eleventh International Conference on Soil Mechanics and Foundation Engineering, San Francisco, vol. 2, pp. 637-640.

Snyder, V.A., & Miller, R.D. 1985. Tensile strength of unsaturated soils. *Soil Science Society of America Journal*, 49: 58-65.

Stapledon, D.H. 1970. Changes and structural effects developed in some South Australian clays, and their engineering consequences. Proceedings of a symposium on soils and earth structures in arid climates, Adelaide, pp. 62-71.

Stirling, R.A., Hughes, P., Davie, C.T. & Glendinning, S. 2015. Tensile behaviour of unsaturated compacted clay soils – A direct assessment method. *Applied Clay Science,* 112-113, 123-133.

Tang, G.X., & Graham, J. 2000. A method for testing tensile strength in unsaturated soils. *Geotechnical Testing Journal*, 23(3): 377-382.

Tang, C.S., Shi, B., Liu, C., Suo, W.B. & Gao, L. 2011. Experimental characterization of shrinkage and desiccation cracking in thin clay layer. *Applied clay science*, 52, 69-77

Tarantino, A., Romero, E. & Cui, Y.J. 2005. Advanced Experimental Unsaturated Soil Mechanics. Proceeding of an international symposium on advanced experimental soil mechanics, Trento, Italy, 27-29 June 2005

Tarantino, A., Sacchet, A., Dal Maschio, R. & Francescon, F. 2010. A Hydromechanical Approach to Model Shrinkage of Air-Dried Green Bodies. *Journal of the American Ceramic Society*, 93, No. 3, 662–670.

Terzaghi, K. 1936. The Shearing Resistance of Saturated Soils and the Angle between the Planes of Shear; in Proceedings of the 1st International Conference on Soil Mechanics Foundation Engineering, vol.1, pp. 54–56.

Thusyanthan, N.I., Take, W.A., Madabhushi, S.P.G. & Bolton, M.D. 2007. Crack initiation in clay observed in beam bending. *Geotechnique,* 57, No. 7, 581–594

Trabelsi, H., Jamei, M., Zenzri, H., Guiras, H., Romero, E. & Olivella, S. 2010. Some investigations about the tensile strength and the desiccation process of unsaturated clay. EPJ Web of Conferences 6, 12005, DOI:10.1051/epjconf/20100612005.

Trabelsi, H., Jamei, M., Zenzri, H., & Olivella, S., 2012. Crack patterns in clayey soils: Experiments and modeling. *International Journal for Numerical and Analytical Methods in Geomechanics*. 36. . 10.1002/nag.1060.

Towner, G.D. 1988. The influence of sand and silt-size particles on the cracking during drying of small clay dominated aggregates. *Journal of Soil Science*, 39: 347-356.

Villar, L.F.S., Campos, T.M.P., Azevedo, R.F. & Zornberg, J.G. 2009. Tensile strength changes under drying and its correlations with total and matric suctions. Proceedings of the 17th International Conference on Soil Mechanics and Geotechnical Engineering.793-796.

Yavari, A., Sarkani, S. & Moyer, E.T. 2002. The mechanics of self-similar and self-affine fractal cracks. *International Journal of Fracture*, 114: 1–27, 2002.

8.2 Chapter 2 References

Ajaz, A. & Parry, R.H.G. 1975. Stress-strain behaviour of two compacted clays in tension and in compression. *Géotechnique*, Vol. 25, No. 3, pp. 495-512..

Blazejczak, D., Horn, R., & Pytka, J. 1995. Soil tensile strength as affected by time, water content and bulk density. *Int. Agrophysics*, Vol. 9, No. 3, pp. 179–188.

De Souza Villar, L.F., De Campos, T.M.P., Azevedo, R.F., & Zornberg, J.G. 2009. Tensile strength changes under drying and its correlations with total and matric suctions. *Proceedings of the 17th International Conference on Soil Mechanics and Geotechnical Engineering: The Academia and Practice of Geotechnical Engineering.* Vol. 1, pp. 793-796.

Farrell, D.A., Geacen, E.L., & Larson, W.E. 1967. The effect of water content on axial strain in a loam soil under tension and compression, *Soil Science Society of America Proceedings*, Vol. 31, No. 4, pp 445-450.

Frydman, S. 1964. The applicability of the Brazilian (indirect tension) test of soils. *Aust. J. Appl. Sci*., Vol. 15, pp 335–343.

Heibrock, G., Zeh, R., & Witt, K.J. 2003. Tensile strength of compacted clays. *In* Proceedings of the International Conference - From Experimental Evidence towards Numerical Modelling of Unsaturated Soils, Weimar, Germany, Schanz Ed., Vol. 1, pp. 395-412.

Jaeger, J.C., & Cook, N.G.W., 1969, Fundamentals of Rock Mechanics. Methuen and Co Ltd, London.

Kim, T.H., & Hwang, C., 2002. Modelling of tensile strength on moist granular earth material at low water content, *Engineering Geology*, Vol. 69, pp. 233-244.

Krishnayya, A.V.G., & Eisenstein, Z. 1974. Brazilian tensile test for soils. *Can. Geotech. J*., Vol. 11, pp. 632–642.

Nahlawi, H., Chakrabarti, S., & Kodikara, J. 2004. A direct tensile strength Testing Method for unsaturated geomaterials. *Geotechnical Testing Journal*, Vol. 27, No. 4, pp. 356-361.

Rodriguez, R.L. 2002. Estudio experimenntal de flujo y transporte de cromo, niquel y manganeso en resduos de la zona minera de Moa (Cuba): influencia del comportamiento hidromecanico. Ph.D. thesis, Universitat Politecnica de Catalunya – Barcelona Tech, Barcelona, Spain.

Rodriguez, R., Sanchez, M., Ledesma, A., & Lloret, A. 2007. Experimental and numerical analysis of desiccation of a mining waste. *Can Geotech J*, Vol. 44, No. 6, pp. 644–58.

Snyder, V.A. & Miller, R.D. 1985. A pneumatic fracture method for measuring the tensile strength of unsaturated soils. *Soil Science Society of America Journal*, Vol. 49, No. 6, pp. 1369-1374.

Stirling, R.A., Hughes, P.N., Davie, C.T., & Glendinning, S. 2015. Tensile behaviour of unsaturated compacted clay soils - A direct assessment method, *Applied clay science*., Vol. 112-113, pp. 123-133.

Tang, G.X. & Graham, J. 2000. A method for testing tensile strength in unsaturated soils", *Geotechnical Testing Journal*, Vol. 23, No. 3, pp. 377-382.

Thusyanthan, N.I., Take, W.A., Madabhushi, S.P.G., & Bolton, M.D., 2007. Crack initiation in clay observed in beam bending. *Geotechnique*, Vol. 57, No. 7, 2007, pp. 581–594.

Trabelsi, H., Jamei, M., Zenzri, H. & Olivella, S. 2011. Crack patterns in clayey soils: experiments and modelling. *Int J Numer Anal Meth Geomech*. Vol. 36, No. 11, pp. 1410–1433.

8.3 Chapter 3 References

Albrecht, B.A. & Benson, C.H. 2001. Effect of desiccation on compacted natural clay. *J Geotech Geoenviron Eng,* 127, No. 1, 67–75.

Amarasiri, A.L., Kodikara, J.K. & Costa, S. 2010. Numerical modelling of desiccation cracking. *Int J Numer Anal Methods Geomech*, 35, No. 1, 82–96.

Baker, R. 1981. Tensile strength, tension cracks and stability of slopes. *Soils and Foundations,* 21, No. 2, 1–17

Bowman, JR. 1926. Recent Factory Experience and Experiments in Drying Terra Cotta, *J. Am. Ceram. Soc*, 9, No. 6, 380–91.

Clews, H. 1969. Heavy Clay Technology. Academic Press, New York.

Cooper, A.R. 1978. Quantitative theory of cracking and warping during the drying of clay bodies. In Ceramic Processing Before Firing, GY Onoda and LL Hench (eds). John Wiley & Sons, New York.

Dyer, M.R. 2005. Further tests on fissuring of clay fill at the thorngumbald flood embankment. Proc. International symposium on advanced experimental unsaturated soil mechanics, Trento, Italy.

Haigh, S.K., Vardanega, P.J. & Bolton, M.D. 2013. The plastic limit of clays. *Geotechnique,* 63, No. 6, 435-440.

Head, K.H. 1986. Manual of Soil Laboratory Testing. Pentech Press, London.

Konrad, J-M. & Ayad, R. 1997. Desiccation of a sensitive clay: field experimental observations. *Can Geotech J*, 34, No. 6, 929–42.

Lakshmikantha, M.R., Prat, P.C. & Ledesma, A. 2012. Experimental evidence of size effect in soil cracking. *Canadian Geotechnical Journal*, 49, No. 3, 264-284.

Marsland, A. 1968. The shrinkage and fissuring of clay in flood banks. Building Research Station, Internal report No. 39/68.

Marsland, A. & Cooling, L.F. 1958. Tests on Full Scale Clay Flood Bank to Study Seepage and the Effects of Overtopping. Building Research Station, Internal report No. C562.

Morris, PH., Graham, J. & Williams, DJ. 1992. Cracking in drying soil. *Can Geotech*, 29, 263–77.

Péron H., Hu, L., Laloui, L. & Hueckel, T. 2007. Numerical and Experimental investigation of desiccation of soil;3:3–8.

Péron, H., Delenne, J.Y., Laloui, L. & El Youssoufi, M.S. 2009. Discrete element modelling of drying shrinkage and cracking of soils. *Comput Geotech*, 36, (1–2), 61–69.

Prat, P.C., Ledesma, A., Lakshmikantha, M.R., Levatti, H.U., & Tapia, J. 2008. Fracture mechanics for crack propagation in drying soils. 12th International Conference of IACMAG, pp.106-1067.

Rodriguez, R.L. 2002. Estudio experimenntal de flujo y transporte de cromo, niquel y manganeso en resduos de la zona minera de Moa (Cuba): influencia del comportamiento hidromecanico. Ph.D. thesis, Universitat Politecnica de Catalunya – Barcelona Tech, Barcelona, Spain.

Rodriguez, R., Sanchez, M., Ledesma, A. & Lloret, A. 2007. Experimental and numerical analysis of desiccation of a mining waste. *Can Geotech J*, 44, No. 6. 644–658.

Sánchez, M., Manzoli, O.L. & Guimarães, L.J.N. 2014. Modeling 3-D desiccation soil crack networks using a mesh fragmentation technique. *Comput Geotech*, 62, 27–39.

Shin, H. & Santamarina, JC. 2011. Desiccation cracks in saturated fine-grained soils: particle-level phenomena and effective-stress analysis. *Géotechnique,* 61, No. 11, 961–72.

Sima, J., Jiang, M. & Zhou, C. 2014. Numerical simulation of desiccation cracking in a thin clay layer using 3D discrete element modeling. *Comput Geotech*, 56, 168–80.

Tarantino, A. & Mongiovì, L. 2002. Design and construction of a tensiometer for direct measurement of matric suction. *Proceedings 3rd International Conference on Unsaturated Soils*. vol. 1. pp. 319-324. Edited by J.F.T. Jucá, T.M.P. de Campos and F.A.M. Marinho, Balkema, Rotterdam.

Tarantino, A. 2007. A possible critical state framework for unsaturated compacted soils. *Geotechnique,* 57, No. 4, 385-389.

Tarantino, A. 2009. A water retention model for deformable soils, *Géotechnique*, 59, No. 9, 751-762.

Tarantino, A., Sacchet, A., Dal Maschio, R. & Francescon, F. 2010. A Hydromechanical Approach to Model Shrinkage of Air-Dried Green Bodies. *Journal of the American Ceramic Society*, 93, No. 3, 662–670.

Tarantino, A. & El Mountassir, G. 2013. Making unsaturated soil mechanics accessible for engineers: preliminary hydraulic-mechanical characterisation and stability assessment. *Engineering Geology*, 165, 89-104.

Thusyanthan, N.I., Take, W.A., Madabhushi, S.P.G. & Bolton, M.D. 2007. Crack initiation in clay observed in beam bending. *Geotechnique,* 57, No. 7, 581–594

Vanapalli, S.K., Fredlund, D.G., Pufahl, D.E. & Clifton, A.W. 1996. Model for the prediction of shear strength with respect to soil suction. *Canadian Geotechnical Journal*, 33, No. 3, 379–392.

Varsei, M., Miller, G.A. & Hassanikhah, A., 2016. Novel Approach to Measuring Tensile Strength of Compacted Clayey Soil during Desiccation. *International Journal of Geomechanics*, 16, No. 6.

8.4 Chapter 4 References

Albrecht, B.A. & Benson, C.H. 2001. Effect of desiccation on compacted natural clay. J Geotech Geoenviron Eng, 127, No. 1, 67–75.

Alonso, E.E., Gens, A. & Josa, A. 1990. A constitutive model for partially saturated soils. Géotechnique, 40: 405-430.

Amarasiri, A.L. & Kodikara, J.K. 2013. Numerical modelling of desiccation cracking using the cohesive crack method. Int. J. Geomech. 13, No. 3 213-221.

Amarasiri, A.L., Shannon, B. & Kodikara, J.K. 2014. Numerical modelling of desiccation in a restrained ring test. Can. Geotech. J. 51. 67-76.

Ávila, G., Ledesma A. & Lloret A. 2013. One-dimensional cracking model in clayey soils. Proceedings of the 18th International Conference on Soil Mechanics and Geotechnical Engineering, Paris. 1077-1080.

Collin F., Li, X.L., Radu, J.P. and Charlier, R. 2002. Thermo-hydro-mechanical coupling in clay barriers. Engineering Geology, 64: 179-193.

Cooper, A.R. 1978. Quantitative theory of cracking and warping during the drying of clay bodies. In Ceramic Processing Before Firing, GY Onoda and LL Hench (eds). John Wiley & Sons, New York.

Costa, S., Kodikara, J., Thusyanthan, N.I. 2008. Modelling of desiccation crack development in clay soils. In: Proc. 12th International Conference of IACMAG, Goa, India, pp. 1099–1107.

Decagon Devices, 2014. WP4C Dew point Potentiameter, s.l.: s.n.

Dyer, M.R. 2005. Further tests on fissuring of clay fill at the thorngumbald flood embankment. Proc. International symposium on advanced experimental unsaturated soil mechanics, Trento, Italy.

Gerard, P., Charlier, R., Barnichon, J.D., Su, K., Shao, J.F., Duveau, G., Giot, R., Chavant, C. & Collin, F. 2008. Numerical modelling of coupled mechanics and gas transfer around radioactive waste in long-term storage. J. Theor. Appl. Mech. 38(1-2), 25–44.

Hallet, P. & Newson, T. 2001. A simple fracture mechanics approach for assessing ductile crack growth in soil. Soil Sci Soc Am J. 65, 1083-1088.

Heibrock, G., Zeh, R., and Witt, K.J., 2003. Tensile strength of compacted clays. In Proceedings of the International Conference - From Experimental Evidence towards Numerical Modelling of Unsaturated Soils, Weimar, Germany, Schanz Ed., Vol. 1, pp. 395-412.

Konrad, J-M. & Ayad, R. 1997. Desiccation of a sensitive clay: field experimental observations. Can Geotech J, 34, No. 6, 929–42.

Lakshmikantha, M.R., Prat, P.C. & Ledesma, A. 2012. Experimental evidence of size effect in soil cracking. Canadian Geotechnical Journal, 49, No. 3, 264-284.

Lloret, A., Ledesma, A., Rodriguez, R., Sanchez, M., Olivella, S. & Suriol, J. 1998. Crack initiation in drying soils. Proceeeding of the 2nd international conference on unsaturated soil, P.R. of China, vol. 1. Peking: International Academic Publishers.

Marinho, F. A., Take, A. & Tarantino, A. 2008. Tensiometric and axis translation techniques for suction measurement. Geotechnical and Geological Engineering, 26(6), pp. 615-631.

Marsland, A. 1968. The shrinkage and fissuring of clay in flood banks. Building Research Station, Internal report No. 39/68.

Marsland, A. & Cooling, L.F. 1958. Tests on Full Scale Clay Flood Bank to Study Seepage and the Effects of Overtopping. Building Research Station, Internal report No. C562.

Morris, PH., Graham, J. & Williams, DJ. (1992). Cracking in drying soil. Can Geotech, 29, 263–77.

Mohammadnejad, T. & Khoei, A.R. 2012. Hydro-mechanical modeling of cohesive crack propagation in multiphase porous media using the extended finite element method. Numerical and analytical methods in geomechanics. 37, No. 10, 1247–1279.

Murray, I., Tarantino, A, Gérard, P. & Francescon, F. 2014. Desiccation cracking in clay forms subjected to non-uniform hydraulic and mechanical boundary conditions. in N Khalili, A Russell & A Khoshghalb (eds), Unsaturated Soils: Research & Applications. vol. 1, Leiden, pp. 829-834, 6th International Conference on Unsaturated Soils, Sydney, Australia, 2-4 July.

Nahlawi, H., Chakrabarti, S., & Kodikara, J. 2004. A direct tensile strength Testing Method for unsaturated geomaterials. Geotechnical Testing Journal, Vol. 27, No. 4, pp. 356-361.

Peron, H., Hueckel, L., Laloui, L. & Hu, L.B. 2009. Fundamentals of desiccation cracking of fine grained soils: experimental characterisation and mechanisms identification. Can. Geotech. J. 45, 1177-1201.

Peron, H., Laloui, L., Hueckel, L. & Hu, L. 2006. Experimental study of desiccation of soil. Geotechnical Special Publication No. 147, Unsaturated Soils Vol. 1, ASCE publications, 1073-1084.

Rodriguez, R., Sanchez, M., Ledesma, A. & Lloret, A. 2007. Experimental and numerical analysis of desiccation of a mining waste. *Can Geotech J*, 44, No. 6. 644–658.

Sánchez, M., Manzoli, O.L. & Guimarães, L.J.N. 2014. Modeling 3-D desiccation soil crack networks using a mesh fragmentation technique. Comput Geotech, 62, 27–39.

Shin, H. & Santamarina, JC. 2011. Desiccation cracks in saturated fine-grained soils: particle-level phenomena and effective-stress analysis. Géotechnique, 61, No. 11, 961–72.

Stirling, R.A., Hughes, P.N., Davie, C.T., & Glendinning, S. 2015. Tensile behaviour of unsaturated compacted clay soils - A direct assessment method, Applied clay science., Vol. 112-113, pp. 123-133.

Tang C., Shi B., Liu C., Sho W., Gao L. 2011. Experimetanl characterization of shrinkage and desiccation cracking in thin clay layer. Appl. Clay Sci., 52, pp. 69-7.

Tarantino, A. & Mongiovi, L. 2002. Design and construction of a tensiometer for direct measurement of matric suction. Proceedings 3rd International Conference on Unsaturated Soils, pp. 319-324.

Tarantino, A., 2004. Panel report: Direct measurement of soil water tension. Proceedings 3rd International Conference on Unsaturated Soils, pp. 1005-1017.

Tarantino, A., Sacchet, A., Dal Maschio, R. & Francescon, F. 2010. A Hydromechanical Approach to Model Shrinkage of Air-Dried Green Bodies. Journal of the American Ceramic Society, 93, No. 3, 662–670.

Thusyanthan, N.I., Take, W.A., Madabhushi, S.P.G. & Bolton, M.D. 2007. Crack initiation in clay observed in beam bending. Geotechnique, 57, No. 7, 581–594.

van Genuchten, M., 1980. A closed-form equation for predicting the hydraulic conductivity of unsaturated soils. Soil Science Society of America Journal, Issue 44, pp. 892-898.

Yesiller, N., Miller, C.J., Inci, G. & Yaldo, K. 2000. Desiccation and cracking behaviour of three compacted landfill liner soils. Eng Geol. 57, 105-121.

8.5 Chapter 5 References

Baroghel-Bouny, V., Mainguy, M. & Coussy, O. 2001. Isothermal drying process in weakly permeable cementitious materials - Assessment of water permeability. Materials Science of Concrete Special Volume: Ion and Mass Transport in Cement-Based Materials, pp. 59-80.

Biot, M.A. 1941. General theory of three-dimensional consoidation. *Journal of Applied Physics*, Volume 12, pp. 155-164.

Bowman, J. 1926. Recent factory experience and experiments in drying terra cotta. *Journal of the American Ceramics Society*, 9(6), pp. 380-91.

BS: 1377-Part 2, 1990, British standard methods of test for soil for engineering purposes: classification tests, BSI, London

Clausen, J. & Fish, R., 1994. Successfully drying sanitaryware. Westerville, Ohio, *The American Ceramic Society*.

Coussy, O., 2004. Poromechanics. West Sussex: Wiley.

Decagon Devices, 2014. WP4C Dew point Potentiameter, s.l.: s.n.

Diamond, S. 1970. Pore size distributions in clay. *Clay and clay minerals*, Volume 18, pp. 7-23.

Ford, R., 1986. Ceramics drying. Oxford: Pergamon.

Fraser, H., 1986. Ceramic faults and their remedies. London: A & C Black.

Fredlund, D.G. & Rahardjo, H. 1993. Soil Mechanics for Unsaturated Soils. s.l.:John Wiley & Sons.

Gur'yanov, A.I. & Zakharov, A.I., 2007. Crack formation in a clay semifinished product. *Glass and Ceramics*, Volume 64, pp. 58-62.

Lu, N. & Likos, W.J., 2004. Unsaturated soil mechanics. Hoboken, N.J.: John WIley & Sons.

Marinho, F.A., Take, A. & Tarantino, A., 2008. Tensiometric and axis translation techniques for suction measurement. *Geotechnical and Geological Engineering*, 26(6), pp. 615-631.

Mitchell, J.K. 1993. Fundamentals of Soil Behavior. New York: Wiley Inter-Science.

Pedrotti, M. 2016. An experimental investigation on the micromechanics of non-active clays in saturated and partially-saturated states. Ph.D. Thesis, University of Strathclyde, Glasgow, Scotland, UK.

Reed, J. S., 1988. Introduction to the Principles of Ceramic Processing. New York: John Wiley & Sons.

Scherer, G.W. 1990. Theory of Drying. *Journal of the American Ceramics Society*, 73(1), pp. 3-14.

Sokolov, P.V. & Gak, B.N., 1959. Accelerating the drying of sanitary ware. *Glass Ceramics*, 16(10), pp. 561-565.

Tarantino, A. 2004. Panel report: Direct measurement of soil water tension. Proceedings 3rd International Conference on Unsaturated Soils, pp. 1005-1017.

Tarantino, A. & De Col, E. 2008. Compaction behaviour of clay. *Géotechnique*, 58(3), pp. 199-213.

Tarantino, A. & Mongiovi, L. 2002. Design and construction of a tensiometer for direct measurement of matric suction. Proceedings 3rd International Conference on Unsaturated Soils, pp. 319-324.

Tarantino, A., Sacchet, A., Dal Maschio, R. & Francescon, F. 2010. A hydro-mechanical approach to model shrinkage of air-dried green bodies. *Journal of the American Ceramic Society*, 93(3), pp. 662-670.

van Genuchten, M., 1980. A closed-form equation for predicting the hydraulic conductivity of unsaturated soils. *Soil Science Society of America Journal*, Issue 44, pp. 892-898.

Zhu, Y. & Leak, N., 2017. Drying processes - The balance between efficiency and product quality, s.l.: Lucideon.

9 LIST OF CAPTIONS FOR FIGURES AND TABLES

10 APPENDIX A – FULL HEIGHT CYLINDER TEST

The cylinder test was designed for two reasons:

1. As an alternative option to the double T test described in Chapter 4 for modelling the time of cracking in a drying clay specimen.
2. As a simple to run test for assessing the susceptibility to cracking of a material for use in the ceramics industry.

The cylinder test consists of a hollow cylindrical specimen that has been cast around a Teflon bar. The sample is left to evaporate. In a free shrinkage test this evaporation would cause the diameter of the cylinder to reduce. In the test, this shrinkage is prevented by the presence of a Teflon bar. The restrained shrinkage result in circumferential stresses developing within the sample, which can result in cracking.

An assumption is made that during evaporation the specimen is able to shrink freely in a vertical direction due to the low friction nature of the Teflon material comprising the cylindrical restraint.

The basic test is similar to that of Najm et al. (2009) (Figure A1-1) and Amarisiri et al. (2014), where a cylindrical soil specimen, of significantly greater thickness than the tests reported here, was formed around a steel restraint and desiccation allowed by evaporation through the top surface. The thickness of the specimen used in these tests makes it incompatible with the production methods used in the ceramic industry, and so, the test was redesigned. The specimes used here were either 5mm or 10mm in thickness. The internal diameter of the cylinders was 55mm.

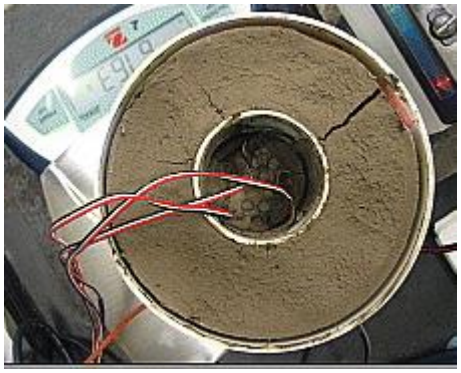

Figure A1-10-1 Test of Najm et al. (2009)

Material Properties

Two basic materials were used for the experiments, Vitreous China (VC) and Fine Fireclay (FFC). The relationship between void ratio and moisture content and degree of saturation and suction are shown in Figure A1-10-2 and Figure A1-10-3 for VC and Figure A1-10-4 and Figure A1-10-5 for the FFC. The liquid and plastic limit for the VC was 22.8% and 16.6% respectively, and 18.3% and 12.90% for the FFC.

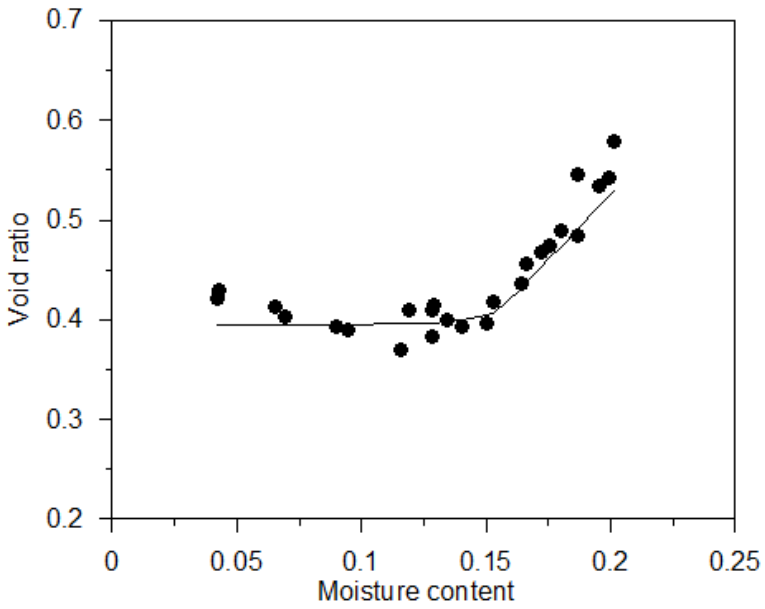

Figure A1-10-2 Bigot curve for VC

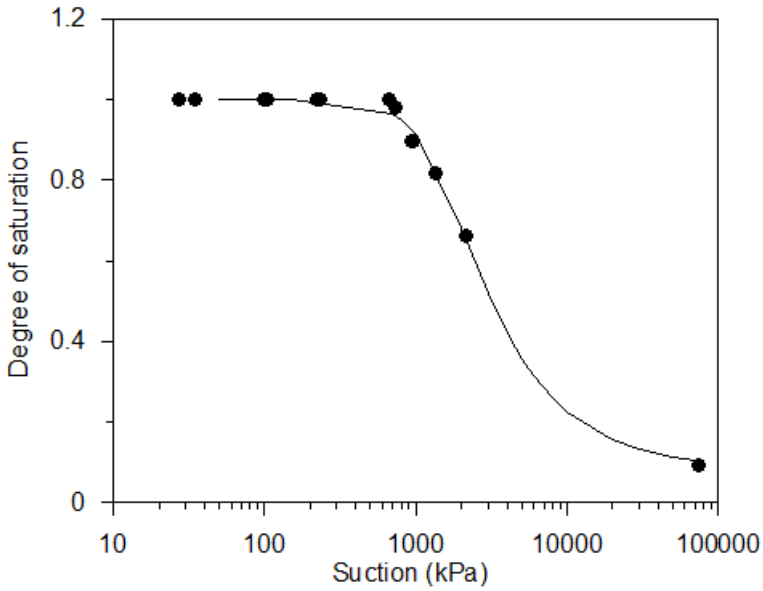

Figure A1-10-3 Drying curve for VC

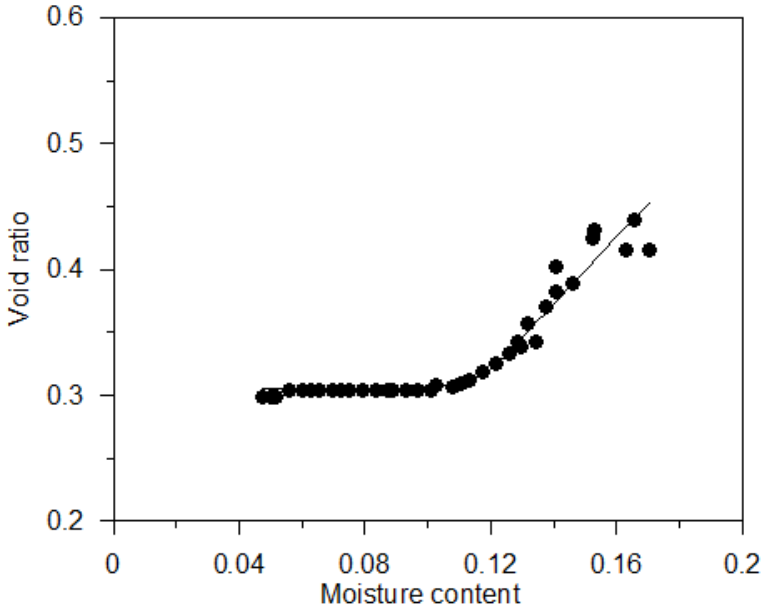

Figure A1-10-4 Bigot curve for FFC

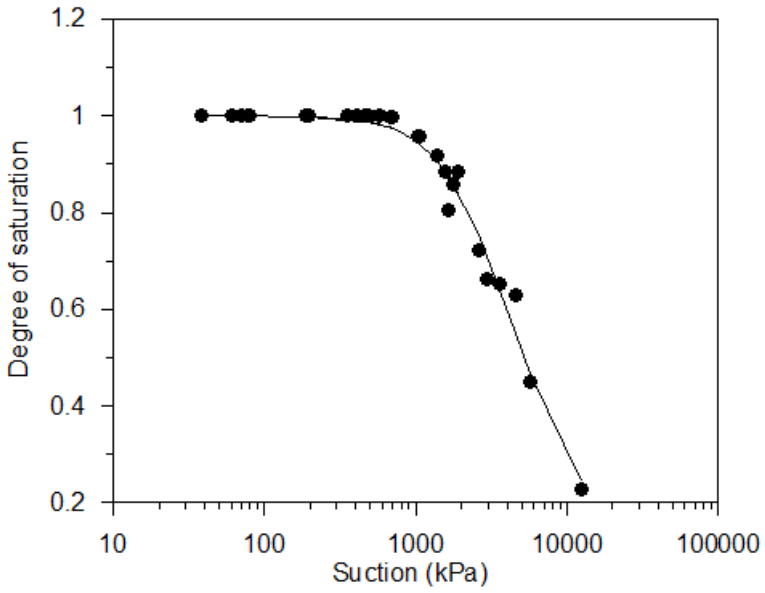

Figure A1-10-5 Drying curve for FFC

Specimen Preparation

The specimen was prepared using slip casting with plaster moulds. The basic slip for both materials was prepared by mixing the raw ingredients with de-mineralised water to a moisture content of approximately 32% for VC and 26% for FFC to create a large quantity of slip. This slip was then stored in an airtight container. For the creation of individual specimens, small quantities of this slip were taken, and de-mineralized water added to take the density of the slip to that required for casting (1.84kg/litre ≈ moisture content of 35% for VC and 1.94kg/litre ≈ moisture content of 29% for FFC). This slip was then poured into the mould.

The 5mm mould, shown in Figure A1-10-6, and 10mm mould were two-part splitting moulds, designed to hold the internal Teflon restraint in the centre at the base and leave a 5mm or 10m gap between the Teflon and the plaster for the rest of the moulds height. The slip was poured from the top into the gap between the Teflon and the plaster mould. Drying of the slip occurred only in the outward radial direction, into the plaster mould. By casting the sample

around the Teflon bar it is guaranteed that the inside of the cylinder is in contact with the Teflon bar and that there is no period of free shrinkage at the beginning of the test. This also negates the need for handling while sliding the sample over the Teflon bar which could result in damage, which may affect test results being caused to samples.

The time required for the slip to consolidate in the mould and create a plastic specimen was 90 minutes and 180 minutes for the 5mm and 10mm cylinders respectively.

The mould created a cylinder of approximately 130mm in height. Once removed from the mould the excess was cut from the top and bottom of the cylinder to create a cylinder with final height of approximately 100mm. If there were any defects in the cast cylinder the defects would be cut away, creating a cylinder with a height that is smaller than 100mm. The cylinder was then vacuum packed and stored for a period of 24hrs to allow for an equilibrium of water content throughout the specimen.

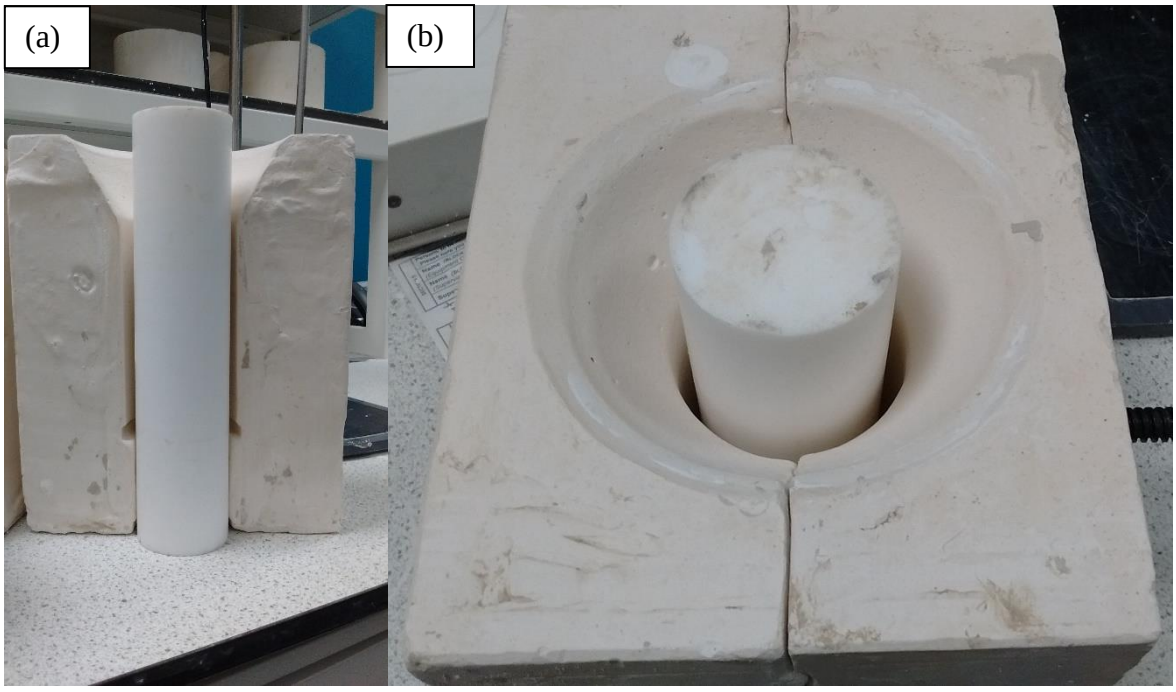

Figure A1-10-6 Mould for slip casting of 5mm cylinder

5 and 10mm Cylinder Procedure and Equipment

The test procedures for both the 5mm and 10mm thickness cylinders were the same. The specimen was removed from storage and a layer of petroleum jelly applied to the top and bottom faces of the sample. This significantly reduced the rate of evaporation from the top and bottom faces, effectively meaning evaporation could only occur from the radial face of the cylinder. The weight of the petroleum jelly used was recorded. Before the test was started the sample was checked to identify if there was any damage. This included small cracks and pin holes which would result in the sample cracking sooner than a non-defective sample. Any sample with visible defects was discarded.

The sample was placed onto a balance to record the change in mass, caused by evaporation of water, over the period of testing (Figure A1-10-7). The sample was left until the sample either developed a crack or reached hygroscopic water content. During testing the sample was surrounded by three webcameras, allowing visibility of the whole specimen, that were recording timelapse videos to allow for identification of the cracking time. The relative humidity of the environment was also recorded. At the end of the test the sample was weighed, after removing the petroleum jelly, and placed into an oven to allow determination of its final water content. The data recorded by the balance allowed for back calculation, with the mass of the Vaseline and Teflon bar deducted, of the water content of the sample throughout the test and most importantly at the time of cracking.

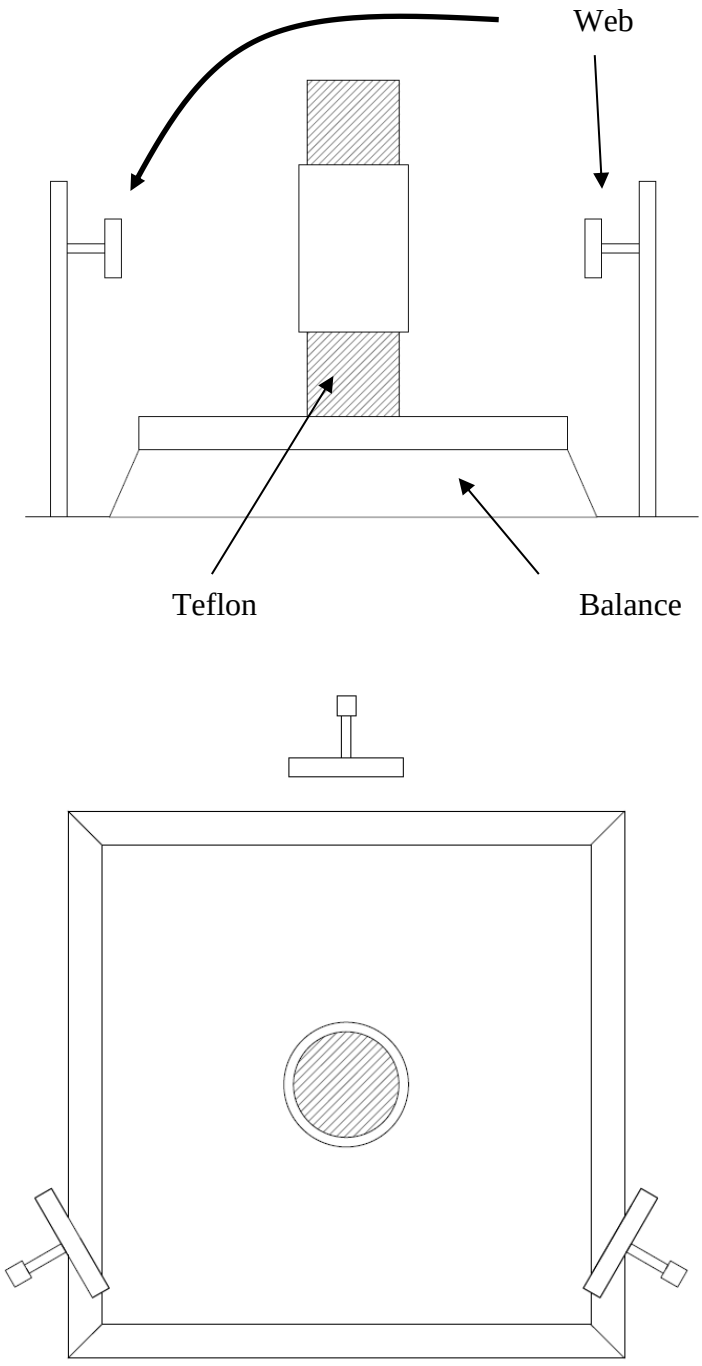

Figure A1-10-7 Apparatus for cylinder test

Results – Description of Cracks

Figure A1-10-8a and b show images of the crack formation from the 18-03 5mm VC cylinder test. The crack formation from this test was typical of those from the other tests that

cracked. Crack initiation always occurred at either the top or bottom of the cylinder and propagated vertically until it split the cylinder. Typically, the time taken form crack initiation to it spanning the entire height of the cylinder was less than 10 minutes.

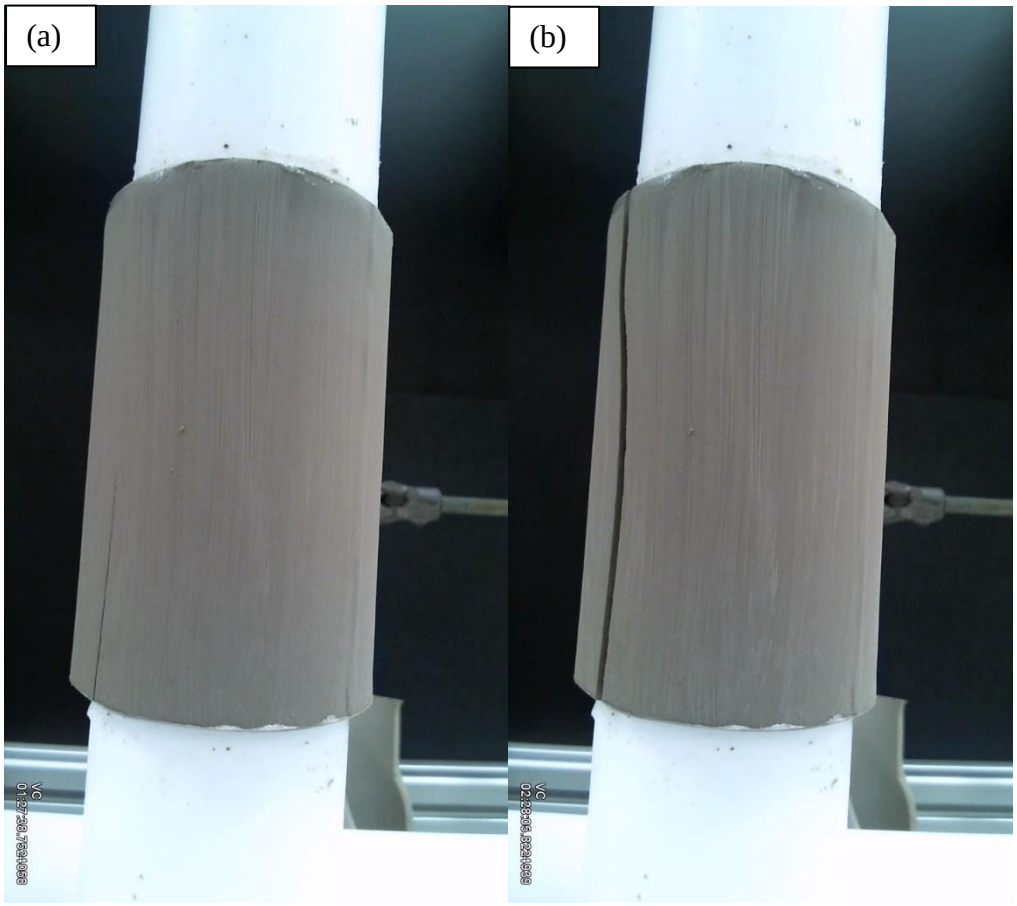

Figure A1-10-8 Images of crack from 5mm VC cylinder test. (a) Crack initiation (b) Full crack propagation

5mm VC

The results of the 5mm VC cylinder tests are shown in Table A1-10-1, Figure A1-10-9 and Figure A1-10-10 below. 12 tests were performed, of which 11 cracked. The height of the specimen ranges between 84 and 108mm. The record of the heights for the tests from 03 May onwards have been lost, but were within this range. The test on 05 May has been marked as bad

data due to unusual data from the balance giving unrealistic values for the water content.

The cracks occurred at water contents between 16.57 and 15.42%, which can be considered to be in the region of the air entry/plastic limit for the material. VC cylinders tests were performed at different relative humidities, which had a strong influence on the time when cracking occurred. The relationship between relative humidity and time to crack is shown in Figure A1-10-10. The figure shows that increasing the relative humidity from 40% to 60% has a small impact on the crack time, but a similar increase from 60 to 80% results in a near 6-fold increase in crack time.

From Figure A1-10-9 it may also be said that the slower rate of drying caused by an increased relative humidity, also affected the moisture content at cracking. Tests where the time to crack was greatest generally had the lowest moisture content at crack. This is most likely due to there being a smaller gradient in moisture content between the outer and inner face of the cylinder.

Table A1-10-1 Results of 5mm VC tests

Date	Sample Height (mm)	R.H. %	w_{t0}	Crack Time (minutes)	w_{crack}	Δw
18-Mar	108	45	18.99	86	16.01	2.98
26-Mar	108	38	18.7	80	15.63	3.07
28-Mar	108	40	18.8	82	15.65	3.15
31-Mar	98	42	18.63	86	15.56	3.07
10-Apr	106	42	19.44	86	16.23	3.21
01-May	84	80	20.18	618	15.42	4.76
03-May	-	60	18.47	322	15.49	2.98
05-May	-	70	Bad data	342	Bad data	
28-May	-	56	19.49	117	16.57	2.92
31-May	-	45 - 60	19.04	**No crack**	**No crack**	
02-Jun	-	61	18.9	120	16.37	2.52
05-Jun	-	58	19.5	123	16.45	3.09

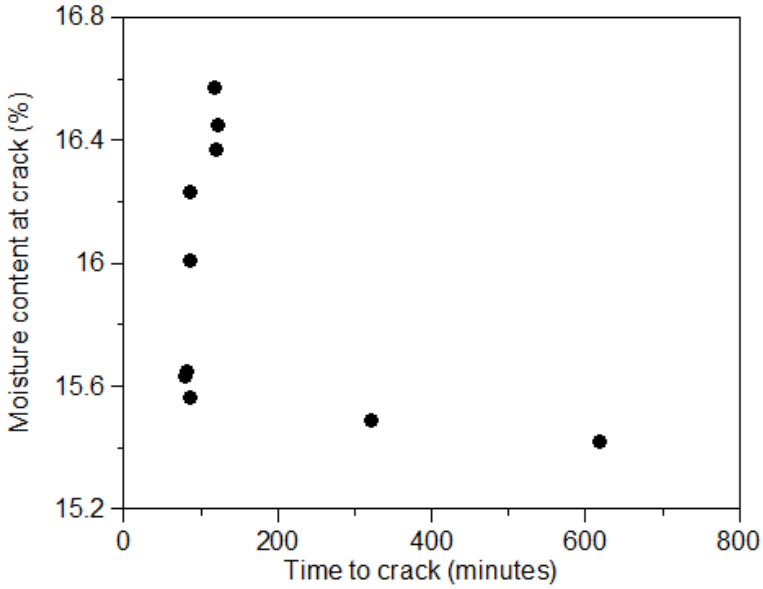

Figure A1-10-9 Moisture content at time of cracking against time of cracking for 5mm VC cylinder tests

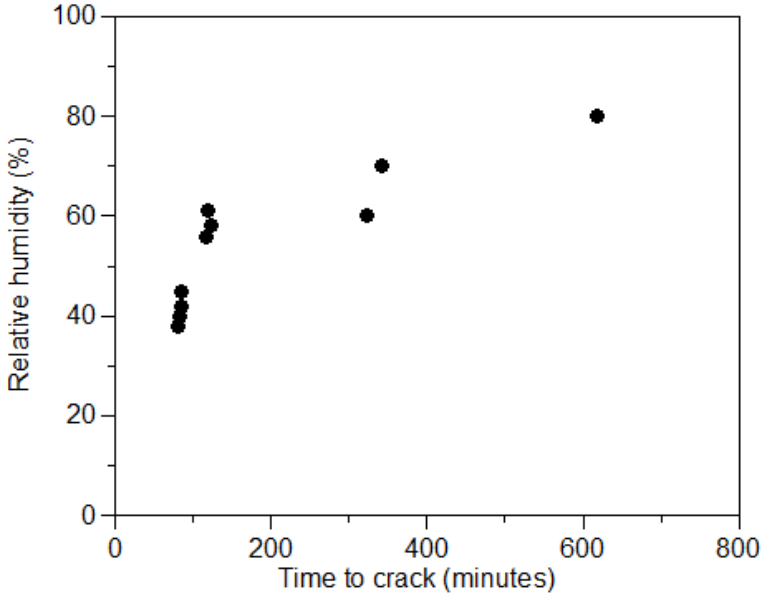

Figure A1-10-10 Relationship between relative humidity and time of cracking for 5mm VC cylinder tests

10mm VC

The results of the 4 tests performed with VC using a 10mm thick cylinder are shown in

Table A1-10-2, Figure A1-10-11 and Figure A1-10-12. In general, the time to cracking for a 10mm thick specimen, at a similar relative humidity, is longer than for the 5mm test. In addition, the water contents at time of cracking are higher than in the 5mm specimens.

Table A1-10-2 Results of10mm VC tests

Date	Sample Height (mm)	R.H. %	w_{t0}	Crack Time (minutes)	w_{crack}	Δw
23-May	-	39	20.32	166	17.17	3.15
24-May	-	46	20.68	221	16.92	3.76
26-May	-	54	21.36	294	17.21	4.15
04-Jun	-	52	20.16	311	15.82	4.34

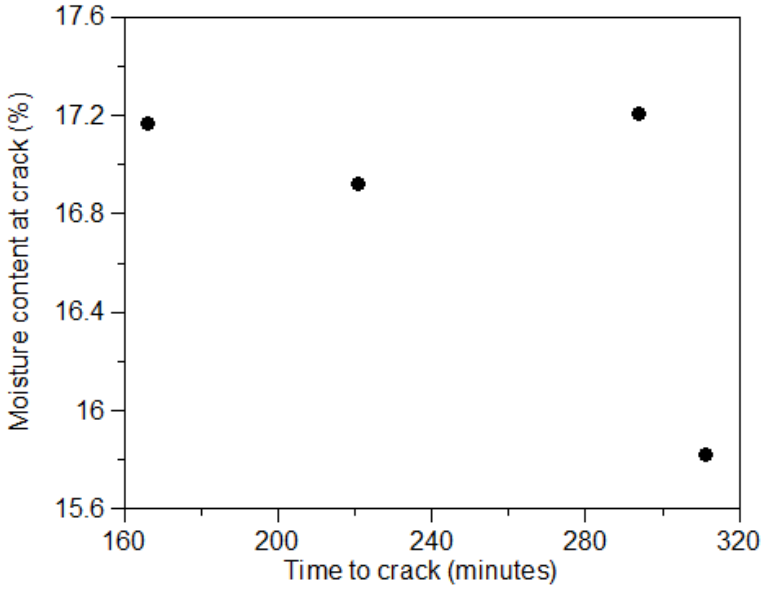

Figure A1-10-11 Moisture content at time of cracking against time of cracking for 10mm VC cylinder tests

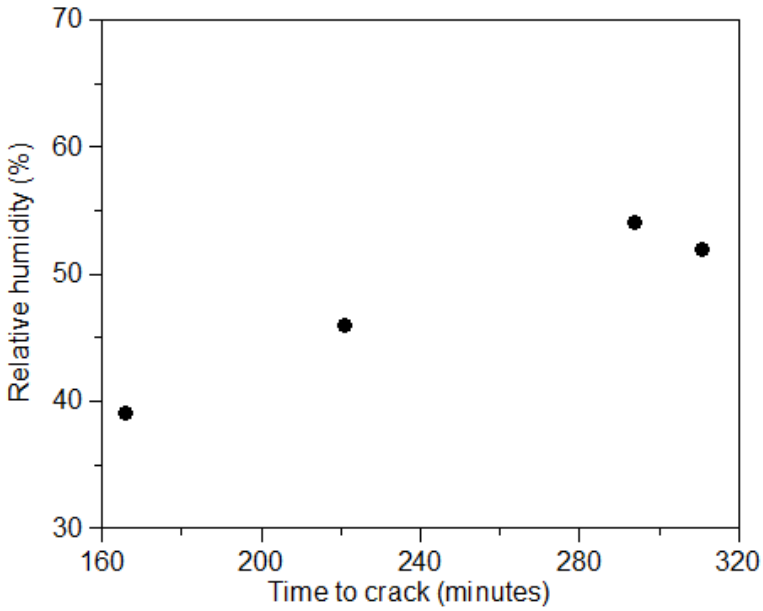

Figure A1-10-12 Relationship between relative humidity and time of cracking for 10mm VC cylinder tests

5mm FFC

The results of the tests on 5mm thick FFC specimens are shown in Table A1-3 and Figures A1-13 and A1-14. A total of ten tests were performed, of which 3 did not crack and a further 2 cracked but only after drying had stopped and the specimens were at the hygroscopic water content. A reasonable explanation for the cracks that occurred in these 2 tests has not been hypothesised, but it is considered reasonable to consider these two tests alongside those that did not crack, as whatever the method of cracking occurred it is clearly different from the cracks that have occurred around the air entry/plastic limit.

Table A1-10-3 Results of 5mm FFC tests

Date	Sample Height (mm)	R.H. %	w_{t0}	Crack Time (minutes)	w_{crack}	Δw
24-Apr	99	43	14.84	141	10.55	4.29
25-Apr	99	44	15.06	137	11.37	3.69
26-Apr	101	48	14.77	1278	0.84	13.93
28-Apr	92	50	14.76	**No crack**	**No crack**	
07-May	92	46	15.1	**No crack**	**No crack**	
09-May	92	46	15.1	68	12.89	2.21
10-May	91	50	14.8	**No crack**	**No crack**	
12-May	-	41	14.7	1424	0.57	14.13
21-May	92	46	15.26	93	12.68	2.58
30-May	-	73	14.12	596	12.12	2

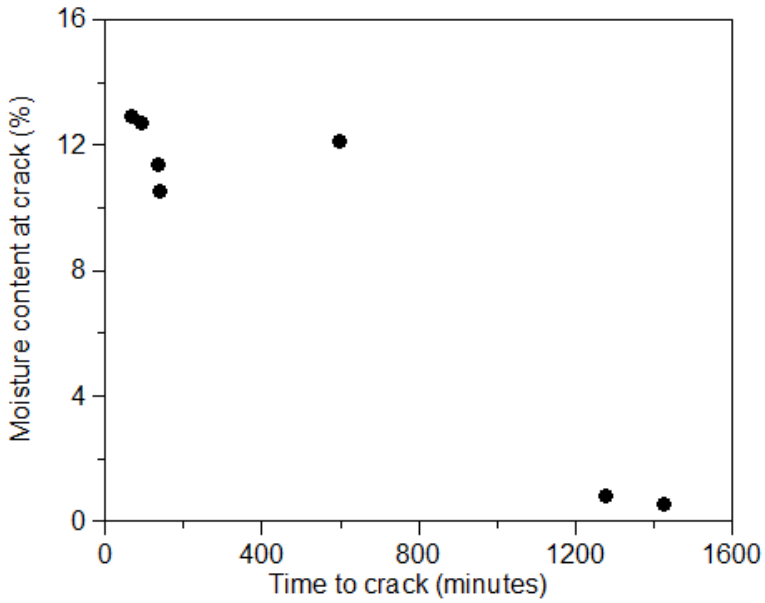

Figure A1-10-13 Moisture content at time of cracking against time of cracking for 5mm FFC cylinder tests

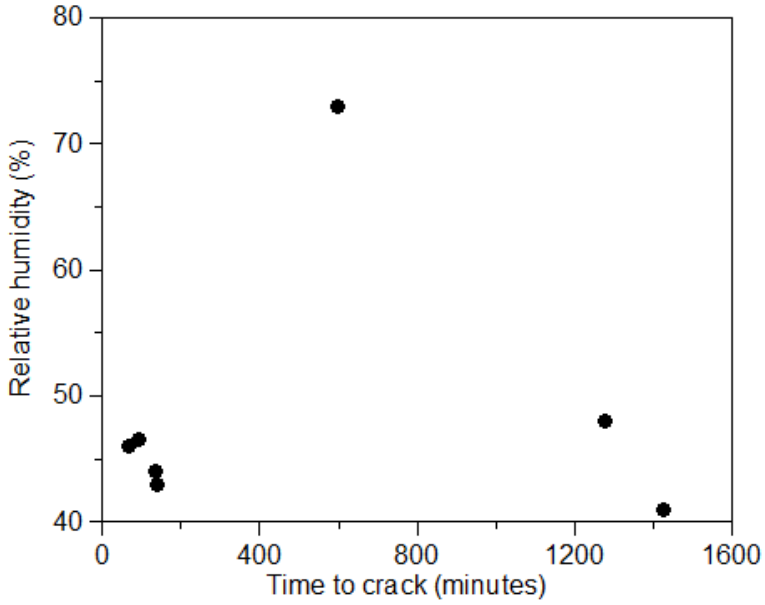

Figure A1-10-14 Relationship between relative humidity and time of cracking for 5mm FFC cylinder tests

10mm FFC

Only two tests of 10mm FFC were conducted making it difficult to observe any significant trends from the data. The data from the tests in shown in Table A1-10-4, Figure A1-10-15 and Figure A1-10-16. The cracks from the two tests did however occur at a moisture content close to the plastic limit/air entry value for the material, as in the 5mm FFC tests.

Table A1-10-4 Results of 10mm FFC tests

Date	Sample Height (mm)	R.H. %	w_{t0}	Crack Time (minutes)	w_{crack}	Δw
25-May	100	52	16.16	432	10.72	5.44
28-May	92	52	16.34	540	9.21	7.13

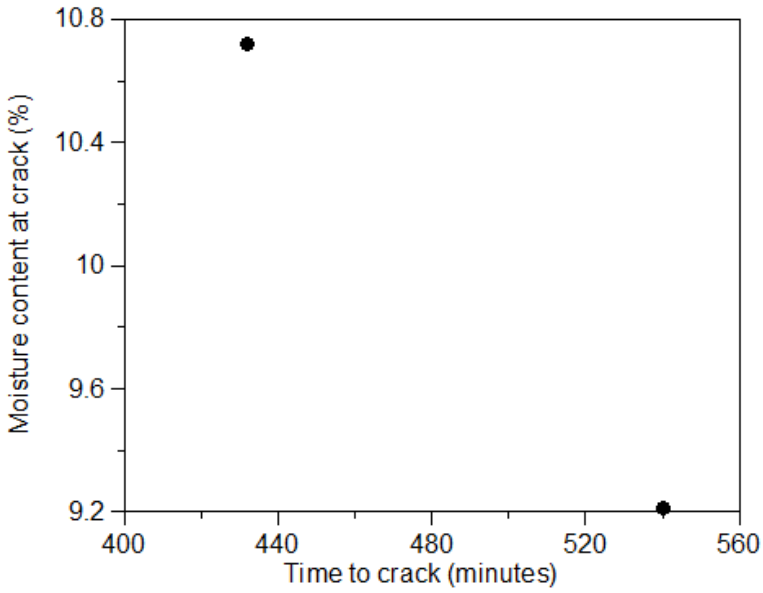

Figure A1-10-15 Moisture content at time of cracking against time of cracking for 10mm FFC cylinder tests

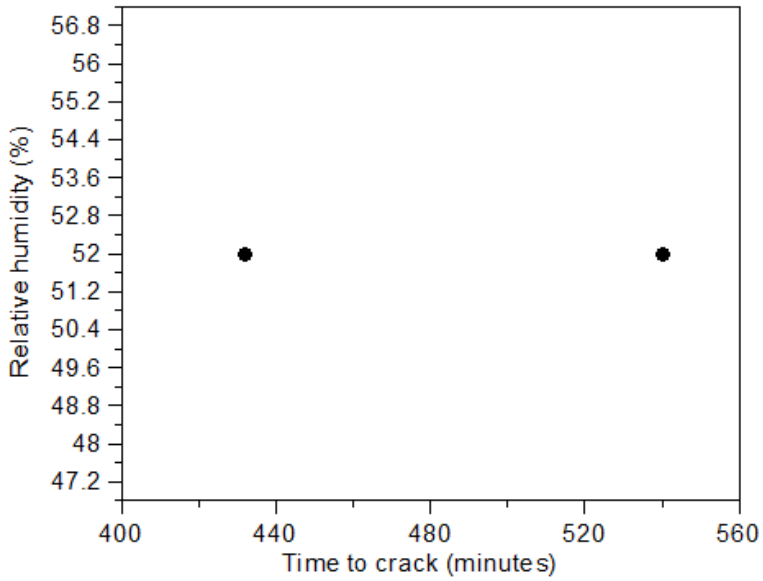

Figure A1-10-16 Relationship between relative humidity and time of cracking for 10mm FFC cylinder tests

Discussion

The results from the 5mm tests show that the VC material is more susceptible to cracking,

with 10 of 11 tests cracking, compared to 7 of 10 for the FFC material, of which 2 cracked at the end of the test at the hygroscopic water content.

A conclusion on the susceptibility of each material to cracking cannot be extended from the 10mm tests cannot because an insufficient number of tests were performed on each material. However, it may be said that a 10mm cylinder is more likely to cause cracking than a 5mm test as all 6 tests (4 VC and 2 FFC) resulted in cracks.

For the 5mm tests the cracks occurred within a small range of the plastic limit for the respective material and within a moisture content of 1% greater than air entry. For the 10mm VC cylinders the cracks occurred at a higher moisture content than in the 5mm tests, whereas for the FFC cracking occurred at lower moisture contents in the 10mm tests than the 5mm tests.

It can be said that cracking in all cases, with the exception of the two 5mm FFC tests where cracking occurred at the end of drying, that cracking occurred within a small range of the air entry, as has often been presented in the literature for other desiccation cracking tests.

References

Amirasiri, A., Shannon, B. & Kodikara, J. 2014. Numerical modelling of desiccation cracking in a restrained ring test. *Can. Geotech. J.*, 51, 67–76

Najm, M.A., Mohtar, R.H, Weiss, J. & Braudeau. E. 2009. Assessing internal stress evolution in unsaturated soils. *Water Resources Research*, 45, 1-18

11 APPENDIX B - CYLINDER RINGS TEST

The "cylinder rings" test, a variation on the full height cylinder test, was run to provide further evidence of cavitation as influencing crack initiation. This was brought about after observing the main tensile tests not reaching the shear failure envelope for specimens tested with suctions close to the materials air entry value (Chapter 3). The test was a method of collecting data more quickly than the tensile test, on the effect that de-airing the slip prior to casting would have on cracking.

Materials

Mixes of both VC and FFC were used for crating specimens for these tests. The VC and FFC materials used for these tests was the same batch of material as was used for the tests in Chapter 5. Details of the specimen characterisation methodology, which was the same for both materials, can be found in Chapter 5. For convenience the relationship between void ratio and moisture content and between degree of saturation and suction are shown in Figure A2-11-1 and Figure A2-. The plastic limit of the two materials were tested on both non-de-aired and de-aired material. The non de-aired plastic limits were taken as 18.1% and 16.44% for the VC and FFC respectively, and the de-aired plastic limits were 17.6% and 16.2%.

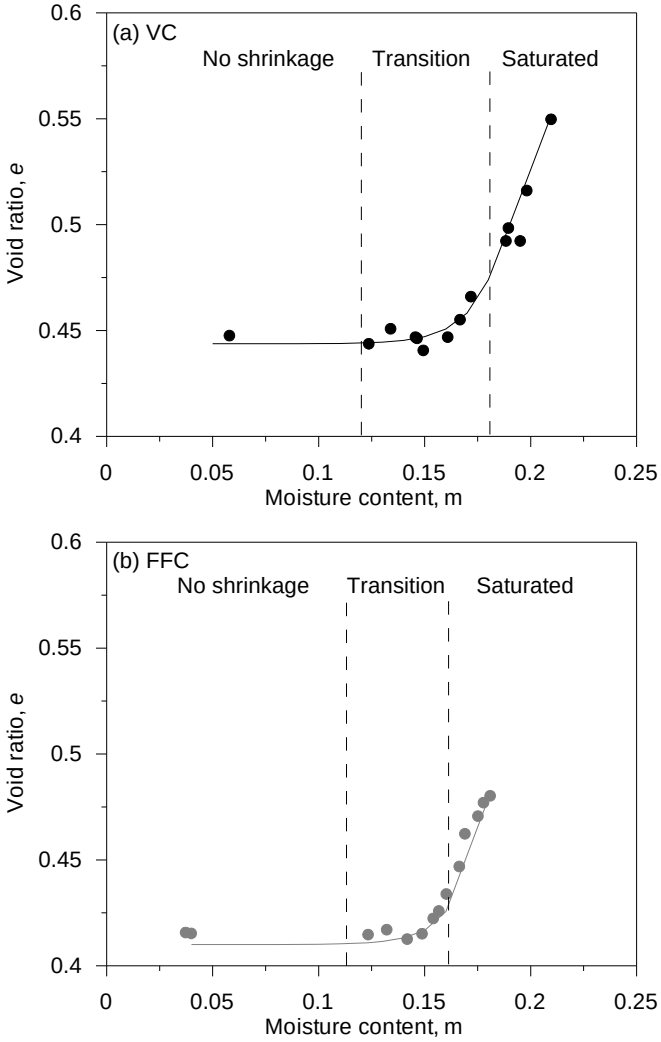

Figure A2-11-1 Bigot curve. (a) VC (b) FFC

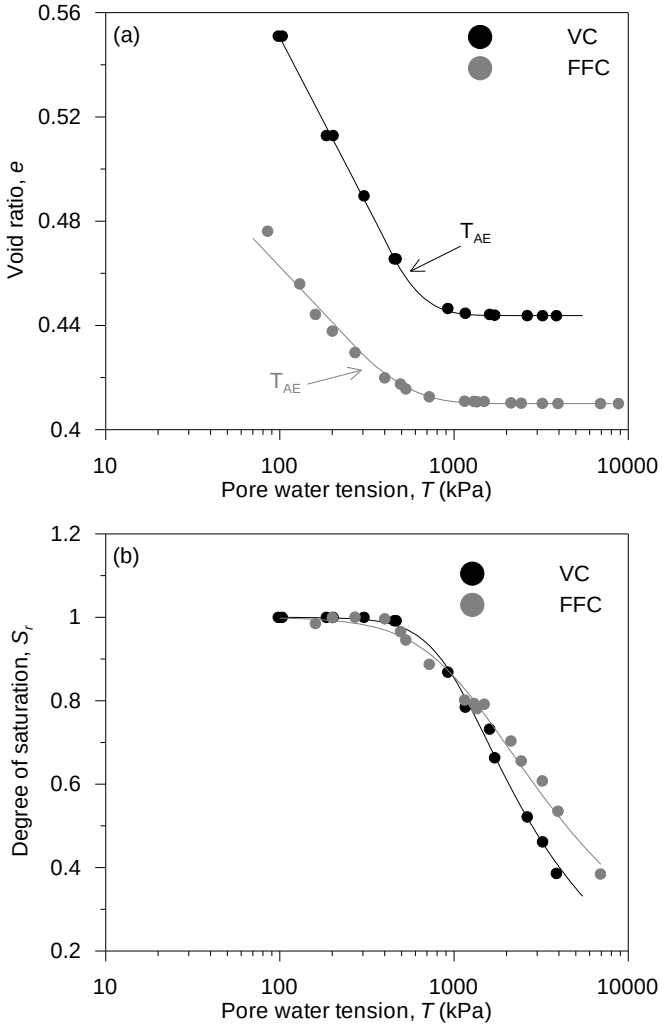

Figure A2-2 Drying curves for VC and FFC materials (a) Void ratio (b) Degree of saturation

Equipment and Procedure

The non-de-aired specimens for the rings test is prepared and cast as described in Appendix A, but only the 5mm mould was used. For the preparation of the de-aired specimens, the slip was subjected to stirring, under vacuum, for a period of one hour. At the end of this period there were no more bubbles of air being released form the slip. After de-airing the slip was cast as normal.

Upon removal of the cylinder specimen from the mould the sample is vacuum packed and

stored for a minimum of 24 hours to allow the water content throughout the sample to reach an equilibrium.

The cast sample is one large hollow cylindrical piece. In order to create rings that were used for each test the cast cylinder was cut. A small ring at both the top and bottom of the large sample were removed. From the remaining sample rings of 2cm height were cut. It was possible to create five rings from each sample. Rings with defects identified from visual inspection were discarded. Defects included small cracks created from cutting the rings or pin holes on the faces of the rings that could act as a place for crack initiation. The rings were slid carefully along the teflon cylinder so as they were positioned 1.5cm apart. The top and bottom face of each ring was covered with a small quantity of petroleum jelly to prevent evaporation from these surfaces, meaning evaporation could only occur from the face of each of the rings. The weight of petroleum jelly used in doing this was recorded. The Teflon cylinder with the prepared rings was then positioned on the balance so as it was in the centre of the three webcams. The balance is used to record the mass loss from the rings during the evaporation process.

The time from when the sample is removed from the vacuum packaging to the test beginning was kept to a minimum as during the final sample preparation there would have been evaporation from the samples. The time taken to prepare the rings and start the test was approximately 6 to 8 minutes.

Once the test was started samples were allowed to evaporate and eventually develop cracks. Once all of the rings had developed cracks the test was stopped. The petroleum jelly was removed from each of the rings and the gravimetric water content of each individual ring measured by placing the rings into the oven for 24hrs.

The relative humidity around the samples was not measured for each test. The tests were performed in a temperature controlled laboratory environment. The relative humidity of which

varies between 40 and 50%.

It was not practical to test each ring individually due to the number of rings being tested. There were therefore four or five rings being tested at the same time, with the change in weight during evaporation being recorded by a single balance. It was therefore necessary to develop a method for calculating the water content of each individual ring throughout the evaporation process. The w% taken at the end of the test by placing the rings in the oven showed that the rings did not have the same final water contents. There are two possible explanations for this:

1. An assumption can be made that because the sample is stored for a period prior to the start of the test with evaporation being prevented that all of the rings will have the same water content at the start of the test. The difference in w% at the end of the test between the rings is therefore explained by small differences in the rate of evaporation between the rings. From the results it was clear that, in the majority of rings, the rings positioned on the top and bottom of the PTFE cylinder had lower water contents than those in the centre. The obvious explanation for this is that water evaporating from the top and bottom rings has more environment to move into than the water from the rings in the centre. Meaning that the relative humidity of the air immediately surrounding the top and bottom rings will be marginally lower than that of the centre rings, resulting in a higher evaporation rate.
2. The rings do not start with the same initial water content. If the storage of the sample before testing was not of sufficient length to ensure an equilibrium of the water content throughout the sample then it is clear that the rings, at the end of testing, would not have the same water content. Due to the addition of the petroleum jelly the evaporation is a 2D problem. Assuming that the relative humidity of the air surrounding the rings is the same then the rate of evaporation from each sample would be the same, resulting in the change in water content during the test of each ring being the same.

In order to determine which explanation was correct a dummy sample was prepared using the same procedure as for the real tests, with the sample being sealed and stored for a period of 24hrs, which was the minimum period any of the test samples were stored for. At the point at which the test would be started the water content of each ring was taken. The results showed that within an acceptable experimental error, all of the rings had the same water content. It is therefore assumed that the rings for each individual test have the same initial water content and that the difference in the final water contents is due to small differences in the relative humidity in the air surrounding each ring.

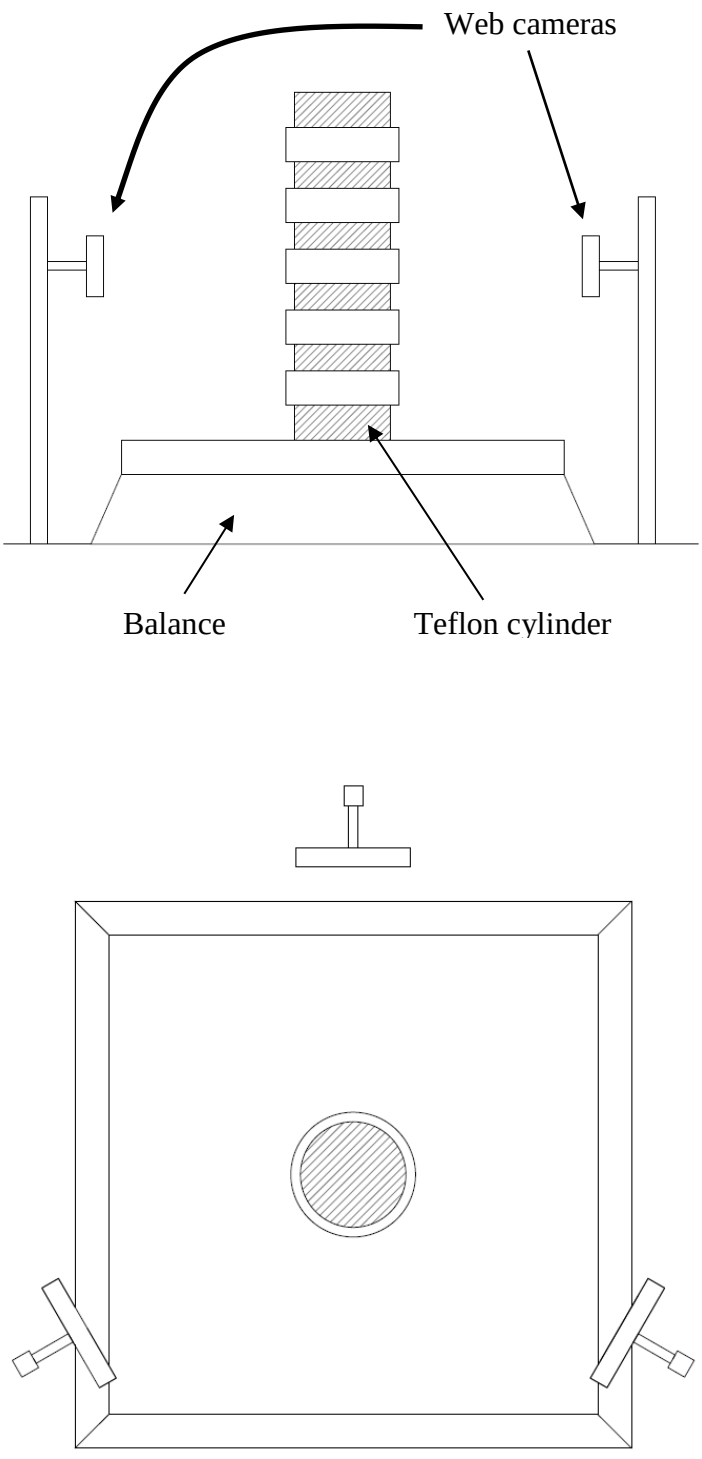

Figure A2-3 Apparatus for cylinder rings test

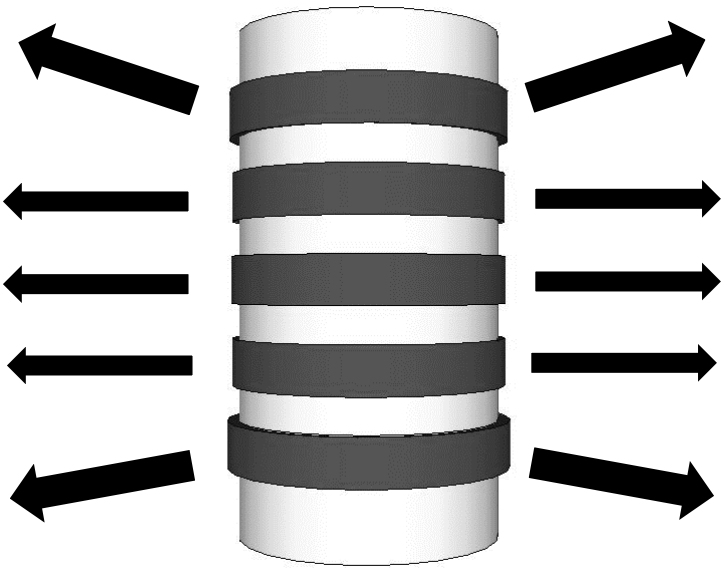

Figure A2-4 Evaporation potential from each ring

Method for calculating w%

The water content, *w* of a specific ring, *r*, at time, *t* ($w_{r,t}$) is calculated from the following:

$$w_{r,t} = \frac{m_{w,r,t}}{m_{s,r}} \quad \text{[A2-1]}$$

Where $m_{w,r,t}$ is the mass of water in the ring at time t and $m_{s,r}$ is the mass of solids in the ring, obtained from drying the ring in the oven at the end of the test. $m_{w,r,t}$ is obtained from the following:

$$m_{w,r,t} = m_{w,r,t_0} - m_{w^e,r,t} \quad \text{[A2-2]}$$

Where m_{w,r,t_0} is the mass of water in the ring at the start of the test and $m_{w^e,r,t}$ is the mass of water evaporated from the ring at time t. m_{w,r,t_0} and $m_{w^e,r,t}$ are calculated as follows:

$$m_{w,r,t_0} = w_{t_0} \cdot m_{s,r} \quad \text{[A2-3a]}$$

$$m_{w^e,r,t} = m_{w^e,t} \cdot \alpha \quad \text{[A2-3b]}$$

Where w_{t_0} is the water content of the rings at the start of the test, $m_{w^e,t}$ is the mass of water evaporated from all the rings and α is the ratio between the water evaporated from ring *r* during the test (m_{w^e,r,t_f}) and the mass of water evaporated from all of the rings, R, during the test (m_{w^e,R,t_f}), which is measured on the balance during the test.

$$\alpha = \frac{m_{w^e,r,t_f}}{m_{w^e,R,t_f}} \quad \text{[A2-4]}$$

m_{w^e,r,t_f} is calculated from the following:

$$m_{w^e,r,t_f} = m_{w,r,t_0} - m_{w,r,t_f} \quad \text{[A2-5]}$$

Where m_{w,r,t_f} is the mass of water in the ring at the end of the test, obtained by putting the ring into the oven after the test.

This method of calculating the water content of a single ring at any point during the drying process is based on the assumption that the rate of evaporation from each ring can change, but the ratio of the rate of evaporation between the rings for each time step cannot change.

In order for this assumption to be valid the test must be stopped while all of the rings are still in the linear section of the drying curve. Figure shows the water content, w, against time for a Vitreous China specimen that was allowed to evaporate until almost completely dry. The figure shows that the linear part of the drying pathway stops at a water content of approximately 5%. The water content, at the point where the test was dismantled, of all of the rings in all of the different VC tests was 10% or greater, i.e. all of the rings were still in the linear part of the drying curve.

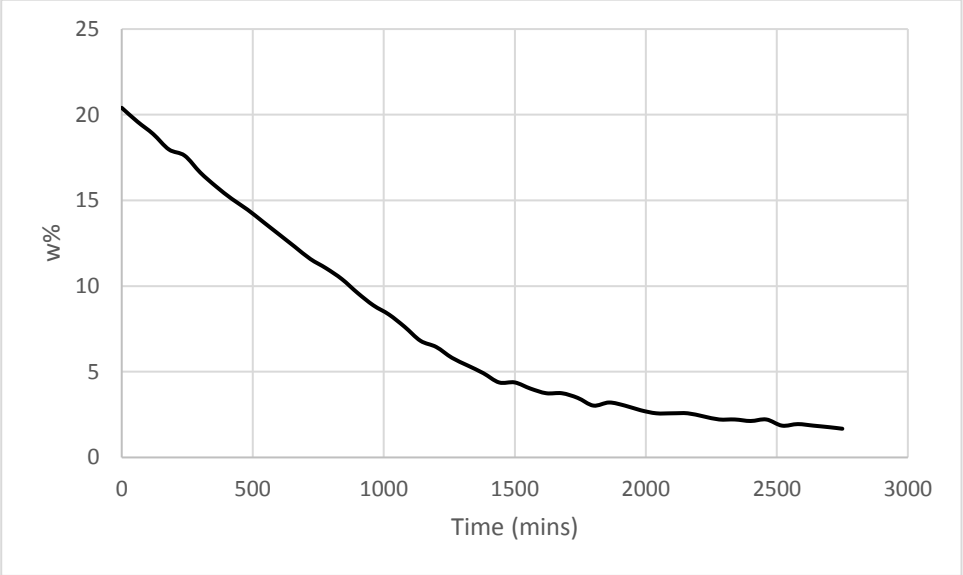

Figure A2-5 Gravimetric water content against time for a free drying Vitreous China sample

VC Non-de-aired

The results of the non-de-aired and de-aired VC tests are shown below in tables A2-1 to A2-8. All of the 38 rings tested resulted in a crack. The moisture content of the rings at the start of testing varied from test to test. Figure shows the relationship between the moisture content at the beginning of the test and at the point of cracking. As there is a general spread of results it can be concluded that there is no clear relationship between the moisture content at the start of testing and at cracking. This result is also present for the de-aired VC material and the non-de-aired and de-aired FFC material.

From Figure it can be seen that there is a shift to the left for the de-aired specimens when compared to the non-de-aired specimens, i.e. the cracks occur at a lower water content for de-aired rings. This suggests that de-airing the slip has delayed the onset of cracking by increasing the strength of the material.

Table A2-1 Non-de-aired VC rings results (23-06)

Ring no.	w_{t0}	Crack time (minutes)	w_{crack}	Δw
1	20.38	44	17.75	2.63
2	20.38	64	16.9	3.48
3	20.38	53	17.3	3.08
4	20.38	61	16.8	3.58

Table A2-2 Non-de-aired VC rings results (24-06)

Ring no.	w_{t0}	Crack time (minutes)	w_{crack}	Δw
1	20.09	56	17.3	2.79
2	20.09	70	16.5	3.59
3	20.09	57	17	3.09
4	20.09	96	15.7	4.39
5	20.09	58	17.1	2.99

Table A2-3 Non-de-aired VC rings results (29-06)

Ring no.	w_{t0}	Crack time (minutes)	w_{crack}	Δw
1	20.10	55	17.7	2.40
2	20.10	84	16.5	3.60
3	20.10	84	16.45	3.65
4	20.10	94	15.9	4.20

VC De-Aired

Table A2-4 De-aired VC rings results (25-06)

Ring no.	w_{t0}	Crack time (minutes)	w_{crack}	Δw
1	19.89	77	16.62	3.27
2	19.89	121	15.2	4.69
3	19.89	105	15.75	4.14
4	19.89	119	15.35	4.54
5	19.89	81	16.42	3.47

Table A2-5 De-aired VC rings results (26-06)

Ring no.	w_{t0}	Crack time (minutes)	w_{crack}	Δw
1	20.45	114	15.3	5.15
2	20.45	119	16.9	3.55
3	20.45	74	17.7	2.75
4	20.45	107	107	3.95
5	20.45	89	89	3.70

Table A2-6 De-aired VC rings results (27-06)

Ring no.	w_{t0}	Crack time (minutes)	w_{crack}	Δw
1	20.58	71	17.2	3.38
2	20.58	75	17.1	3.48
3	20.58	93	16.5	4.08
4	20.58	112	15.5	5.08
5	20.58	93	16.1	4.48

Table A2-7 Non-de-aired VC rings results (30-06)

Ring no.	w_{t0}	Crack time (minutes)	w_{crack}	Δw
1	20.77	106	17.1	3.67
2	20.77	150	16.45	4.32

3	20.77	145	16.37	4.40
4	20.77	146	16.43	4.34
5	20.77	161	15.8	4.97

Table A2-8 De-aired VC rings results (30-09)

Ring no.	w_{t0}	Crack time (minutes)	w_{crack}	Δw
1	19.79	85	15.34	4.45
2	19.79	81	15.27	4.52
3	19.79	56	16.66	3.13
4	19.79	71	15.97	3.82
5	19.79	51	16.59	3.20

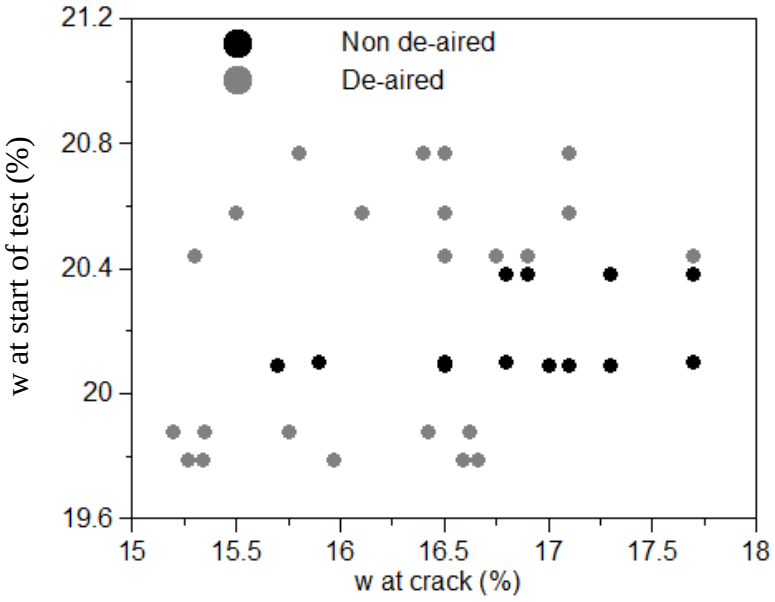

Figure A2-6 Effect of initial water content on the water content at time of cracking

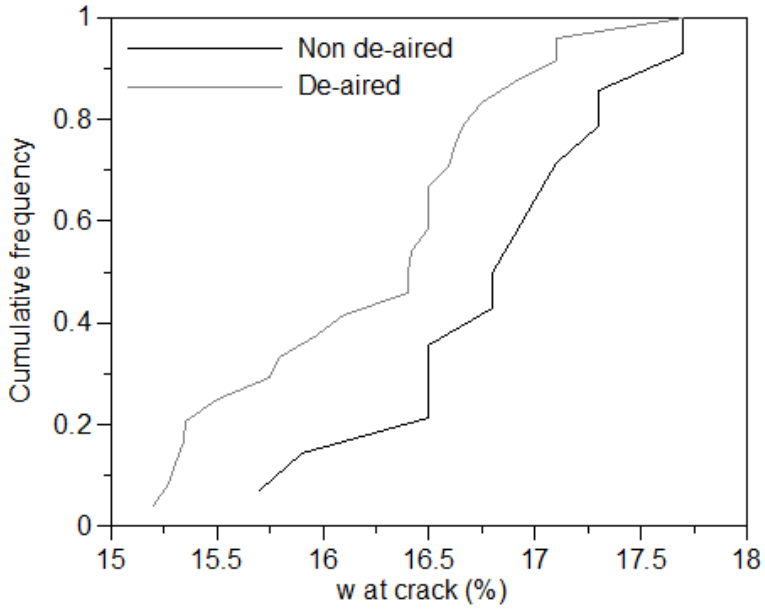

Figure A2-7 Effect of de-airing slip on the plastic limit (VC)

FFC non-de-aired

The results of the non-de-aired and de-aired FFC tests are shown below in Tables A2-9 to A2-18. All of the 44 FFC rings cracked. As with the VC tests, the moisture content of the rings at the start of testing varied from test to test. Figure shows the relationship between the moisture content at the beginning of the test and at the point of cracking. As there is a general spread of results it can be concluded that there is no clear relationship between the moisture content at the start of testing and at cracking.

From Figure it can be seen that there is a shift to the left for the de-aired specimens, i.e. the cracks occur at a lower water content for de-aired rings. This suggests that de-airing the slip has delayed the onset of cracking by increasing the strength of the material.

Table A2-9 Non-de-aired FFC rings results (03-07)

Ring no.	w_{t0}	Crack time (minutes)	w_{crack}	Δw
1	16.67	47	14.75	1.92
2	16.67	74	14	2.67
3	16.67	112	12.75	3.92
4	16.67	83	13.82	2.85
5	16.67	68	14.05	2.62

Table A2-10 Non-de-aired FFC rings results (04-07)

Ring no.	w_{t0}	Crack time (minutes)	w_{crack}	Δw
1	17.16	63	14.73	2.43
2	17.16	81	14.14	3.02
3	17.16	81	14.03	3.13
4	17.16	68	14.55	2.61
5	17.16	84	13.9	3.26

Table A2-11 Non-de-aired FFC rings results (15-08)

Ring no.	w_{t0}	Crack time (minutes)	w_{crack}	Δw
1	16.72	63	13.58	3.14
2	16.72	60	13.56	3.16
3	16.72	52	13.97	2.75
4	16.72	66	13.43	3.29
5	16.72	52	13.87	2.85

FFC de-aired

Table A2-12 De-aired FFC rings results (01-07)

Ring no.	w_{t0}	Crack time (minutes)	w_{crack}	Δw
1	18.72	97	15.25	3.47
2	18.72	115	14.6	4.12
3	18.72	116	14.65	4.07
4	18.72	108	14.75	3.97

Table A2-13 De-aired FFC rings results (02-07)

Ring no.	w_{t0}	Crack time (minutes)	w_{crack}	Δw
1	18.67	128	14.68	3.99
2	18.67	133	14.6	4.07
3	18.67	142	14.17	4.50
4	18.67	130	14.42	4.25

Table A2-14 De-aired FFC rings results (05-07)

Ring no.	w_{t0}	Crack time (minutes)	w_{crack}	Δw
1	16.86	51	14.72	2.14
2	16.86	59	14.44	2.42
3	16.86	61	14.28	2.58
4	16.86	70	13.98	2.88

Table A2-15 De-aired FFC rings results (09-07)

Ring no.	w_{t0}	Crack time (minutes)	w_{crack}	Δw
1	16.99	34	14.85	2.14
2	16.99	64	13.35	3.64
3	16.99	52	13.95	3.04
4	16.99	56	13.45	3.54

5	16.99	50	13.7	3.29

Table A2-16 De-aired FFC rings results (12-07)

Ring no.	w_{t0}	Crack time (minutes)	w_{crack}	Δw
1	16.90	52	14.2	2.7
2	16.90	62	13.6	3.30
3	16.90	64	13.62	3.28

Table A2-17 De-aired FFC rings results (13-07)

Ring no.	w_{t0}	Crack time (minutes)	w_{crack}	Δw
1	16.90	82	13.78	3.12
2	16.90	89	13.52	3.38
3	16.90	87	13.22	3.68
4	16.90	92	13	3.90

Table A2-18 De-aired FFC rings results (14-07)

Ring no.	w_{t0}	Crack time (minutes)	w_{crack}	Δw
1	16.27	46	14.14	2.13
2	16.27	55	13.77	2.50
3	16.27	62	13.34	2.93
4	16.27	66	13.13	3.14
5	16.27	64	13.16	3.11

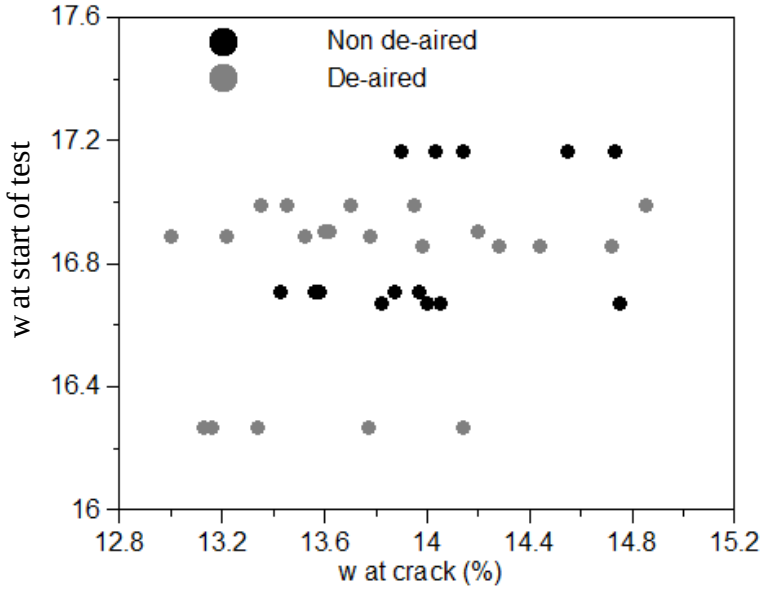

Figure A2-8 Effect of initial water content on the water content at the time of cracking (FFC)

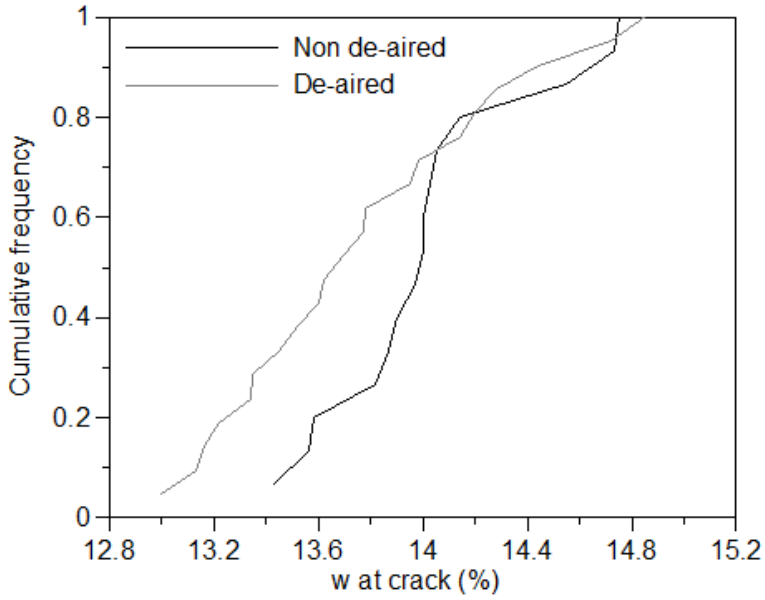

Figure A2-9 Effect of de-airing slip on the plastic limit (FFC)

Discussion

The results of the cylinder rings tests show that de-airing the slip delays the onset of

cracking in terms of cracking water content for both the VC and FFC materials.

All of the rings for both materials cracked, unlike for the full height cylinder where, despite the lower number of specimens tested, both materials had tests where the cylinder did not crack. The increase in cracking for the rings test can be attributed as being either as a result of the small change in the VC and FFC material mixes between the two different test types, or as a result of the reduction in height of the cylinders. A reduction in height having an effect on the likelihood of cracking suggests that the initial assumption that the specimen is free to shrink vertically is not valid. Whether this assumption was correct or not, the assessment that de-airing delays cracking can be considered valid.